CYRIC

ANNUAL REPORT

2005

(January 2005 - December 2005)

CYCLOTRON AND RADIOISOTOPE CENTER
TOHOKU UNIVERSITY
http://www.cyric.tohoku.ac.jp/

PREFACE

In this twenty-sixth issue of the CYRIC Annual Report, we summarize the activities in research and development, and in training of radioisotope safe-treatment at the Cyclotron and Radioisotope Center (CYRIC) during the calendar year 2005.

Research at CYRIC was carried out in the fields of nuclear physics, nuclear chemistry, material sciences, nuclear medicine using PET (oncology, brain study, pharmacology), radiopharmaceutical chemistry, health physics, nuclear instrumentation, nuclear medical engineering (diagnosis and therapy technology), nuclear engineering and elemental analysis using PIXE.

Developments and improvements on nuclear instruments and techniques have progressed; one of the 2005 highlights is the construction of high efficiency Germanium gamma-ray detectors array (Hyper-ball 2) which consists of 6 clover type Ge detectors and 13 single crystal type Ge detectors; other highlights are the construction of high-intensity neutron-beam course and the success of extraction of the negatively charged hydrogen beam, which are combined to extend the research with neutron beams. The beam attenuator device and the acceleration of C-O-Ne cocktail beam were also introduced for testing semiconductor devices. Since the 14 GHz ECR ion source has been improved for the plasma region, the acceleration of heavy ion beams was extended to the mass region of Krypton. The high-intensity neutron-beam course installed in 2004 has been used effectively for studies of neutron-induced reactions like fragment production and activation, and also for semiconductor irradiation experiments. A total of 2513 hours of beam-time of the K=110MeV cyclotron were delivered for scheduled operation in research work.

[^{18}F]FDG, [^{18}F]FRP-170, [^{11}C]methionine, [^{11}C]doxepin, [^{11}C]raclopride, [^{11}C]donepezil and [^{15}O]water were routinely prepared and supplied to clinical PET studies. In May 2005, [^{11}C]BF-227, a new β-amyloid imaging agent, was successfully prepared and supplied to the first clinical PET study in collaboration with TUBERO, Tohoku University.

Molecular imaging of dementia such as Alzheimer's disease and mild cognitive impairment (MCI) has been activated at CYRIC since the starting of clinical application of [^{11}C]BF-227, the first domestically-supplied β-amyloid imaging probe. [^{11}C]Donepezil is also important for evaluation of neurotransmission of the cholinergic nervous system and the clinical study has been conducted. [^{18}F]FDG study is still very active, and CYRIC has

participated in a nationwide multi-center study, Study on Diagnosis of Early Alzheimer's Disease (SEAD)-Japan. Histamine H1 receptor imaging and dopamine D2 receptor imaging have seen steadily progressing this year. Clinical evaluation of several new antihistamines is a good example of clinically-oriented application of receptor studies. In addition to PET study of sports science, scientific evaluation of various techniques used in alternative medicine, such as aroma-therapy and acupuncture, is becoming another important research field.

As for clinical diagnosis, [^{11}C]methionine has been very useful for diagnosis of brain tumors. This tracer has given an important medical information regarding decision making of neurosurgeons at Tohoku University Hospital, as well as clinical research on whole-body oncology studies of malignant and non-malignant diseases that are not reimbursed by health insurance yet.

The research program on PIXE analysis has been carried out by using an electrostatic accelerator (4.5 MV Dynamitron) at the Fast Neutron Laboratory (FNL), Graduate School of Engineering, Tohoku University, under the scientific tie up between CYRIC and FNL. A total of 528 hours of beam-time was served to this program. The micro-beam formation system of which the beam spot size is about 1μm was completed. Micro-PIXE analysis, STIM analysis, and beam processing are now available.

The training for radioisotope safe-treatment was carried out as usual. In 2005, a total of 1097 staffs and students of Tohoku University took three courses: 1) Radioisotopes and radiation generators (525 trainees), 2) X-ray machines and electron microscope (478), and 3) Synchrotron Radiation (94). The number of trainees (1122) decreased slightly from 2005 (2.3%), while that for x-rays and SOR increased markedly. The English classes for each course were practiced for 88 foreign students and scientists.

This year, two big projects started: 1) Development of ultra high resolution semiconductor PET under the support of a Grant-In-Aid for Specially Promoted Research of the Ministry of Education, Sports, Culture, Science and Technology, 2) CYRIC and National Institute of Radiological Sciences (NIRS) joint educational program of molecular imaging using PET.

We are most grateful to Tohoku University and to the Ministry of Education, Sports, Culture, Science and Technology for continuous support.

January 2006

Keizo ISHII
Director
Cyclotron and Radioisotope Center, Tohoku University

EDITORS:

Keizo ISHII
Masatoshi ITOH
Mamoru BABA
Ren IWATA
Tsutomu SHINOZUKA

WORD PROCESSED BY

Yu-ko YAMASHITA

CONTENTS

I. NUCLEAR PHYSICS

II. NUCLEAR INSTRUMENTATION

III. NUCLEAR ENGINEERING

IV. NUCLEAR MEDICAL ENGINEERING

V. PIXE AND ENVIRONMENTAL ANALYSIS

2005

VI. RADIOCHEMISRTY AND NUCLEAR CHEMISTRY

VII. RADIOPHARMACEUTICAL CHEMISTRY AND BIOLOGY

VIII. NUCLEAR MEDICINE

2006

I. NUCLEAR PHYSICS

I. 1. Search for Chiral Doublet Structures in ^{79}Kr with Hyperball2

Suzuki T.[1,2], Koike T.[2], Ahn T.[3], Endo T.[1], Fujita M.[1], Fu Y.Y.[4], Fukuchi T.[5], Joshi P.[6], Kinoshita S.[2], Ma Y.[2], Miura Y.[2], Miyashita Y.[1,2], Ohguma M.[1,2], Rainovski G.[3,7], Sato N.[1,2], Shinozuka T.[1], Shirotori K.[2], Tamura H.[2], Tateoka M.[1,2], Timar J.[8], Ukai M.[1], Wakui T.[1], and Yamazaki A.[1]

[1]*Cyclotron and Radioisotope Center, Tohoku University*
[2]*Department of Physics, Tohoku University*
[3]*Department of Physics and Astronomy, SUNY, Stony Brook*
[4]*Department of Nuclear Physics, China Institute Atomic Energy*
[5]*Department of Physics, Osaka University*
[6]*Department of Physics, University of New York*
[7]*St. Kliment Ohridski Univeristy of Sofia*
[8]*Institute of Nuclear Research (ATOMKI)*

Nearly degenerate pairs of ΔI = 1 rotational bands, which are interpreted as chiral twin bands candidate[1,2], are observed in several odd-odd and few odd-A nuclei in the A~130 [3-7] and the A~105 [8-13] regions. In these triaxial nuclei, left- and right-handed chiral geometries in the body-fixed frame can be formed from the mutually perpendicular angular momentum of the valence proton, valence neutron and the core rotation. In odd-A nuclei, one of the components of angular momentum is a broken pair of quasi-particles at higher spin states. Chirality can be identified via (1) nearly degenerate pair of ΔI=1 rotational bands with the same parity and (2) $B(E2; I \rightarrow I-2)_{in,out}$ and $B(M1; I \rightarrow I-2)_{in,out}$ having same or similar values between the pair bands.

Recently, life time for chiral candidate members in ^{134}Pr in the A~130 region was measured; however $B(E2)$ values are largely different between the two bands[14]. This result suggests a difference in deformation between the two, challenging the origin of these doublets from formation of chirality [15]. While verification of nuclear chirality is being carried out in the mentioned mass region, observations of chiral candidates are expected in a new mass region, namely the mass A~80 region.

In this region, the best single particle configuration for chiral geometry is $\pi g_{9/2} \otimes \nu g_{9/2}^{-1}$ for odd-odd nucleus. Angular momentum of valence proton is aligned along the short axis, and that of valence neutron is aligned along the long axis where three

axes are defined by triaxial mass distribution. This mechanism is opposite to that of $\pi g_{9/2}^{-1} \otimes \nu h_{11/2}$ in the A~105 region, and similar to $\pi h_{11/2} \otimes \nu h_{11/2}^{-1}$ in the A~130 region. In this study, we tried to search for chiral twin bands in ^{79}Kr in the mass 80 regions.

High spin states in ^{79}Kr were populated via the $^{70}\mathrm{Zn}(^{13}\mathrm{C},4n)$ reaction at the beam energy of 65 MeV, obtained from the 930 cyclotron at Cyclotron and Radioisotope Center, Tohoku university, impinging upon a stack of two 500 μg/cm^2 thickness self-supporting ^{70}Zn (70% enriched) targets. The emitted gamma rays were detected by the Hyperball-2 array. This array houses 14 normal type detectors and 6 clover type detectors, each of which is shielded with BGO counters for Compton background suppression. A total of approximately 370 million triple gamma coincidence events was sorted into cubes and analyzed with the RADWARE programs[16]. Example of triple gamma coincidence spectrum is shown in Fig. 1.

The partial level scheme for ^{79}Kr obtained from the present experiment is shown in Fig. 2. Bottom and upper part of band labeled as (a) in Fig. 2 was previously reported by Johns *et. al.*[17] with the $\nu g_{9/2}^{-1}$ and $\pi g_{9/2}^{2} \otimes \nu g_{9/2}^{-1}$ configuration assigned, respectively. Band (b) in Fig. 2 is identified in the present experiment for the first time. Level (c) was observed previously. The level is assigned with 21/2+ and could be independent from band (b) because of no gamma ray transition observed between the 23/2+ states in band (b) and the 21/2+ states.

Linear polarization for links connecting (a) and (b) can be extracted with clover detectors to infer relative spin and parity for the side band (b). The experimental linear polarization is defined as $P = (1/Q)(N_\perp - N_\parallel)/(N_\perp + N_\parallel)$, where $N_\perp$ ($N_\parallel$) is the number of added-back photo peak counts which are events scattered in to perpendicular (parallel) direction with respect to the reaction plane and Q is polarization sensitivity of the clover detectors. Polarization sensitivity Q has yet to be measured; however the sign of P can determined without knowing Q. Positive linear polarization values indicate electric character of transitions, while negative values indicate their magnetic character. In the analysis, two γ-γ matrices were sorted with one axis corresponding to a single-hit event including that of single crystal detector and the other axis corresponding to added-back double-hit events. One matrix is sorted from only parallel-scattered events, while the other matrix from perpendicular-scattered events. The results from these measurements for γ-ray transition in the positive parity band are shown in Fig. 3. The transitions

assigned as $E2$ in Ref.[17] (Red and Sky-blue) are found to have positive polarization values, and the transitions assigned as $M1$ in Ref.[17] (Orange) have near zero or negative values.

The 472-keV transition shows electric character; if the parity were negative ($E1$), the 636-keV and 1616-keV transition would be of $M2$ and $M3$, respectively. For the same level, if the spin were 25/2, the 1616-keV transition would be of $E3$. Therefore, level (c) is assigned as 21/2+. The 811-keV transition shows electric character; if the spin were 27/2, 1676-keV transition would be of $E3$, and thus the band head for band (b) is assigned as 23/2+.

In Fig. 4(a), the excitation energy of the yrast and the partner band is plotted as a function of spin. Energy difference of about 1 MeV, which are not degenerate, is observed. In Fig. 4(b), the excitation energy is plotted relative to a rigid rotor, which reveals single particle alignment. If the two bands were chiral partners, it would show a similar trend. In Fig. 4(c), $S(I) = [E(I) - E(I-1)]/2I$ is plotted as a function of spin. Smooth variation of $S(I)$ with I suggests perpendicular coupling of a single particle angular momentum to the core rotation, as a strongly coupled band built on a single particle angular momentum aligned perpendicular to the rotational axis for an axial symmetric rotor has no signature splitting. The present result indicates that one of the single particle angular momenta has sizable component along the core rotation. Overall, the two bands do not show chiral characters from this work.

In summary, the side band structure to the $\pi g_{9/2}^{\ 2} \otimes \nu g_{9/2}^{\ -1}$ yrast has been identified in ^{79}Kr. Tentative spin and parity assignments are made based on the linear polarization measurement. The current result shows that the side band structures are of non chiral nature.

References

1) Frauendorf S., Meng J., Nucl. Phys. A **617** (1997) 131.
2) Starosta K., et. al., Nucl. Phys. A **682** (2001) 375c.
3) Koike T., Starosta K., Chiara C.J., Fossan D.B., LaFosse D.R., Phys. Rev. C **67** (2003) 044319.
4) Petrache C.M., et. al., Nucl. Phys. A**597** (1996) 106.
5) Hecht A.A., et. al. Phys. Rev. C **63** (2001) 051302(R).
6) Hartley D.J., et. al., Phys. Rev. C **64** (2001) 031304(R).
7) Rainovski G., et. al., Phys. Rev. C **68** (2003) 024318.
8) Vamman C., Fossan D.B., Koike T., Storasta K., Phys. Rev. Lett. **92** (2004) 032501.
9) Joshi P., et. al., Phys. Lett. B **595** (2004) 135.
10) Timar J., et. al., Phys. Lett. B **598** (2004) 178.
11) Joshi P., et. al., Eur. Phys. J. A **24** (2005) 23.
12) Zhu S.J., et. al., Eur. Phys J. A **25** (2005) 459.
13) Timar J., et. al., Phys. Rev. C **73** (2006) 011301(R).

14) Tonev D., et. al., Phys. Rev. Lett. **96** (2006) 052501.
15) Petrache C.M., Hagemann G.B., Hamamoto I., Starosta K., Phys Rev. Lett. **96** (2006) 112502.
16) Radford D.C., Nucl. Instrum. Methods A **361** (1995) 297.
17) Johns G.D., et. al., Phys. Rev. C **50** (1994) 2786.

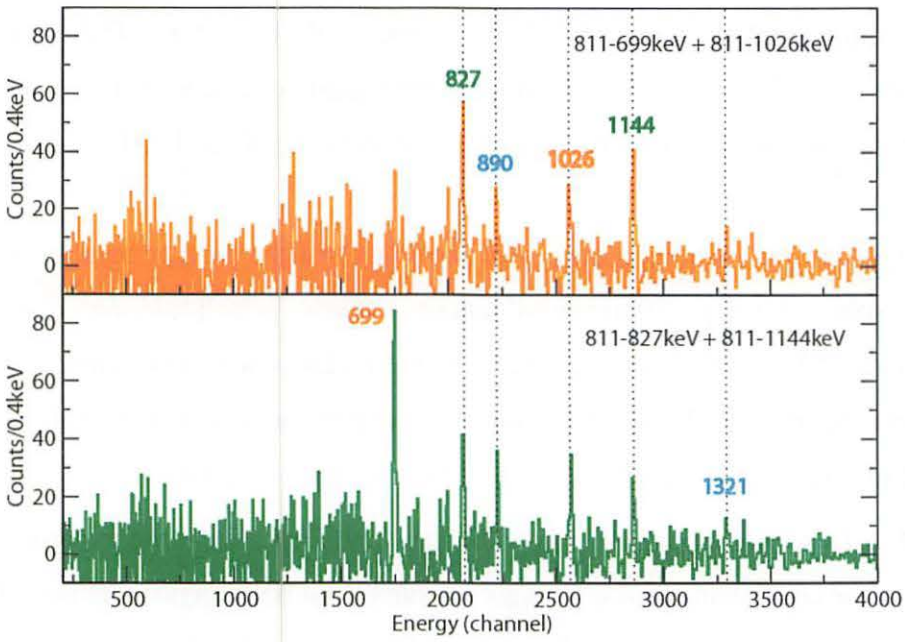

Figure 1. Example of double gated gamma-ray coincidence spectra. Peaks labeled with their energy in keV are assigned to ^{79}Kr.

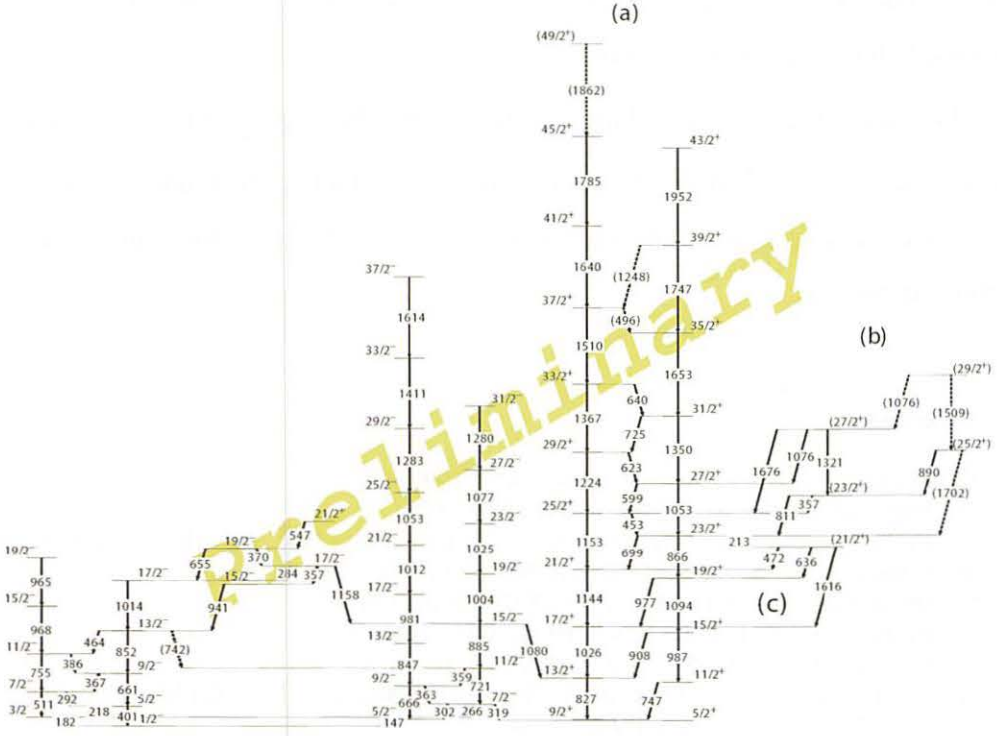

Figure 2. Partial level scheme of ^{79}Kr deduced from the resent study. The energy of the gamma transition is in keV.

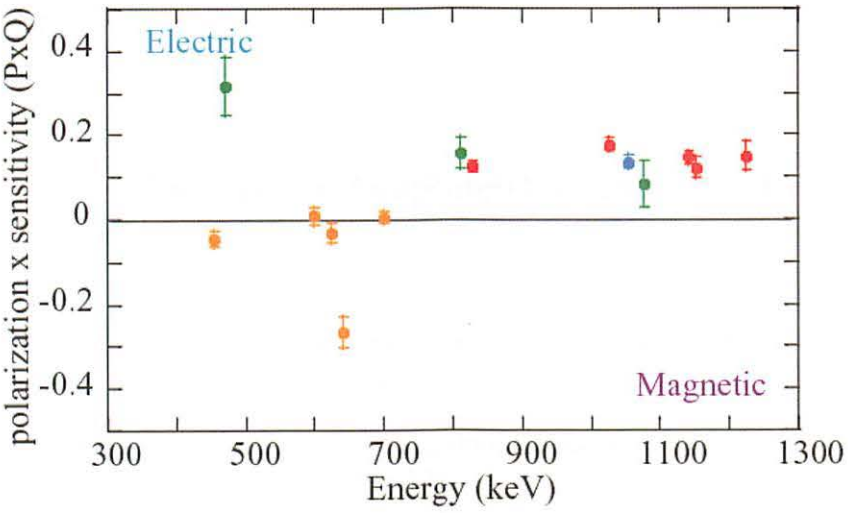

Figure 3. Linear polarization times the clover polarimeter sensitivity. Red and sky-blue points are consistent with electric character of these transitions. Orange colored points are consistent with $M1$ assignment for these transitions made in Ref. [17]. Green points are for transitions identified from the current study. The error bars show only statistical error.

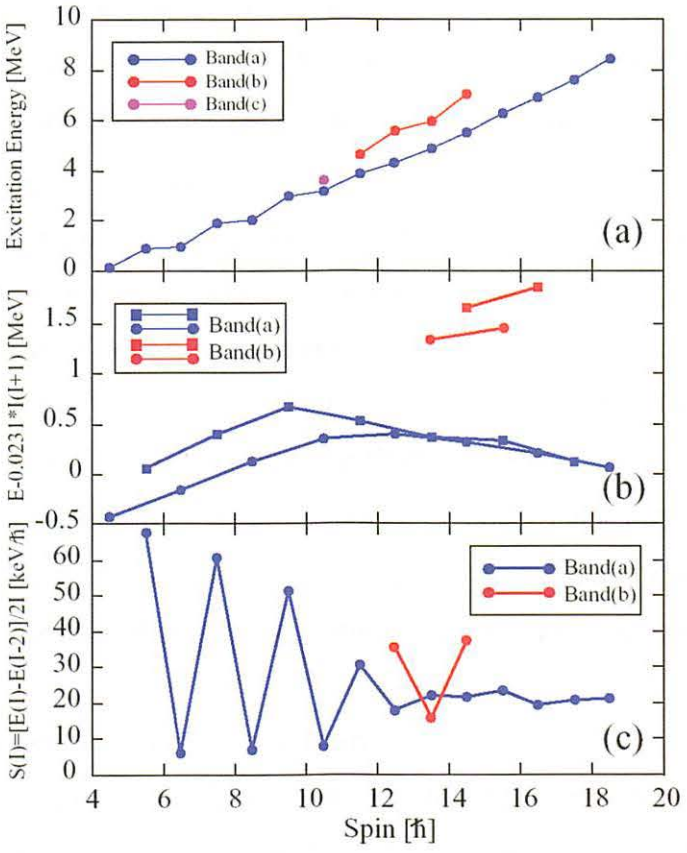

Figure 4 (a): excitation energy, (b): excitation energy minus the rigid-rotor reference, and (c): $S(I)$-$[E(I)$-$E(I$-1)]/2I .

I. 2. Study of High-Spin Structure in ^{151}Er

Fukuchi T.[1], Gono Y.[2], Odahara A.[1], Shinozuka T.[3], Suzuki T.[3], Ukai M.[3], Koike T.[4], Shirotori K.[4], and Ma Y.[4]

[1]*Department of Physics, Osaka University*
[2]*RIKEN*
[3]*Cyclotron and Radioisotope Center, Tohoku University*
[4]*Department of Physics, Tohoku University*

High-spin isomers were reported in $N = 83$ isotones systematically[1], namely ^{143}Nd, ^{144}Pm, ^{145}Sm, ^{146}Eu, ^{147}Gd, ^{148}Tb, ^{149}Dy, ^{150}Ho and ^{151}Er. Their lifetimes range from 10 ns to a few μ sec. The excitation energies of those isomers are close each other ranging between 8.5 and 9.0MeV except for ^{151}Er. Configuration of the high-spin isomers are deduced experimentally and theoretically[2] to be $[\nu(f_{7/2}h_{9/2}i_{13/2})\ \pi(h_{11/2}^2)]_{49/2+}$ for odd nuclei and $[\nu(f_{7/2}h_{9/2}i_{13/2})\ \pi(d_{5/2}^{-1}h_{11/2}^2)]_{27+}$ for odd-odd nuclei. In a high-spin region of these nuclei, the angular momenta of individual valence particles align to the symmetry axis so that the overlaps of nucleon wave functions become to be maximum. Then the shape changes from near spherical to oblate. According to the Deformed Independent Particle Model (DIPM) calculations[2], the shapes suddenly change at high-spin isomeric states. This sudden shape change causes the high-spin isomer. Therefore, these isomers could be described as high-spin shape isomers. As to ^{151}Er nucleus, $J^\pi = 67^-$ isomer at 10.6MeV was reported by C. Foin *et al.*[3,4]. It is important to investigate the high-spin isomer in ^{151}Er, since the spin-parity and the excitation energy of the high-spin isomer in this nuclei are largely different to those of other isotones.

An experiment for ^{151}Er was performed at Cyclotron and Radioisotope Center (CYRIC), Tohoku University. Excitation states in ^{151}Er were populated using the reaction ^{116}Sn(^{40}Ar,5n)^{151}Er. The ^{116}Sn target of 1.4 mg/cm^2 was enriched to 90% and a target foil was backed by 11mg/cm^2 lead to stop the reaction products. This target was bombarded by ^{40}Ar beam of 197MeV with intensity of around 2pnA provided by the cyclotron. A germanium ball, Hyperball-2, which consist of 12 single and 4 clover type detectors was

used for prompt and delayed γ-γ-γ coincidence measurements. The total detection efficiency was about 3.2% for 1.3-MeV γ-ray in the singles mode. A total of 4.5×10^8 above 3-fold coincidence events were recorded in event by event mode.

An example of the γ-ray spectrum obtained by gating on the 1100-keV transition which belongs to ^{151}Er is shown in Fig.1. The coincidence relations between transitions are determined by this kind of spectrum. In order to determine the spin-parity of the high-spin isomer in ^{151}Er, analyses of γ-ray angular correlations and γ-ray linear polarization are also performing. The detailed analyses are now in progress.

References

1) Gono Y., et al., Eur. Phys. J. **A 13** (2002) 5 and references therein.
2) Dossing T., et al., Phys. Scr. **24** (1981) 258.
3) Foin C., et al., Eur. Phys. J. **A 8** (2000) 451.
4) Andre A., et al., Z. Phys. **A 337** (1990) 349.

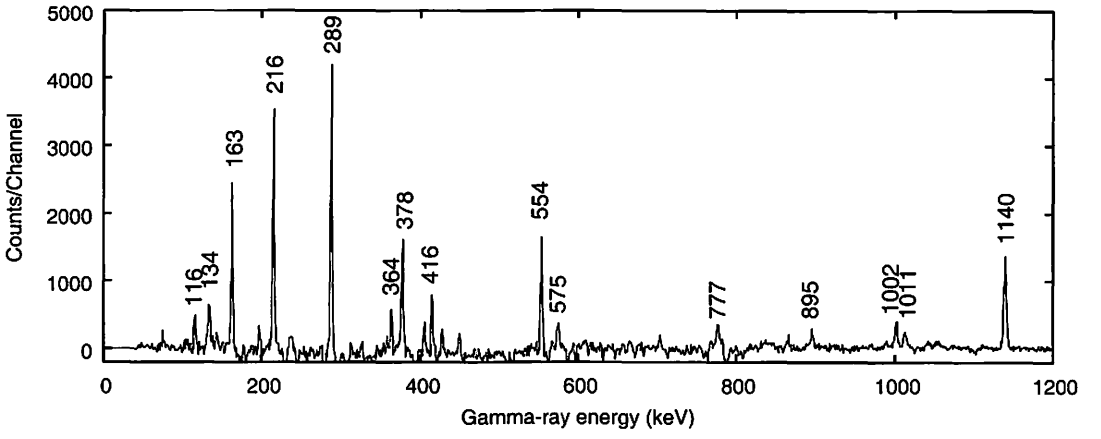

Figure 1. Gamma-ray spectrum obtained by gating on the 1100-keV γ-ray in ^{151}Er. Transitions in ^{151}Er are labeled in energy.

I. 3. "Basic Research in Physics" at CYRIC

Kanda H.[1], Hirose K.[1], Maeda K.[1], Matsuzawa M.[1], Miyase H.[1], Ohtsuki T.[2], Shinozuka T.[3], and Yuki H.[2]

[1]Graduate School of Science, Tohoku University
[2]Laboratory of Nuclear Science, Tohoku University
[3]Cyclotron and Radioisotope Center, Tohoku University

From fiscal year 2004, we have carried out the radioactive isotope (RI) production experiment at CYRIC for one of the themes in the "Basic Research in Physics *(Butsurigaku kiso kenkyuu)*". The main objective of the theme is to learn radiation detection techniques. As the practice of the radiation detection and measurement, the sealed checking sources are usually used. But the hand-made RI sources more stimulate the students' interests. RI production is the demonstration of a modern alchemy that means the conversion of atom which cannot be achieved by conventional chemical methods. An iron plate becomes radioactive after the irradiation of proton beams of 20 MeV. Students identify the radioactive nuclide by the energy spectrum of emitted gamma-rays and reconfirm it by its half life measured by the attenuation of gamma-ray intensity with the course of time[1]. After 3 terms of the experiment, we found some problems as the following list.

1. Produced RI: ^{56}Co is identified by the energy spectrum and the half life, and then we have concluded that ^{56}Fe (p, n) ^{56}Co reaction changes the iron nucleus. However it is still qualitative and with less physical meaning.
2. Because the systematic errors in measurements of counting rates are large compared to the half life of ^{56}Co (77.3 days), the measured half life of ^{56}Co is deviated by the slight changes of the experimental conditions.

This year, we used thin iron plates stacked along the proton beam for the measurement of the RI production cross sections which vary with the energy of incident proton. By introducing the idea of the reaction cross section, students can qualitatively access the scale of the nucleus. And the energy loss: the principle of the radiation detection is qualitatively treated by calculating mean energy of proton in each thin iron plate. Vanadium plates were also prepared to produce ^{51}Cr via (p, n) reaction. Its half

life is 27.7 days[2], that means more than 50% decrease of the gamma-ray intensity can be measured in 4 weeks.

The measured cross sections of ^{56}Fe(p, n)^{56}Co reaction with respect to the incident proton energies are compared with the reference values in Fig. 1. The students' results and the reference values show a good agreement. By assuming the maximum cross section of ^{56}Fe(p, n)^{56}Co reaction is the cross section of spherical ^{56}Fe nucleus, its radius was measured as 3.8 fm. The radius of ^{56}Fe estimated by using $1.25A^{1/3}$ rule is 4.8 fm. Thus they are in the same order. From this result, it is shown that the assumption was not so wrong. The measured count rates of 0.32 MeV-gamma ray from ^{51}Cr and the exponential curve fitted to the data are shown in Fig. 2. A half life of ^{51}Cr obtained from 7 measurements in 5 weeks was 26.4 0.1± (stat.) days. Supposing the difference of 1.3 day from the reference value is one standard deviation, a systematic error of each measurement was estimated to be 5%. It is too large to measure the life time of ^{56}Co within a reasonable accuracy, however it is sufficient to measure the life times of RI's with life times similar to or shorter than ^{51}Cr.

This year, we carried out the RI production experiment at CYRIC for one of the themes in the "Basic Research in Physics *(Butsurigaku kiso kenkyuu)*". We continue to modify and improve it aiming that the students can touch the essence of the physics of nuclei and nuclear reactions and better understand the method of experiments.

References

1) Kanda H., *et al.*, CYRIC Annual Report 2004 (2004) 9.
2) WWW Table of Radioactive Isotopes. URL: http://ie.lbl.gov/toi/.
3) Experimental Nuclear Reaction Data. URL: http://www.nndc.bnl.gov/exfor/exfor00.htm.

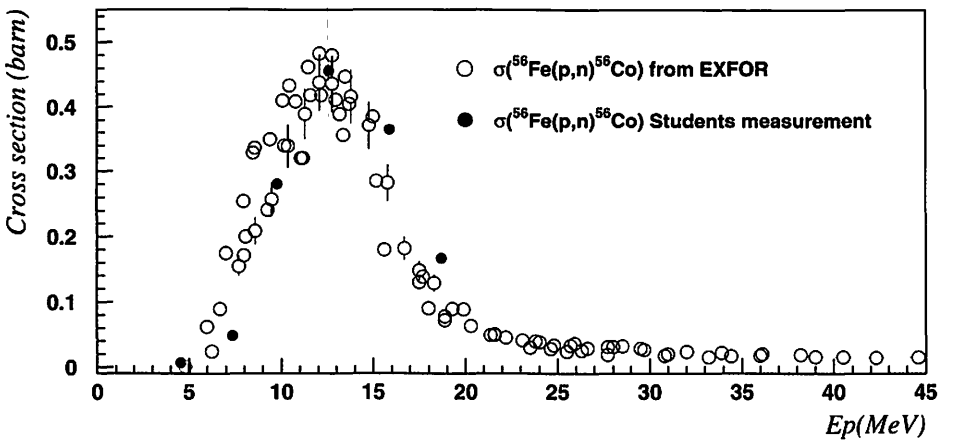

Figure 1. The cross sections of ^{56}Fe(p, n)^{56}Co reaction with respect to the incident energy of proton. Open circles are the reference data from Experimental Nuclear Reaction Data Library[3] and red closed circles are the data from students' measurement.

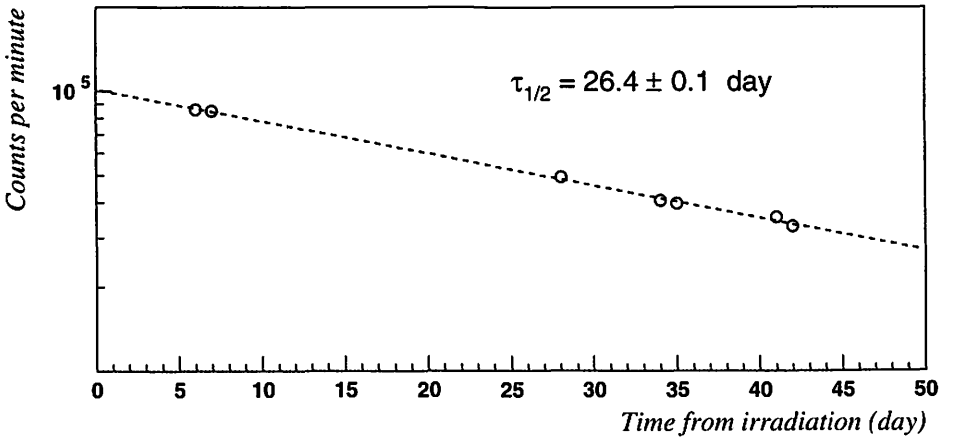

Figure 2. Count rates of 0.32 MeV gamma-ray from ^{51}Cr with respect to the time after proton irradiation. An exponential curve is fitted to the data points and the half life of 26.4 days was obtained.

II. NUCLEAR INSTRUMENTATION

II. 1. Design and construction of RFIGISOL2 at CYRIC

Miyashita Y.[1], Fujita M.[2], Ohguma M.[1], Suzuki T.[1], Sato N.[1], Tateoka M.[1], Ukai M.[2], Wada M.[3], Wakui T.[2], Yamazaki A.[2], and Shinozuka T.[2]

[1]Department of Physics, Tohoku University
[2]Cyclotron and Radioisotope center, Tohoku University
[3]Atomic Physics Laboratory, RIKEN

The study of neutron rich unstable nuclei far from the valley of beta-stability is an important step toward the understanding of nuclear structure. The Radio Frequency Ion Guide Isotope Separator On-Line (RFIGISOL) system provides us neutron rich unstable nuclei produced by proton induced fission reactions with Uranium target. The RFIGISOL1 using large volume thermalization gascell equipped with DC and RF electric field was installed and developed in 2001[1)]. The mass separated fission yield was increased in comparison with the yield from a classical type IGISOL system[2)]. However, the mass separated fission yields from RFIGISOL1 was insufficient for the purpose of nuclear physics experiment such as perturbed angular correlation measurement at the region of more neutron rich unstable nuclei[3)].

The RFIGISOL2 has been developed to increase mass separated fission yields[4)]. Figure 1 shows schematic view of RFIGISOL2. The newly installed functions of RFIGISOL2 are as follows;

- modified electrode configuration at thermalization gascell
- cooling system of thermalization gascell
- driving mechanism of skimmer electrode

In themalization gascell, DC electric field of RFIGISOL1 was produced by 80 ring electrodes which are arranged to form a parabolic structure. Although the DC voltages were applied well, the sophisticated structure and heavy weight of the ring electrodes need to optimize of DC field. In RFIGISOL2, all electrodes have been printed on the 50 μm Kapton film. It is formed into a cylindrical shape. This realizes a flexible design of electrode structure and lighter weight.

A cooling system of thermalization gascell has been installed to reduce the impurity molecules in buffer gas. It has been operated at temperatures between -20°C and 80°C using Fluorinert™ liquid indirect cooling brine. In thermalization gascell, the fission product ions collide with impurity molecules. This process leads to neutralization of fission product ions. This works as an effective method for avoiding ion loses by neutralization[5].

The driving mechanism of the skimmer electrode has been installed. This system enabled to optimize the distance between ion guide orifice and skimmer electrode in on-line experiments. A better optimized electrical field condition for ion optics and the adequate buffer gas pressure at the orifice skimmer region have been obtained. This optimization also enables us to improve velocity dispersion, ion transport, etc.

These new characteristics of RFIGISOL2 lead higher yields of mass separated fission fragments.

References

1) Sonoda T., et al., CYRIC Annual Report (2002).
2) Sonoda T., Doctoral Dissertation, Tohoku University (2004).
3) Miyasita Y., Master Thesis, Tohoku University (2005).
4) Sato N., Master Thesis, Tohoku University (2006).
5) Sato N., in this report.

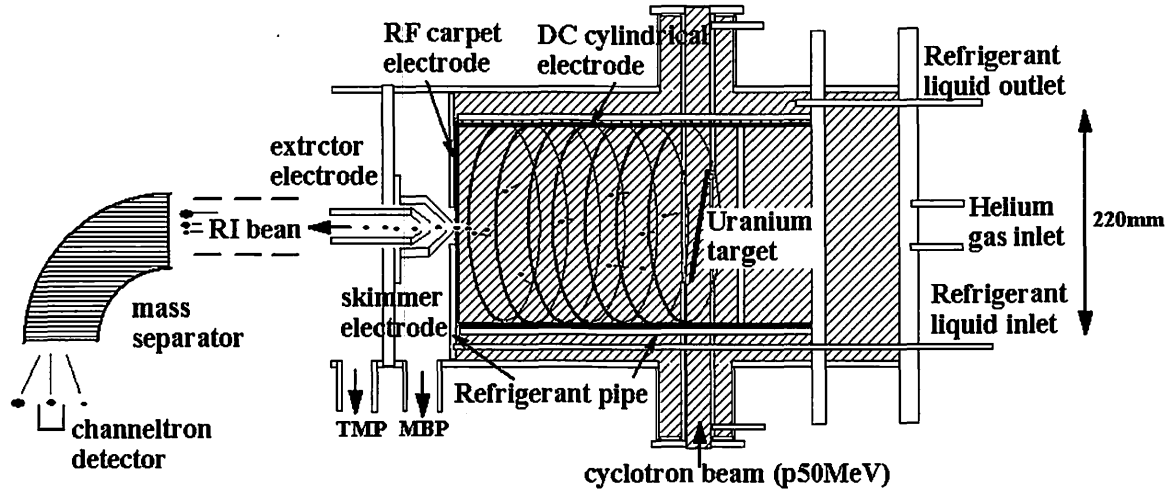

Figure 1. Schematic view of RFIGISOL2.

II. 2. Effects of RF Voltage and Cooling of RFIGISOL2

Sato N.[1], Miyashita Y.[1], Fujita M.[2], Ohguma M.[1], Suzuki T.[1], Tateoka M.[1], Ukai M.[2], Wada M.[3], Wakui T.[2], Yamazaki A.[2], and Shinozuka T.[2]

[1]*Department of Physics, Tohoku University*
[2]*Cyclotron and Radioisotope Center, Tohoku University*
[3]*Atomic Physics Laboratory, RIKEN*

Radio Frequency Ion Guide Isotope Separator On-Line (RFIGISOL) has been designed and developed to study the nuclear structure of neutron-rich nuclei at the medium-mass region far from the beta stability line. The upgraded RFIGISOL2 has been recently designed and developed to obtain higher yield of mass-separated unstable nuclei at CYRIC[1,2].

We report the effects of RF voltage and the performance of cooling of upgraded RFIGISOL2. The details of design and specifications of RFIGISOL2 are presented in this volume[2].

In order to study the effect of RF-voltage in RFIGSIOL2, we chose stable xenon, which are mixed in helium buffer gas and are ionized by the 50 MeV proton beam of the 930 cyclotron. Stable xenon ions are an adequate probe instead of fission products. Xenon ions are transported by the DC and RF electric fields in the RFIGISOL chamber. Then, they are extracted from an exit hole, mass separated by the magnetic field and detected with a channeltron.

Figure1 shows the relation of the yield of xenon ions and RF voltage of carpet electrodes, which are consist of 230 circular electrodes. The frequency of RF field was 3.65 MHz. The carpet electrodes to supply the DC voltage are separated into two groups, the inner and the outer. The voltage of the inner one from the center (the exit hole) to 30 mm was 13 V and the voltage of the outer one from the 30 mm to 110 mm was 10 V. The mass-separated xenon ions have drastically increased from 50 Volt region of RF voltage in

peak to peak (Vpp). The extraction yield of xenon ions at Vpp = 90 V is about 1000 times higher than the yield without RF voltage.

Figure 2 shows the mass spectra of light ions with coolant temperatures at 20°C (top) and -13°C (bottom), respectively. These spectra reflect the impurity concentration in the buffer gas. The electric field was not applied in this experiment. We can see the two prominent tendencies by the effects of cooling down. The first one is the disappeared peaks of A > 20 , and the second is that the yield of A = 16 ion ($^{16}O^{+}$) was reduced to about 1/10. Figure 2 shows the effect of cooling by the drastic reduction of molecule contamination.

References

1) Sato N., Master Thesis, Tohoku University (2006).
2) Miyashita Y., in this report.

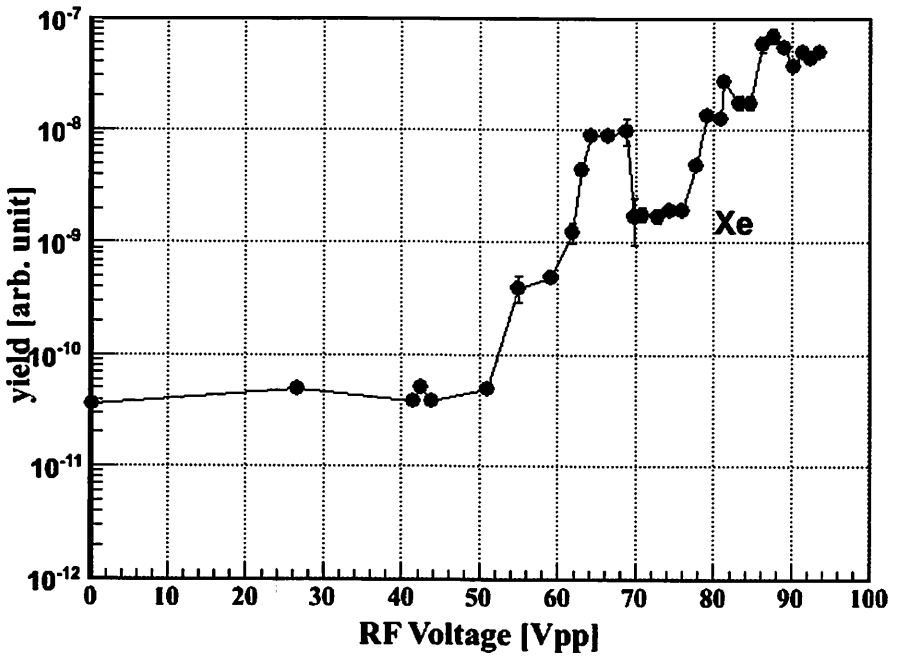

Figure 1. The effect of applying RF voltage.

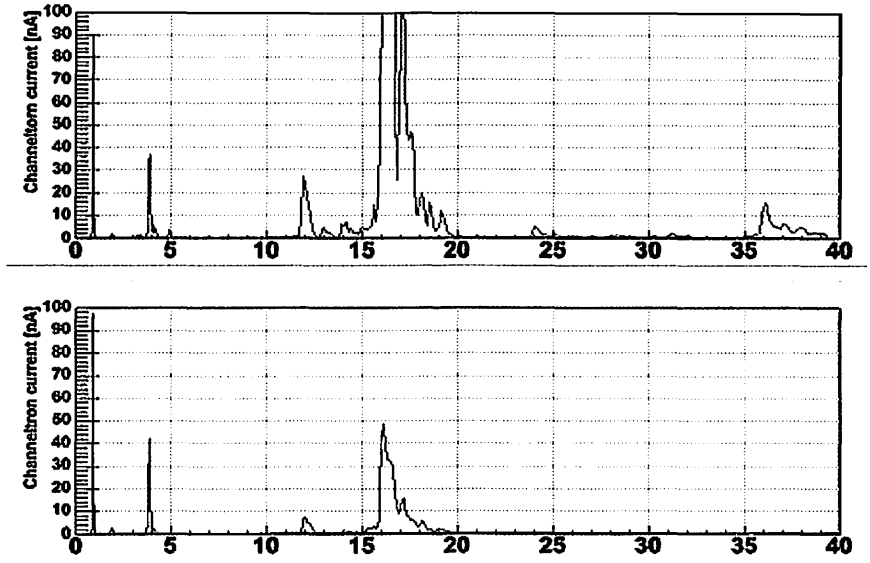

Figure 2. Mass spectrum of impurity molecules.

II. 3. Construction of Hyperball2 at CYRIC

Ukai M.[1], Fujita M.[1], Kinoshita S.[2], Koike T.[2], Ma Y.[2], Miura Y.[2], Miyashita Y.[1,2], Ohguma M.[1,2], Sato N.[1,2], Shinozuka T.[1], Shirotori K.[2], Suzuki T.[1,2], Tamura H.[2], Tateoka M.[1,2], Wakui T.[1], and Yamazaki A.[1]

[1]*Cyclotron and Radioisotope Center, Tohoku Universityn*
[2]*Department of Physics, Tohoku University*

A large acceptance germanium detector array, Hyperball2, was installed at CYRIC 33 course beam line and it realized performing the new type of the in-beam γ-ray spectroscopy experiment at this facility. Hyperball2 is consisted of fourteen Ge detectors having one crystal (Single type, 60%) and six Ge detectors having four crystals (Clover type, 20%/crystal). Figure 1 shows the schematic view of Hyperball2. All of them are the coaxial type and having a high-purity and n-type crystals. Each Single and Clover type Ge detectors were surrounding by six and twelve bismuth germanate (BGO) scintillation counters to suppress the Compton scattering events. Ge crystals covered a solid angle of 25% of 4 π sr. Total photo-peak efficiency of Hyperball2 was measured to be 5% for 1.33 MeV γ ray. Four-neighboring crystals in the Clover type detector enabled the "add-back"[1)] of the γ-ray energies and the measurement of the linear polarization of the detected γ rays.

The read-out electronics for the Ge detectors were suited to high counting rates. All the Ge detectors were equipped with transistor-reset type preamplifiers. The dead time due to the reset was as short as 15 μs.

ADC and TDC data of Ge detectors were collected via FERA bus to the Universal MEMory modules (UMEM[2)]) in a VME create. To reduce the DAQ dead time during the data read out from UMEM, two UMEM's were used as double-buffer mode. When the data were collected one UMEM, the data in another UMEM were read out via a VME-PCI interface and written on the data storage media. The switching timing of UMEM's was distributed by the TUL (Tohoku Universal Logic[3)]) which is a logic module boarding FPGA (Filed Programmable Gate Array). This read out system enabled the high rate data taking as 5 kHz trigger (300 words/ event).

The liquid nitrogen used to cool the Ge crystals was contained in a 3 litter dewar and re-filled every 12 hours in the beam time. Therefore, oxygen hazard monitors were also installed at the target room.

In 2005, the first in-beam γ-ray spectroscopy using Hyperball2 at CYRIC, the chiral doublet structure search in the A~ 80 region, was started[4]. Hyperball2 was once moved to the KEK-PS K6 beam line and used for the γ-ray spectroscopy experiment of the *p*-shell hypernucleus[5,6] (the predecessor of Hyperball2, Hyperball, was dedicated to the hypernuclear γ-ray spectroscopy). Afterwards, it came back to CYRIC and was used for further chiral doublet search experiment and another experiment, high spin isomer search experiment of Er isotopes[7].

References

1) http://www.canberra.com/products/1112.asp
2) Ajimura S., http://km.phys.sci.osaka-u.ac.jp/~ajimura/mem/
3) Nomura H., Master Thesis, Tohoku University (2006).
4) Suzuki T., et al., in this report.
5) Kinoshita S., Master Thesis, Tohoku University (2006).
6) Yue M., Master Thesis, Tohoku University (2006).
7) Fukuchi T., et al., in this report.

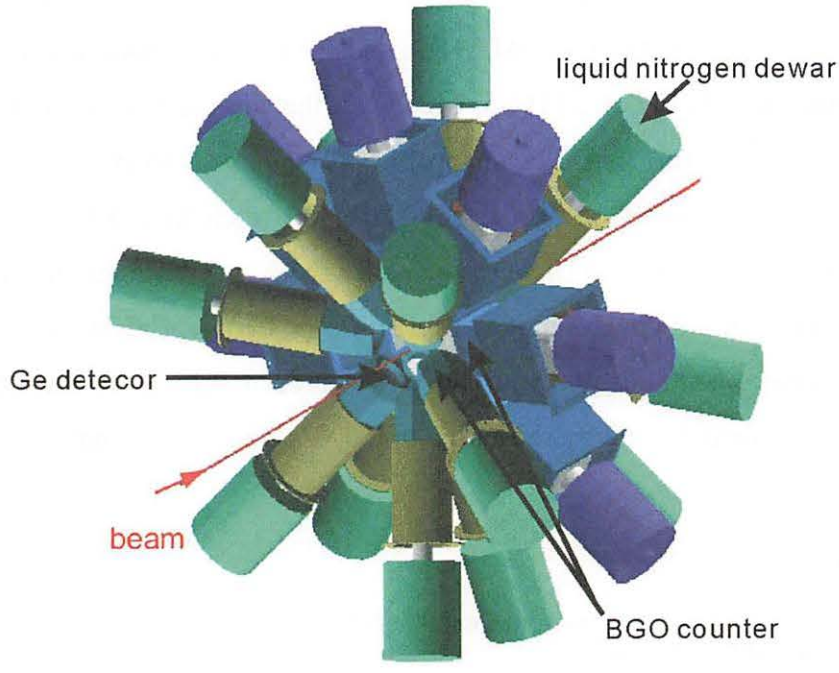

Figure 1. Schematic view of Hyperball2 installed at 33 course.

II. 4. High Resolution Beam Line at CYRIC

Itoh M., Okaumra H., and Ozeki K.

Cyclotron and Radioisotope Center, Tohoku University

The C4 beam line at CYRIC was designed to study nuclear physics by using the high resolution beam. It consists of 9 quadrupole and 2 dipole magnets. The layout is shown in Fig. 1. The total bend is 200 degrees, in two opposite direction 95 and 105 degrees segments, with an intermediate focus between the segments. Since the rigidity of the DEF magnet was less than those for the maximum beam energy of the upgraded AVF cyclotron, we replaced the DEF magnet to the old SW2 magnet which specifications were listed in Ref. 2. The ion optics of the C4 beam line for the dispersive mode was recalculated by the code GIOS. Figure 2 shows the result of the calculation including the extraction and additional beam lines (CP and C41). The total magnifications of Mx and My are 0.3 and 0.7, respectively. The momentum dispersion at the point of SLH4-5 is 21.5 m. Figure 3-5 show pictures of beam viewers at ALM4-1, ALM4-2, and the target position and results of the Monte Carlo simulation. In Fig. 5, SLH4-5, which was the slit to cut the beam horizontally, was closed up to 2mm. The initial beam profile was assumed to be (Xi, Ai, Yi, Bi, dPi)=(0.015 m, 0.001 rad, 0.008 m, 0.001 rad, 0.001), in which Xi and Yi were horizontal and the vertical beam sizes, Ai and Bi were angles for the X and Y directions, respectively. The dPi was the momentum deviation of the beam. In the case that SLH4-5 was closed up to 2 mm, the energy resolution of the beam was achieved 0.13 % in the Monte Carlo simulation. We confirmed the energy resolution of 0.4 % with the NaI counter at least.

References

1) Terakawa A., et al, CYRIC Annual Report (2002) 17.
2) CYRIC Annual Report (1980) 8.

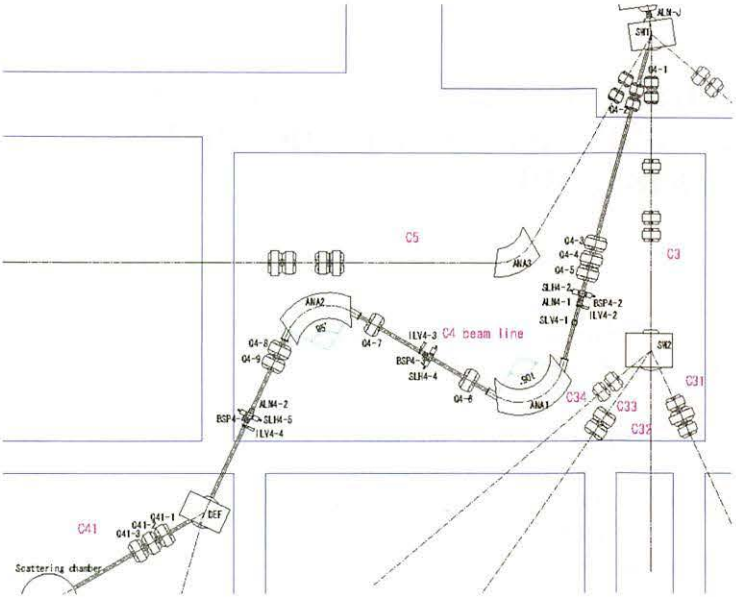

Figure 1. Layout of the C4 beam line.

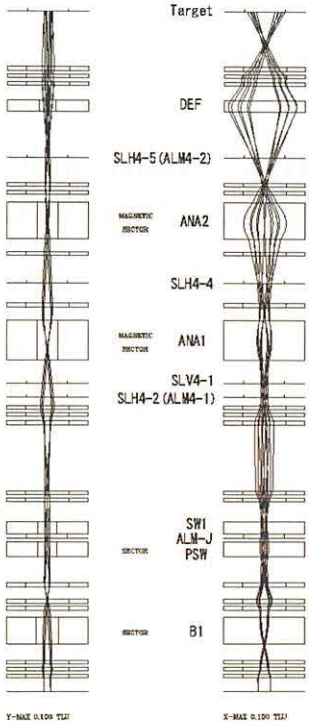

Figure 2. The profile of the dispersive beam transport.

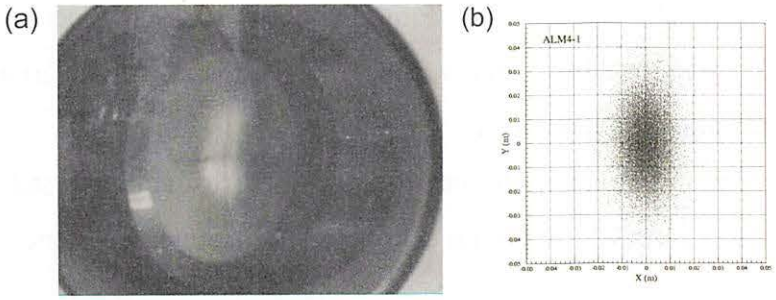

Figure 3.
(a) The beam profile at ALM4-1. (b) The result of the Monte Carlo simulation at ALM4-1.

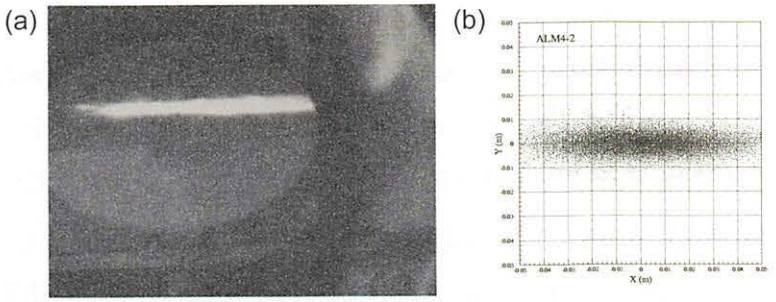

Figure 4.
(a) The beam profile at ALM4-2. (b) The result of the Monte Carlo simulation at ALM4-2.

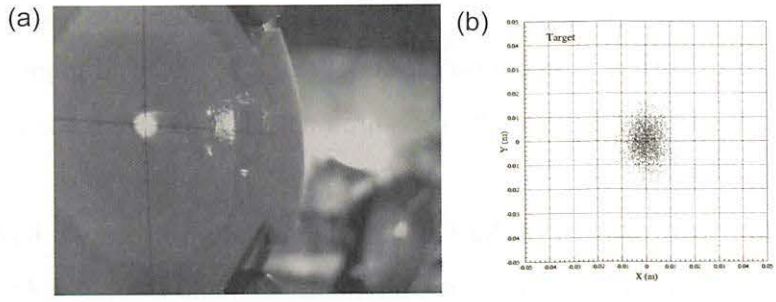

Figure 5.
(a) The beam profile at the target position. (b) The result of the Monte Carlo simulation at the target position.

II. 5. Study for NaI(Tl) and Scintillation Fiber with 80 MeV Proton Beam Toward ESPRI Experiment at NIRS-HIMAC, RIKEN-RIBF

Zenihiro J.[1], Matsuda Y.[2], Sakaguchi H.[3], Takeda H.[4], Iwao Y.[1], Matsumoto H.[1], and Itoh M.[5]

[1]Department of Physics, Kyoto University
[2]Department of Physics, Tohoku University
[3]Department of Applied Physics, Miyazaki University
[4]RIKEN
[5]Cyclotron and Radioisotope Center, Tohoku University

In recent years various new phenomena in unstable nuclei such as neutron skin or halo, have been a focus of international attention. RI beam facilities of the next generation, RIKEN-RIBF, GSI-SIS100/300, RIA at USA, and so on, are being built and various experiments are planned to confirm these phenomena.

We have already succeeded in extracting the neutron density distributions in stable nuclei by using intermediate energy polarized proton elastic scattering measurements at RCNP in Osaka University.

Now we are proposing experiments of **E**lastic **S**cattering of **P**rotons with **RI** beam (**ESPRI**) at NIRS-HIMAC and RIKEN-RIBF, and developing a new detector system composed of momentum tagging and tracking counters of the RI beam (Scintillation Fibers, two MWDCs), a Solid Hydrogen Target (SHT) and a Recoil Particle Spectrometer (RPS), to measure recoil protons in the SHT scattered by RI beam. The RPS shown in Fig.1, consists of MWDCs, plastic scintillators and finally fourteen-NaI(Tl) arrays. NaI(Tl) determines the total energy of recoil protons precisely. The Scintillation Fibers installed in the secondary beam line are used to tag the momentum of the RI beam at the focal plane of the beam line. Both of them are indispensable to the measurement of inverse kinematical proton elastic scattering with the RI beam.

In order to evaluate the performances of NaI(Tl) and Scintillation Fiber we have calibrated these detectors with 77.6 MeV proton beam at CYRIC in Nov. and Dec. of 2005.

NaI(Tl)

The size of NaI(Tl) rod is 2 inches square and 18 inches long and they cover the wide range of scattered angles of RPS from about 65 to 85 degrees in laboratory system. We measure their scintillating photons with HAMAMATSU R1307 photomultiplier tubes shown in Fig. 1, 2. The requirement for NaI(Tl) is to achieve energy resolution better than 600 keV (FWHM) independent of the energies of incident recoil protons up to 130 MeV and positions of NaI(Tl) rod. Thus we need to know the energy and position dependence of each NaI(Tl) crystal. We have already tested them with 12 MeV proton beam at Tandem Van de Graaff Accelerator Lab. at Kyoto University. The energy resolutions are about 1.5% (FWHM) and the square root gain of the left and right PMTs fluctuates about 5%. At this energy protons stop at the surface of NaI(Tl) crystal (about 1mm stopping range), so it is necessary to test with higher energy proton beam, that stops deep inside the NaI(Tl) crystal.

We used a faint proton beam of E_p = 77.6 MeV for this test experiment. The beam was directly injected into NaI(Tl) after the 10 mm thick brass collimater of 5 mm in slit width. In order to change the incident beam position on NaI(Tl) rod we mounted the NaI(Tl) detector on the stage which moved with the remote controlled pulse motor. The signals from PMTs were shaped and amplified by emitter followers and spectroscopic amplifiers ORTEC 671. Amplified signals were finally converted to digital data by peak hold ADC HOSHIN C008.

If doped Tl or crystal structure of NaI(Tl) were highly uniform, scintillating photons would be attenuated in a NaI(Tl) rod approximately as an exponential function of the length from the scintillating position to PMT. The square root of the left and right gains would be almost constant, independent of its position. But in fact, since NaI(Tl) crystals have non-uniformity to some extent, we cannot neglect the variations in square root gains (~6 %) which are larger than the resolutions (~0.5%) as shown in Fig. 3, 4. We have approximated the attenuation in non-uniform crystal by a simple sum of an exponential and a Gaussian. We fitted the left and right gains to this function with 5 parameters (Fig. 5), and got the calibrated square root gains again. By using these calibrated gains we found in Fig. 6 the variations become small nearly 600 keV in full width. Table 1 shows the fitting function and parameters used in this calibration.

At ESPRI experiments by using these calibrated gains we will be able to get the high resolution (~600keV) spectra of NaI(Tl) rods independent of incident positions, and to select elastic events.

Scintillation Fiber

Gas counters such as Low pressure MWPC and PPAC are often used as a position detector at a focal plane of a RI beam line. However, beam intensity, energy and so on are very influential in these performances. Moreover, usage of the counter gas can't release from danger. To avoid such problems, we have developed a simple one-dimensional Scintillation Fiber Detector (SFD).

The design of SFD is shown in Fig. 7. 2 mm square fibers are arranged in sixty rows. The effective area is 120 mm x 50 mm. Because of the very simple structure, areas of cladding material which are about 8% of fibers become a inefficient region. If the effective area is set up perpendicular to a beam axis, the inefficiency can't be bypassed. Of course, it isn't impossible to detect the particle passed through the clad area. But it only makes the operation more complex. Then, in order to achieve an efficiency of nearly 100 %, it was suggested that SFD is tilted toward the beam axis. Because the focal plane usually isn't perpendicular to the beam axis and the more tilting, the better the position resolution becomes, this method is fit to use.

In order to make sure this expectation, we measured the relation between the tilting angle and the efficiency using 45 MeV protons. Hit patterns and timing information of SFD were measured by multi-hit TDC AMSC 64ch AMT-VME module, via Flat Panel Photomultiplier Tube (FPPMT) HAMAMATSU H8500 and amplifier-shaping-discriminator (ASD) Gnomes Design GNA-180, of which the time constant was 16 nsec and the threshold was set to –30 mV on the chip. To monitor cross talk events occurred in FPPMT, charge pulses from the dynode are measured by ADC LeCroy 2249A, via pre-amplifier, is a same amplifier of ASD, and PMT amplifier LeCroy 612A.

Efficiency curves of each tilting angles (0, 5, 10, 15, 30, 45, 60 degrees) are shown in Fig. 8. A counting rate was about 1 kHz during measurement. An efficiency of cluster multiplicity 1 (C1), means that SFD can determine hit positions without any delicate analyses, reaches nearly 100% at more than 15 degrees. Considering the cladding thickness, it can be explained an increase of the efficiency from 0 degrees to 10 degrees.

When the operation HV becomes more than 500 V, an efficiency of cluster multiplicity 2 (C2) increases. It is caused by cross talk events in FPPMT. It can be confirmed to see correlations between time widths of anode signals and charges of dynode signals. A distribution of the sum of time widths for each cluster is shown in Fig. 9. Hatched areas mean cross talk events and can be removed by this analysis. Two bumps of true hits region at 30, 45 degrees are caused by nonlinear relation between energy loss and

time widths of anode signals.

From these measurements, it was confirmed SFD have nearly 100% detection efficiency. Moreover, for 60 degrees, we could get fairly good position resolution (< 1mm full width).

The response for high counting rate (10^6 Hz) and heavy ions were also examined with 390 MeV/u ^{22}Ne primary beam and its secondary beam at HIMAC and the performance didn't go down. So SFD is installed in a momentum dispersive focal plane of SB2 course of HIMAC now. Because momentum dispersion of SB2 course is 2 cm/%, we will succeed in getting good momentum resolution (<0.1%) for beam particles.

References

1) Sakaguchi H.,et al., Phys. Rev. **C57** (1998) 1749.

Table1. The parameters of fitting function (exp + Gaussian). $p_1 \times \exp\left(-\frac{x-l}{p_2}\right) + p_3 \times \exp\left(-\left(\frac{x-p_4}{p_5}\right)^2\right)$

S/N		p1	p2	p3	p4	p5
030320-7	Left	2733.68	-1624.82	265.567	80.295	126.83
	Right	2091.85	257878	1035.4	-171.75	138.36
030527-3	Left	3198.26	-1202.99	156.5	37.507	56.746
	Right	3125.99	1713.67	37.157	17.5	31.707
030527-4	Left	3654.76	-807.673	112.77	-208.76	38.875
	Right	3167.74	1559.21	53.934	37.235	33.438

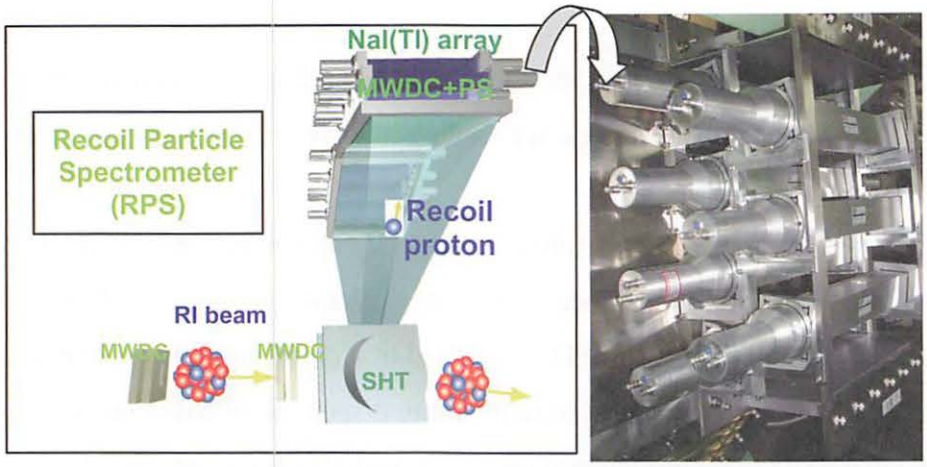

Figure 1. Schematic view of Elastic Scattering of protons with RI beam and photo of NaI(Tl) array.

Figure 2. NaI(Tl) rod of 2 x 2 x 18 inch with Hamamatsu R1307 PMT.

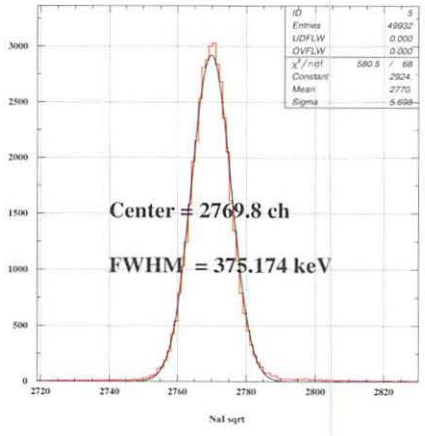

Figure 3. The resolutions at the center of a NaI(Tl) rod.

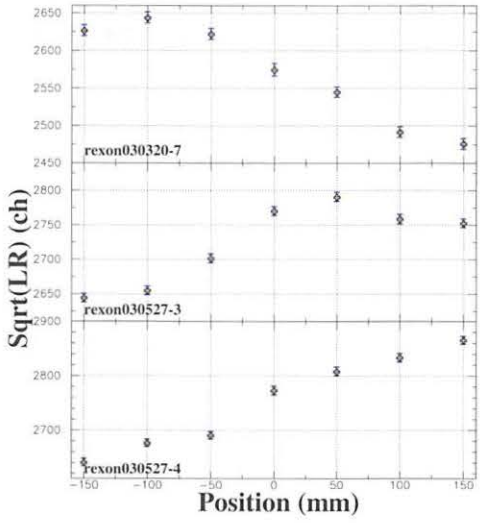

Figure 4. Gains and resolutions of each NaI(Tl) rod. While the resolutions are within 0.5% (FWHM), fluctuation of the gains is about 6%.

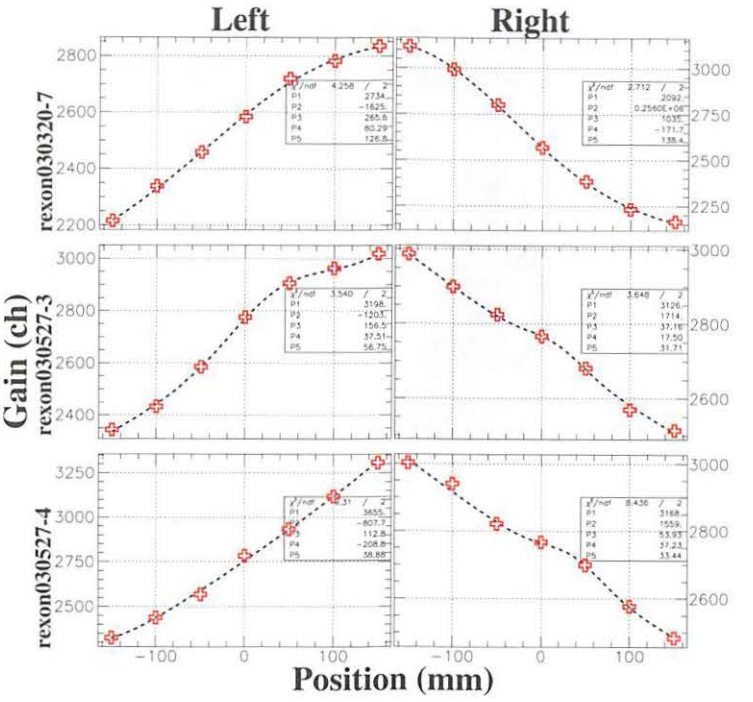

Figure 5. Left and right gains of each position in each NaI(Tl) rod. We fitted these to a function of an exponential and a Gaussian.

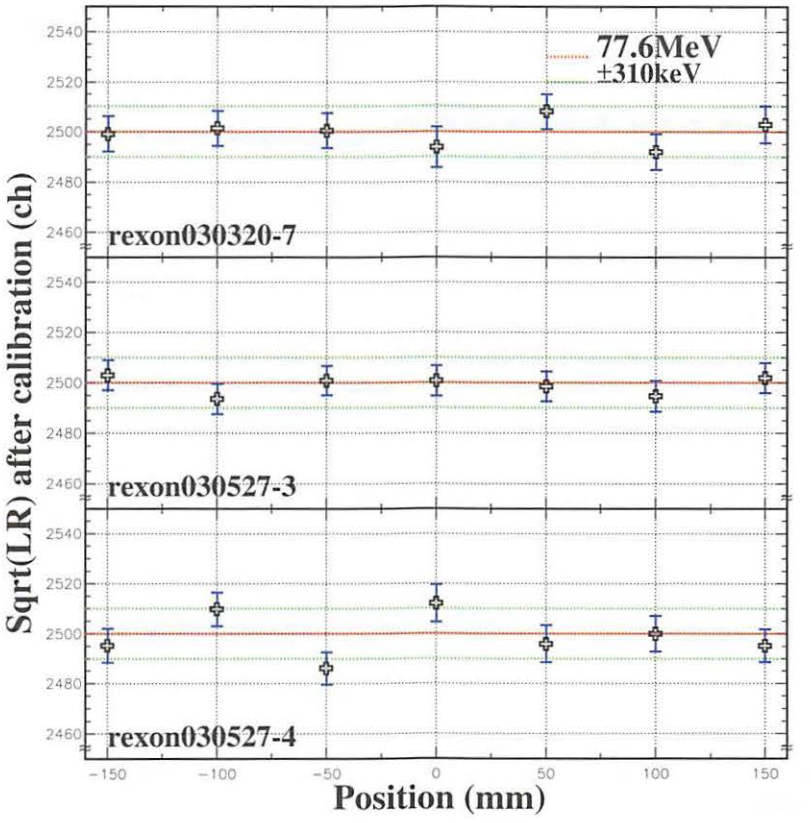

Figure 6. Each square root gains after calibration. They are within just about 600 keV in full width.

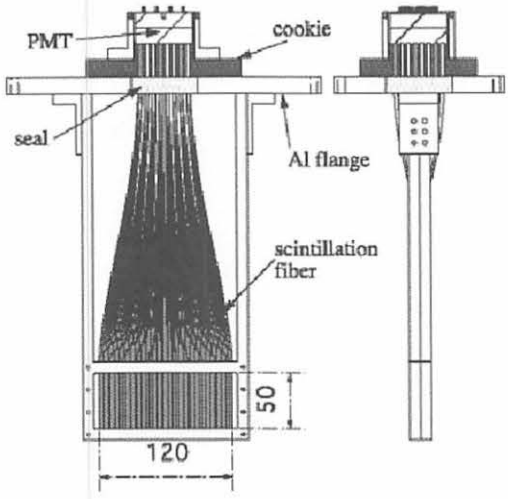

Figure 7. The schematic illustration of SFD.

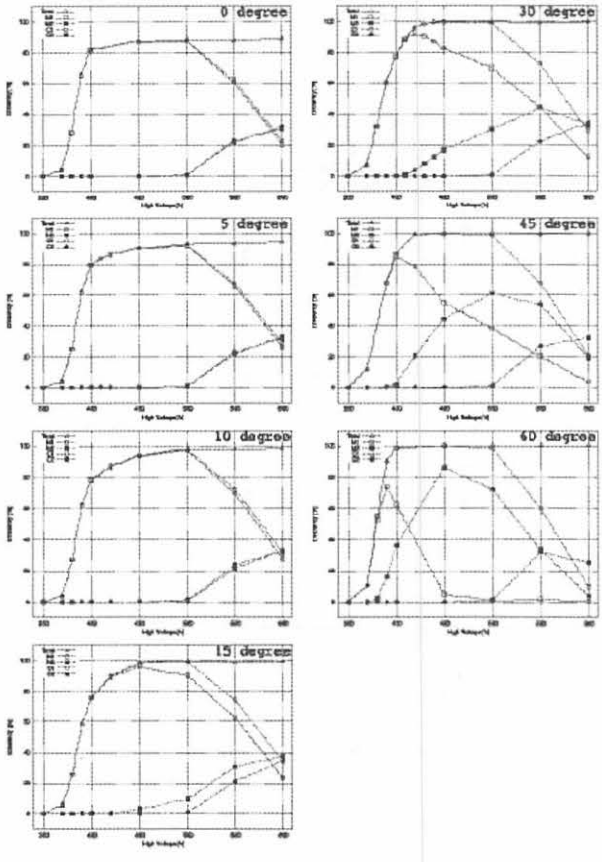

Figure 8. Efficiency curves for 45 MeV protons at various angles. Open triangles show the total efficiency: the efficiency of fiber multiplicity 1 (M1, open squares), of fiber multiplicity 2 (M2, closed circles), of cluster multiplicity 1 (C1, open circles), and of cluster multiplicity 2 (C2, closed circles).

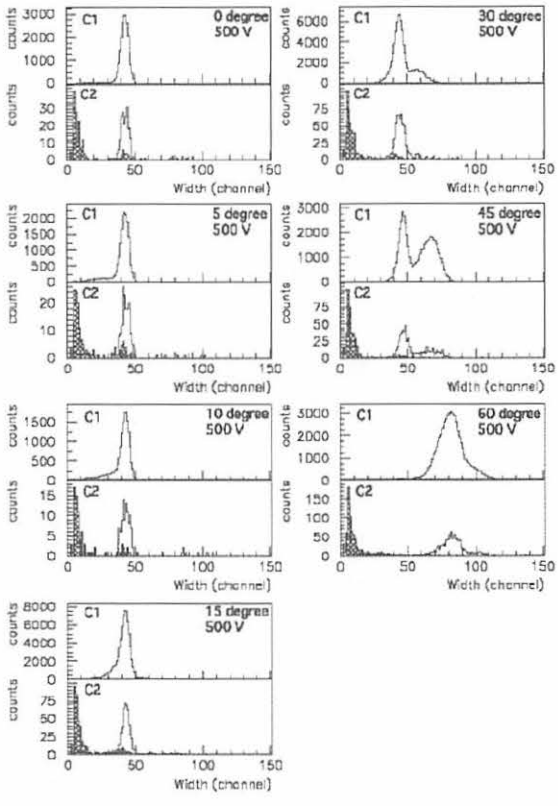

Figure 9. The distribution of the sum of time widths for each cluster. Hatched areas correspond cross talk events.

II. 6. Development of a Novel Fast-response Neutron Beam Monitor

Nakhostin M.[1], Baba M.[1], Oishi T.[1], Itoga T.[1], Kamata S.[1], Unno Y.[1], and Otsuki T.[2]

Cyclotron and Radioisotope Center, Tohoku University
Laboratory for Nuclera Study, Tohoku Univeristy

Introduction

During the last year we have been involved with the development of fast response neutrons detectors. Such detectors are required for couple of applications. A prominent example of such applications is intense neutron beam monitoring in next generation of accelerator-based neutron sources. Such accelerators are now under construction in several countries. For example, in Japan, Japan proton accelerator research complex (J-PARC) is being built. In this project very intense thermal neutron beams will be available and therefore appropriate neutron detectors are required to provide information on the neutron beam such as intensity, spatial and time distribution. In such a harsh environment, detector radiation durability is of crucial importance as well.

This report is devoted to the preliminary results of a novel fast neutron beam monitor, which is based on the parallel plate avalanche chamber (PPAC). Choice of PPAC was made due to its fast response, radiation resistance, high-count rate and position measurement capability.

Parallel plate avalanche counters

A PPAC consists simply of two thin metalized foils mounted in parallel, with a small gap of a few mm in between (Fig. 1). PPAC is employed at a few torr of a hydrocarbon gas like isobutene, and under a strong electric field E in the gap. Due to the high-reduced electric field, E/P, (P is gas pressure) released electrons by ionizing radiations initiate electron avalanche and form a very fast signal (~1 ns rise time) due to the high drift velocity of electrons. Detector can be easily made position sensitive, if an electrode is made of a grid of parallel thin wires or parallel strips. Then, position data can be obtained by means of conventional methods like delay line or charge division method.

The neutron-sensitive PPAC

Our prototype detector consists of three parts: The converter sheet, which produces recoil charged particles, the PPAC and detector housing.

Converter; the converter is a thin layer of ^{6}LiF evaporated on aluminum backing. In order to obtain a good pulse height spectrum converter sheet is placed a few centimeters far from PPAC.

PPAC; a schematic illustration of our PPAC has been shown in Fig. 2. It consists of an aluminized Mylar foil electrode as anode and cathode made of a grid of gold-plated tungsten wires (30 μm) with 2 mm spacing. Anode-cathode gap is 2 mm and position information is obtained by using delay-line technique.

Detector housing; detector assembly is mounted in the detector housing, which is made of aluminum. The detector is operated in the gas flow mode with isobutene gas.

Test experiments results

Test experiments were carried out with using an Am-Be neutron source. Fast neutrons were thermalized by employing appropriate thickness of polyethylene. A typical detector pulse height spectrum is shown in Fig. 2. Figure 3 shows a typical signal waveform, obtained with fast current sensitive preamplifier (VT120, Ortec). The signal rise time of ~ 4 ns and ~ 6 nsec pulse width (FWHM) is easily obtainable. Such signals are well suited for the time dependent beam monitoring applications under high count rates.

A projection of position spectrum is shown in Fig. 4. The obtainable spatial resolution is equal with wires spacing (2 mm). Delay line system was composed of delay chips with 3 ns delay between adjacent wires and 100 ps time resolution.

Summary and conclusion

A novel neutron beam monitor with very fast response and position measurement capability has been successfully developed. Fast signals with ~ 4 ns rise time and ~6 ns pulse width together with 2 mm position accuracy were easily obtained. This detector looks very promising for beam monitoring in J-PARC project and so on.

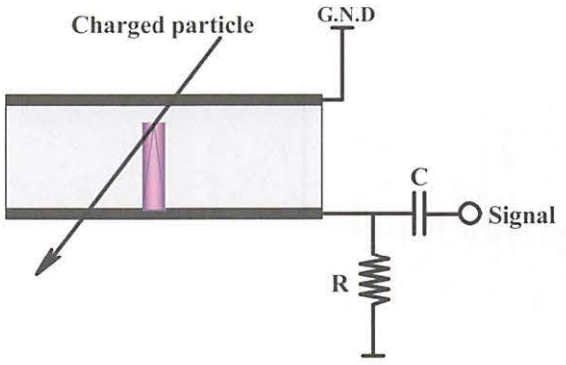

Figure 1. PPAC principle of operation.

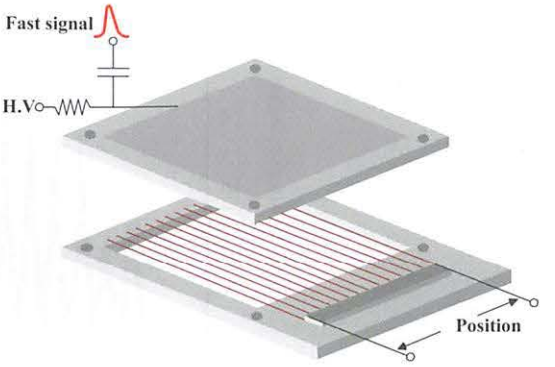

Figure 2. Schematic representation of our PPAC.

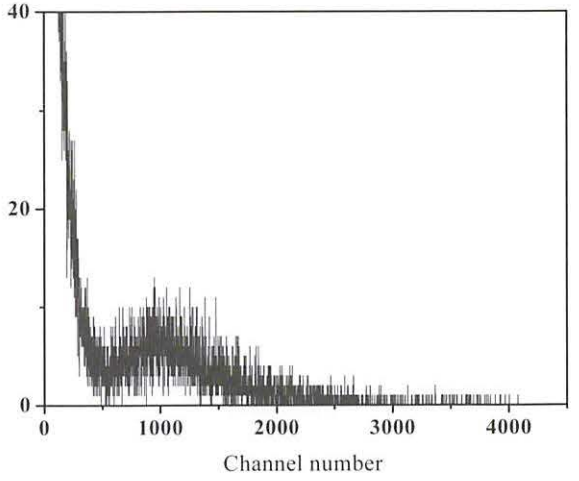

Figure 3. Typical pulse height spectrum.

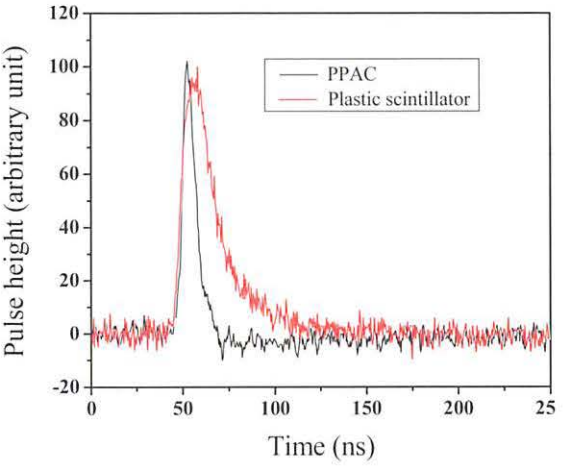

Figure 4. Typical signal waveform, compared with scintillator. Scintillator shows much longer decay time.

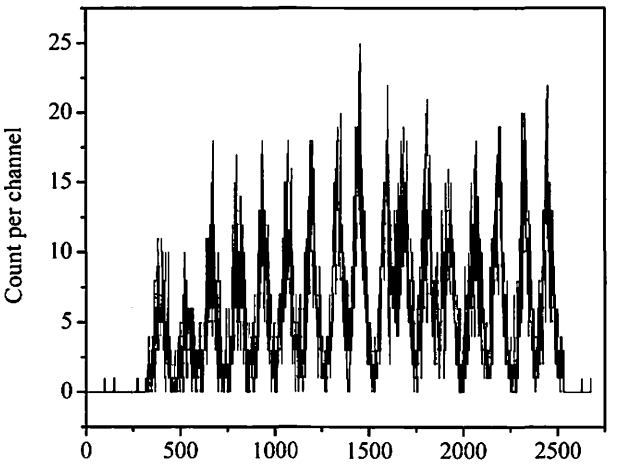

Figure 5. Results of position measurement according to delay line method.

III. NUCLEAR ENGINEERING

III. 1. Tail Correction in Quasi-monoenergetic Neutron Source

Kamata S., Itoga T., Unno Y., and Baba M.

Cyclotron and Radioisotope Center, Tohoku University

Mono-energetic neutron source plays an important role for cross-section measurement, dosimetry development, testing of semi-conductors for single-event effects and so on. In the energy region above 20 MeV, the ^{7}Li(p,n) and ^{9}Be(p,n) neutron source have been employed as an intense "monoemnergetic" neutron source. Actually, however, they are not purely mono-energetic but quasi-monoenergetic because continuos spectrum neutrons (tail) are produced from breakup reactions and accompany with the main peak neutrons.

In the measurement using such sources, large errors comes from the background due to low energy tail as well as limited intensity of the peak neutrons. To improve the situation, we have installed and characterized an intense quasi-monoenergetic neutron source at CYRIC[1]. Now we are promoting the study of the applicability of the "tail correction" method which is the correction for backgrounds due to tail, reported by R.Nolte et al. for 200 MeV proton beams[2]. Their tail correction is based on the fact that the high-energy peak neutron decreases rapidly with angle whereas the shape of the "tail" neutrons does not change considerably. Therefore we can get corrected quasi-monoenergetic neutron spectrum by subtracting the data in larger angle from that in smaller angle (zero-deg.).

In order to inspect the applicability of this "tail correction method" in our energy range, we carried out experiment for 70 MeV protons and obtained neutron spectrum from a Li target, and Be target at 5th target room at CYRIC. The experimental method was almost the same with these in previous experiments[3]. A thin target of lithium (4.69 mm thickness), a thin target of beryllium (3.0 mm thickness) and a thick target of copper (10 mm thickness) in order to determine the timing of prompt gamma ray event were prepared.

The neutron spectra were measured with time-of-flight method using a beam

swinger system over a wide range (5-70 MeV) of secondary energies at seven laboratory angles for lithium and nineteen angles for beryllium respectively, between 0- and 110-deg. The results are shown in Fig. 1 and Fig. 2. These figures show that peak neutrons from lithium and beryllium tend to decrease very rapidely with the neutron emission angle but the low-energy tail show much milder angle-dependence.

Let two neutron spectra measured at 0 deg. and θ (larger than 0 deg.) be φ_0 and φ_θ. We normalize the spectra to the same flux in the low-energy tail region by multiplying the spectrum φ_θ by a factor k. The normalize factor is determined in order to avoid negative value of subtracted spectrum. The subtraction equation as follows:

$$\Phi = \varphi_0 - k \cdot \varphi_\theta$$

where Φ is the corrected spectrum,

φ_0 is spectral fluence at angle 0 deg.

φ_θ is spectral fluence at angle θ.

k is a normalize factor.

Figure 3 indicates 0 deg. spectrum and 30 deg. spectrum normalized to 0 degree's low-energy tail region.

With a view to select optimum angle for the "tail correction", we evaluated the three quantities: 1) peak-to-total flux ratio, 2) chi-square test on each energy bin, 3) feature of the spectrum. Table 1 summaries peak-to-total flux, and table 2 shows the results of chi-square test. From the three quantities, 30 degree seems to be an optimum angle for the tail correction. Figure 4 indicates subtracted spectrum of neutrons from lithium and beryllium respectively. In the near future, we will prepare 30-deg. port by punching a hole in a collimator and apply the port to the neutron cross section measurement and semi-conductor single-event upset experiment.

References

1) Meigo S., Nucl. Instr. Method in Phys. Res. A**400** (1997).
2) Nolte R., et al., Nucl.Instr. Method in Phys. Res. A**476** (2002).
3) Hagiwara M., et al., Fusion Sci. Tech **48** (2005).

Table 1. Peak to total ratio.

	Li	Be
FOM	72.7 %	62.4 %

Table 2. Result of chi-square test.

	Li	Be
χ^2	5.17×10^{7}	1.12×10^{10}

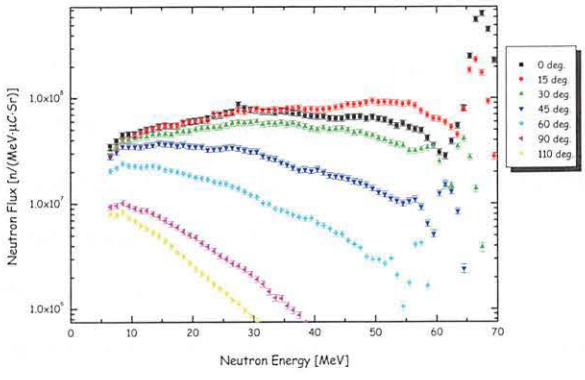

Figure 1. Neutron spectrum for Li.

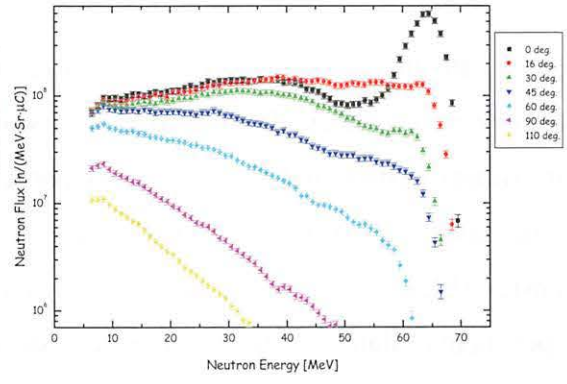

Figure 2. Neutron spectrum for Be.

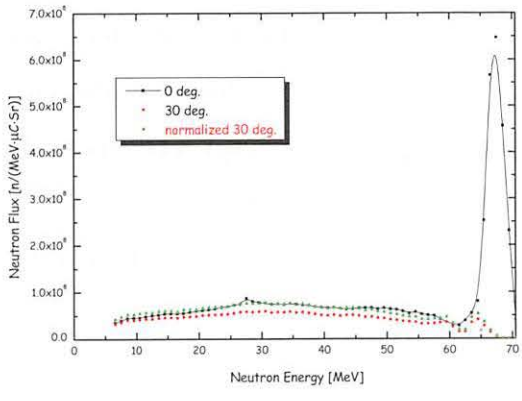

Figure 3. Normalization to 0 deg. low-energy.

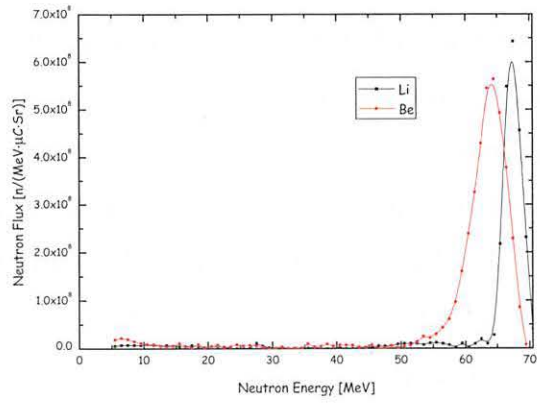

Figure 4. Subtracted spectrum.

III. 2. Study of low energy fragment measurement using energy time of flight method

Oishi T.[1], Sanami T.[2], Hagiwara M.[2], Okuji T.[1], Itoga T.[1], and Baba M.[1]

[1]Cyclotron and Radioisotope Center, Tohoku University
[2]High energy accelerator research organization

In the evaluation of the single event effects (SEE) which cause semiconductor memory errors, detailed knowledge are required on the charge, mass, and energy not only for primary particle but also secondary particles produced in semiconductor. In particular, fragments produced by ten's of MeV nucleons are important due to the large liner energy transfer (LET) of fragment and high flux of incident particles in space. However, the experimental data of the fragment production are very few due to the experimental difficulty of a small amount of produced fragments, large energy loss, and high back ground of light particles. Especially, the fragment production cross-section in low energy region will be very important to evaluate the SEE because the fragments production cross-section increases toward lower energy. However there is no experimental data. We have been conducting measurement of fragment production using specially developed Bragg curve counter and the energy time-of-flight method. In this report, the energy-TOF method is discussed to measure the fragment production cross-sections in low energy region,

The Energy Time of flight (E-TOF) method can identify the mass of the particles using the energy and TOF information as explained by the equation:

$$E = mv^2/2 = m/2 \times (L/t)^2 \cdots (1),$$

where E is the energy of the particle, m is mass of the particle, L is the flight pass, t is TOF. The advantage of this method is the wide energy range to be covered and there is no low limit in principle. The experiment was carried out in the No. 2 target room of CYRIC. The experimental geometry is shown in Fig. 1. The fragments which was produced by 70 MeV protons were detected by micro-channel plate (MCP) and SSD. Fast preamplifiers were used to achieve good timing resolution over a wide energy region. In the first experiment, analog circuits were used for a signal processing but there were distortions in

low energy region due to "walk" on the timing detection. To overcome this problem, the digital signal processing (DSP) technique was introduced. The DSP is a data handling method in which each signal waveform from a detector is acquired as digital data, and the information on the radiation can be derived through the analysis of the signal waveform using computers. By applying DSP, even small pulses were could be without the "walk" by ideal constant fraction discrimination enabled by DSP.

The two dimensional plot of the energy-TOF distribution is shown in Fig. 2. The horizontal axis is energy of the fragments and the vertical axis is $t\sqrt{E}$ which is derived from eq.1. Boundary energy to identify the particles was investigated. Dispersion of each mass line is derived by the propagation of errors and expressed by eq.2, where σ_t and σ_E is the resolution of TOF and energy, respectively.

$$\sigma_{t\sqrt{E}} = \sqrt{E\sigma_t^2 + \frac{t^2}{4E}\sigma_E^2} \cdots (2),$$

σ_t and σ_E were adjusted by the experimental value. The boundary energy was found by changing the resolutions. As a result, the boundary energy became lower owing to improved energy resolution while the boundary energy does not change from the old data with infereior TOF resolution. Additionally it became clear that 2.5% energy resolution is needed to identify above 2 MeV of the carbon particles.

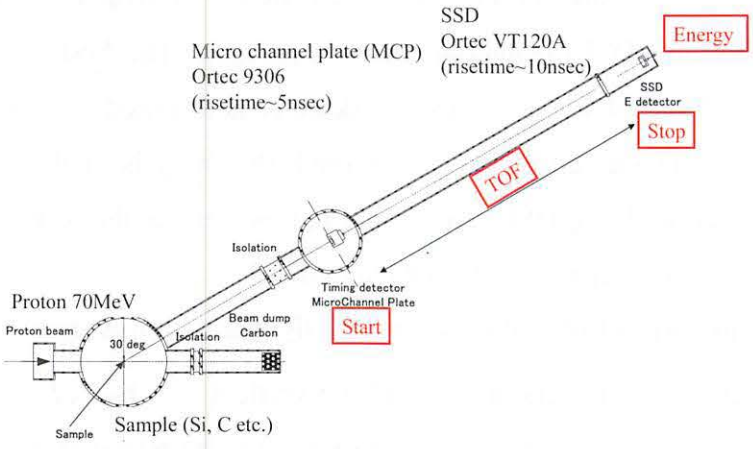

Figure 1. The geometry of E-TOF experiment.

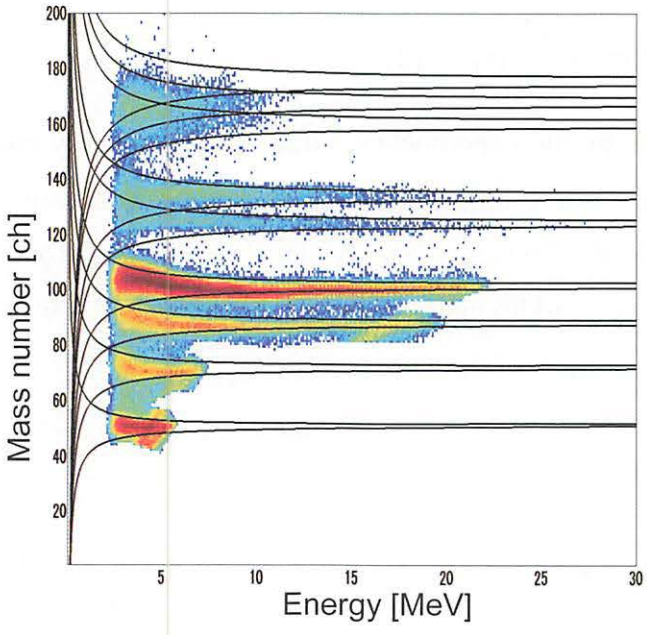

Figure 2. Mass identification by experiment and calculation.

III. 3. Experimental Study on Fission Cross-sections of Actinides using Digital Signal Processing

Takahashi W.[1], Oishi T.[1], Nakhostin M.[1], Yamauchi T.[1], Baba M.[1], Yuki H.[2], Ohtsuki T.[2], Hori J.[3], and Yashima H.[3]

[1]*Cyclotron and Radioisotope Center, Tohoku University*
[2]*Laboratory of Nuclear Science, Tohoku University*
[3]*Kyoto University Research Reactor Institute*

For effective transmutation of minor actinide (MA) in nuclear wastes by Accelerator Driven System (ADS), a variety of nuclear data is needed. However, the nuclear data of actinides are not enough both in quality and quantity. Therefore, new experimental data is required to improve the precision of the data[1-3].

A lead slowing-down spectrometer has been used effectively to measure the fission cross-sections of MA owing to very high neutron flux[1-3]. However, the energy range of the measurement was limited below ~10 keV because accelerator-synchronized electromagnetic noise piled up on high-energy events and disturbed to detect them. To solve the problem, we tried to extend the energy range of measurement to higher energy by reducing the electromagnetic noise by use of a digital signal processing (DSP) technique[4].

The lead slowing-down spectrometer is based on the fact that lead isotopes are characterized by a very small capture cross-section, and scattering is essentially isotropic and kinetic energy loss is only ~1% per collision. As a consequence, there is a statistical correlation between slowing-down time t and the mean kinetic energy E of neutrons[5]. In the lead-slowing-down spectrometer, the neutron intensity is thousands times as high as or more than those in conventional neutron time-of-flight (TOF) spectrometer owing to a short distance from the source. Therefore, the lead slowing-down spectrometer is very effective for the measurement of fission cross-section measurement with small amount samples and/or low cross-section, and under high background by α-decay. However, the energy resolution of lead slowing-down spectrometer is about 40%[6] and not good.

The present measurement was carried out using Kyoto University lead slowing-down spectrometer (KULS) driven by an 46 MeV electron linac in KURRI. The

KULS is a cube of 1.5×1.5×1.5 m^3 consisting of lead blocks and set on a steel platform cart in the linac target room. At the center of the KULS, pulsed fast neutrons are produced by the photo-reaction in a tantalum target in cylindrical titanium casing, which is air-cooled with compressed air. The cross sectional view of the KULS is shown in Fig. 1.

An ionization chamber with two parallel plate electrodes was employed for the detection of fission events. Since MA and ^{235}U deposits on backside each other, the chamber is called a back-to-back (BTB) type double fission chamber. The cross sectional view of the BTB chamber is shown in Fig. 2.

The pulse width of electron beam was generally 33 ns in FWHM and the frequency was 100 Hz as the optimum value for KULS. The beam current on the target was around 10.5 to 12.4 μA. The waveform signals of the fission chambers were digitized and recorded by a digital storage oscilloscope (DSO), LeCroy WavePro 7000. The linac RF signal was used as trigger of the DSO.

Data analysis was performed with the DSP method. The pulse height data and the slowing-down time data were deduced by processing the waveform data. The fission fragment pulses were discriminated from the α-particles pulses by the pulse height. The electromagnetic noises induced by the linac pulse proved to be almost same in shape for all pulses. Therefore subtraction of the typical waveform data of electromagnetic noise from fission signal waveform enabled us to eliminate the electromagnetic noise and count the higher energy neutrons (Fig. 3). Accordingly, we could extend the energy range of measurement to about 100 keV or more[4].

Preliminary results for neutron induced fission cross-sections of ^{237}Np and ^{241}Am are shown in Fig. 4 and Fig. 5, respectively. The present data are favorably compared with the evaluated nuclear data of JENDL-3.3, ENDF/B-IV and JEFF-3.1 and other experimental data.

References

1) Kobayashi K., et al., J. Nucl. Sci. Technol. **36** (1999) 549.
2) Kai T., et al., Annals Nucl. Ener. **28** (2001) 723.
3) Kobayashi K., et al., J. Nucl. Sci. Technol. **36** (1999) 20.
4) Oishi T., et al., J. Radiat. Protect. Bull. (2005) 148.
5) Granier T., et al., Nucl. Instr. Method Phys. Res. A**506** (2003) 149.
6) Kobayashi K., et al., Nucl. Instr. Method Phys. Res. A**385** (1997) 145.

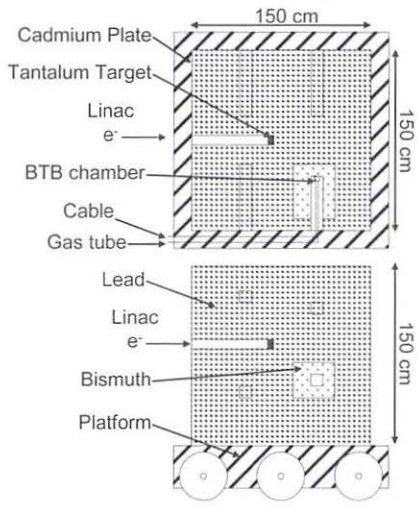

Figure 1. The cross sectional view of the KULS.

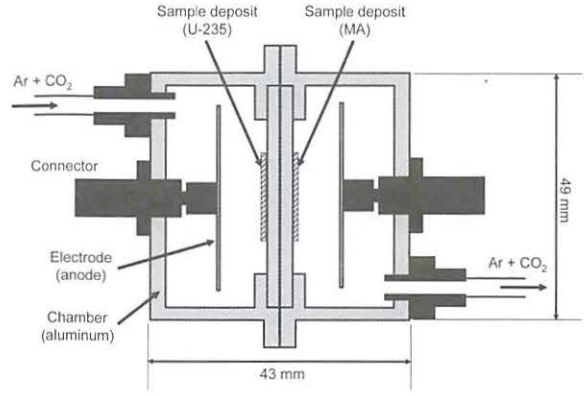

Figure 2. The cross sectional view of the BTB chamber.

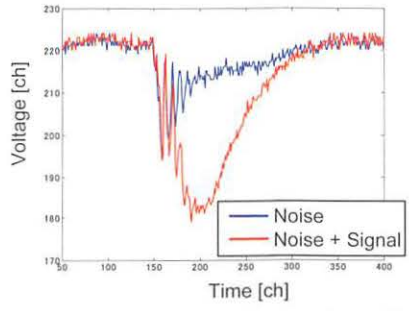

Figure 3. The signal wave form from fission chamber; electromagnetic noise overlaps on the signal and disturbs the detection of signal.

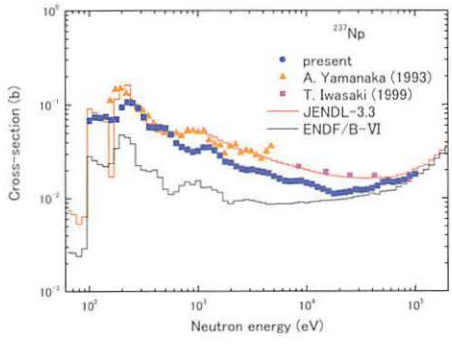

Figure 4. The neutron induced fission cross-section of ^{237}Np.

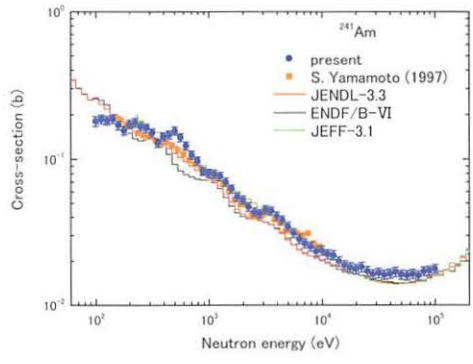

Figure 5. The neutron induced fission cross-section of ^{241}Am.

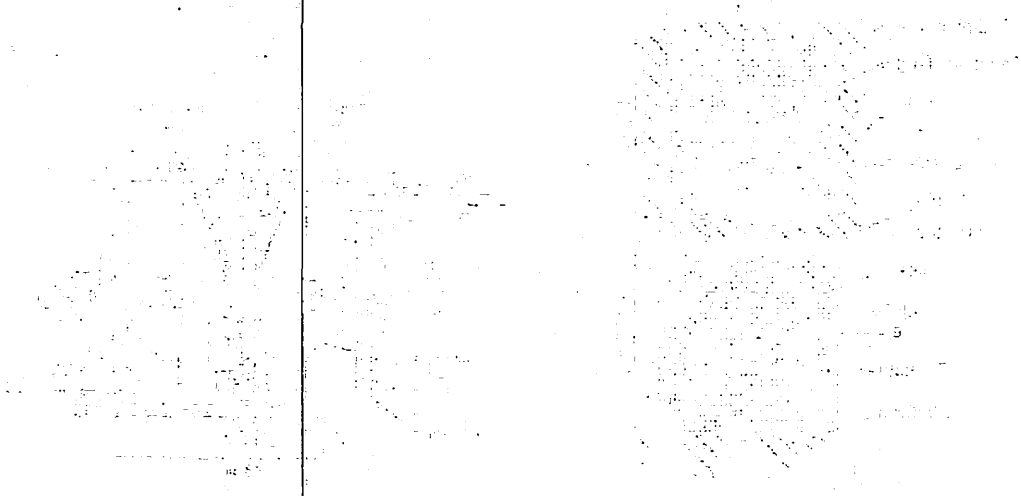

IV. NUCLEAR MEDICAL ENGINEERING

IV. 1. Beam Irradiation System for Proton Therapy at CYRIC

Terakawa A.[1], Ishizaki A.[1], Totsuka Y., Honda T.[1], Miyashita T.[1], Arikawa J.[1], Togashi T.[1], Ishii K.[1], Itoh M.[2], and Orihara H.[3]

[1]*Graduate School of Engineering, Tohoku University*
[2]*Cyclotron and Radioisotope Center, Tohoku University*
[3]*Department of Physics, Tohoku Institute of Technology*

The horizontal beam-irradiation system for proton therapy was installed at CYRIC to develop the advanced particle irradiation technique and study superior therapeutic effects of proton therapy using small animals. As the beginning phase of the proton therapy at CYRIC we have performed basic experiments for delivering a therapeutic proton beam which makes a uniform radiation field and a spread-out Bragg peak (SOBP) using the present system. In this report the results of the performance tests for the irradiation system will be described.

Figure 1 illustrates the beam irradiation system consisting of two dipole magnets, a scatterer, a ridge filter, a beam monitor, range shifter and collimators. The target position is about 4 m downstream of the magnet. A proton beam delivered into the irradiation system is spread by a wobbler method[1,2] with the magnets and the scatterer so that the uniform radiation field having a diameter of up to 10 cm for a 90 MeV-proton beam is produced at the target position. The ridge filter modulates the energy of the monoenergetic beams to produce the SOBP whose width is equal to the maximum width of the cancer in the beam direction. Dose delivery is controlled with the beam monitor of a parallel-plate ionization-chamber design. Dose calibration of the beam monitor is performed with a standard ionization chamber.

The experiments for producing a uniform field based on the wobbler method and the SOBPs with the ridge filters were performed using a 80 MeV-proton beam from the AVF cyclotron at CYRIC. The two-dimensional beam fluence at the target position was measured with an Imaging Plate (IP)[3]. The depth-dose distribution was measured with an IP which was inserted in polymethyl metacrylate (PMMA) at 20° with the beam axis. The dose rate was a few mGy/min at the SOBP.

Figure 2 shows typical results for a uniform field of about 80 mm in diameter and the depth-dose distribution in PMMA. The flatness of the field is less than 5% which has sufficient quality for proton therapy, while the flatness of about 6% for the SOBP should be improved.

In the following phase we are planning to perform not only the clinical experiments using a rat but also the beam-delivery experiments based on a spot-beam scanning for development of the advanced irradiation technique.

References

1) Akagi T., et al., Phys. Med. Biol. **48** (2003) N301.
2) Tamura H., et al., Japan. J. Med. Phys. **18** (1998) 42.
3) Fuji Photo film CO., LTD., http://www.fujifilm.co.jp/bio/si_imgplate/imgplate.html.

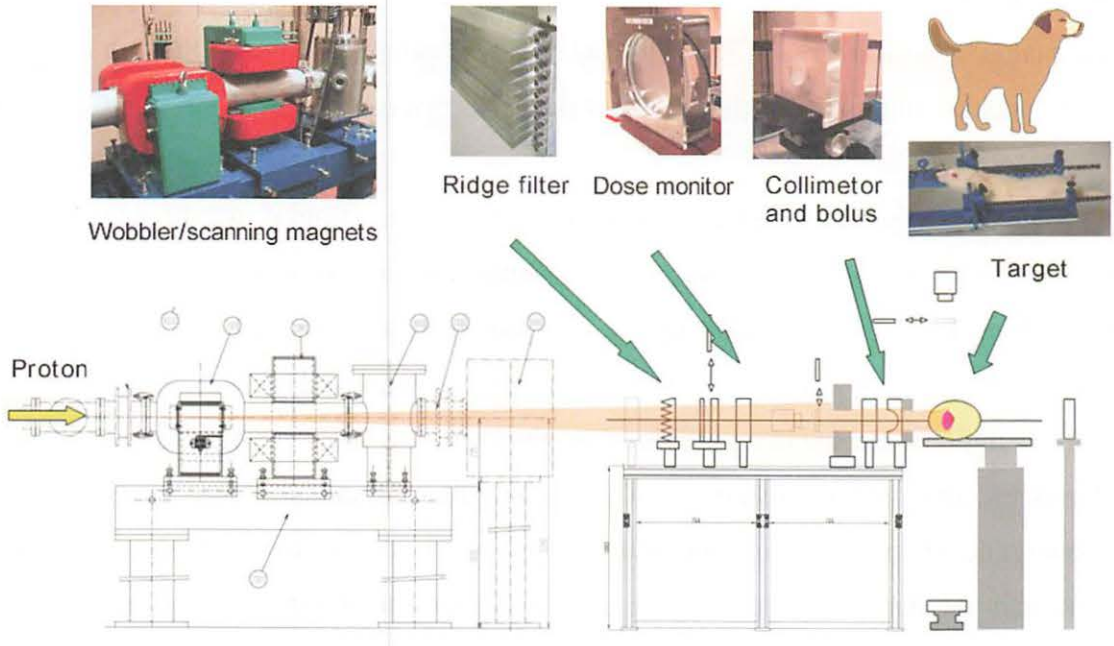

Figure 1. Schematic layout of the beam irradiation system for proton therapy at CYRIC.

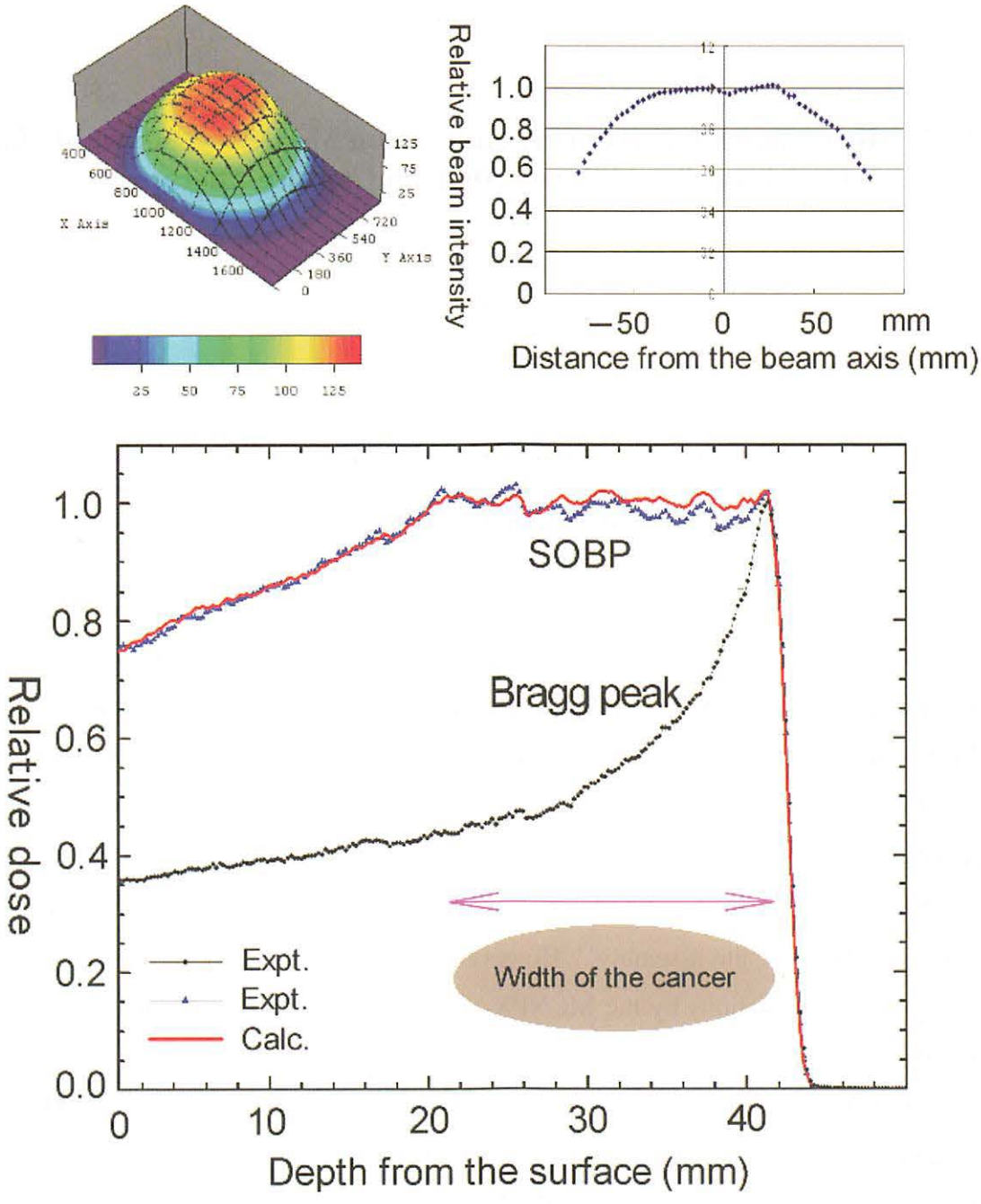

Figure 2. Uniform field of about 80 mm in diameter (upper) and depth-dose distribution in PMMA (lower).

IV. 2. Benchmark Experiments on Neutron Moderator Assembly for Cyclotron-Based Boron Neutron Capture Therapy

Unno Y.[1], Yonai S.[2], Baba M.[1], Itoga T.[1], Kamada S.[1], Tahara Y.[3], and Yokobor H.[4]

[1]*Cyclotron and Radioisotope Center, Tohoku University*
[2]*National Institute of Radiological Sciences*
[3]*Engineering Development Co., Ltd.*
[4]*Advanced Reactor Technology Co., Ltd.*

In ref.[1,2], we have proposed a neutron moderator system for a cyclotron-based Boron Neutron Capture Therapy (BNCT). Nevertheless, a cyclotron with a beam power of 50 MeV and 300 μA is not realized yet. Therefore, to facilitate the realization of a cyclotron-based BNCT neutron filed, we started the design of the BNCT assembly employing a commercially available high-intensity cyclotron with a beam power of 30 MeVx750 μA. The design resulted in very promising feature and engineering design also indicated feasibility of the assembly. However, the validity of the design depends on the adequacy of the simulations by the MCNPX code[3] and LA150 data library[4] which were used in the design calculation and not validated yet.

In order to confirm the adequacy of neutron production and transport by MCNPX, we carried out two experiments; 1) measurement of neutron energy spectra from a tantalum thick target for 30 MeV protons with the TOF method, 2) measurement of the neutron energy spectrum for treatment using multi-moderator spectrometer[5] with the sand-II unfolding code[6].

The results for angle-dependent neutron energy spectra for the Ta(p,xn) reaction at 30 MeV (experiment 1) are shown in Fig.1. The present study is to evaluate the adequacy of the calculation of the neutron source. Then, Figure 2 shows the comparison between the calculation and the measurement of the Ta(p,xn) neutron spectra at 90-deg. The data for tungsten is shown for LA150 data because, in LA150 library, the neutron emission data is available only for tungsten and we confirmed the identity of tantalum data and tungsten data experimentally. The sum of the measured spectrum from 1 MeV to 5 MeV which

affects directly the required beam current or therapeutic time agree with calculation within 24%.

In Fig. 3, the results of neutron energy spectra for treatment (experiment 2.) are shown in count rate. The calculation result is obtained by folding the response function of multi-moderator spectrometer with neutron energy spectrum behind the moderator calculated by MCNPX. The result of the neuron energy spectra for treatment is shown in Fig.4. The measured data is in general agreement with the calculation except for the region above 40 keV, where the measurement is lower than the calculation. This is favorable feature because high energy neutrons cause damage to normal tissues. In conclusion, therefore, the feasibility of our proposal assembly is confirmed also from view point of neutronics.

References

1) Yonai S., et al., *Med. phys.* **30** (2003) 2021.
2) Yonai S., Itoga T., Baba M., Nakamura T., Yokobori H., Tahara Y., *Appl. Radiat. Isot.* **61** (2004) 997.
3) Pelowitz D.B., MCNPX Use's Manual, LA-CP-05-0369, April 13 (2005)
4) Chadwick M.B., et al., *Nucl. Sci. Eng.*, **131** (1999) 293.
5) Yonai S., et al. , *J. Nucl. Sci. Tech.*, **4** (Supplement) (2004) 415.
6) McElroy W.N., Berg, S., Crockett T., Hawkins, R.G., A study of the iterative method. AFWL-TR-67-41, Air Force Weapons Laboratory (1967).

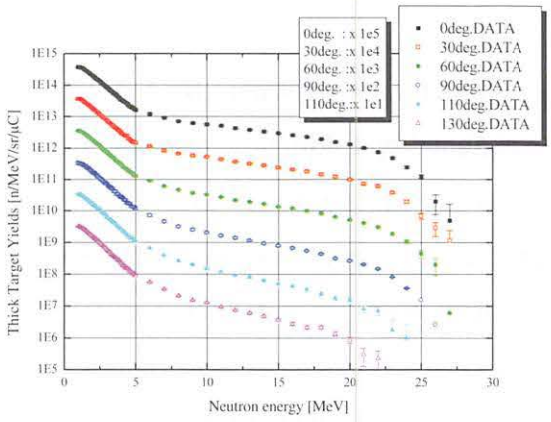

Figure 1. Neutron spectrum Ta(p,xn) [Ep=30 MeV]

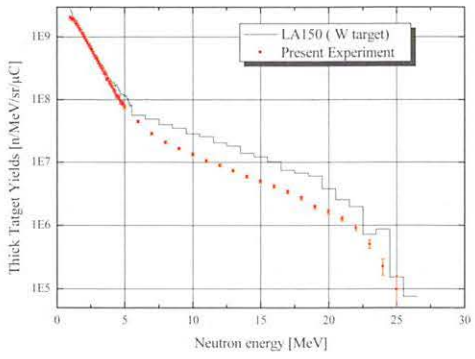

Figure 2. The measurement vs. The calculation [at 90 deg.].

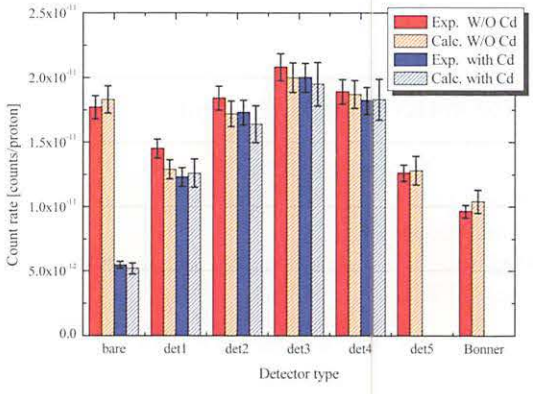

Figure 3. The count rate (The Experiment vs. The Calculation).

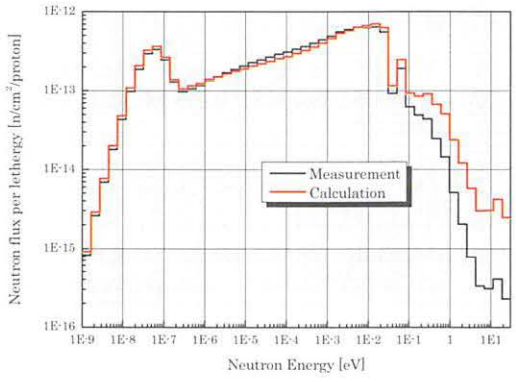

Figure 4. The neutron energy spectra for treatment.

IV. 3. Measurement and Monte Carlo Calculation of the Response Function of a Schottky CdTe Detector with a Guard Ring Electrode for Medical X-ray Field

Mohammadi A.[1], *Baba M.*[1], *Ohuchi H.*[2], *and Yamaguchi Y.*[1]

[1]*Cyclotron and Radioisotope Center, Tohoku University*
[2]*Graduate School of Pharmaceutical sciences, Tohoku University*

The CdTe detectors have a great advantage for use at room temperature because they are compact and have large photon absorption cross section in comparison with Si and Ge. Therefore, they are convenient for X-ray spectroscopic systems. However, the CdTe detectors have problems of poor charge transport properties because of the charge carrier trapping[1]. This problem has been improved significantly in a Schottky CdTe diode that is made of a high quality CdTe crystal, where a high Schottky barrier is formed by using indium[2,3] for the holes on a CdTe surface. The Schottky CdTe diode with guard ring can be operated with higher bias voltage, which leads to high resolution X-ray spectra free from tail structure, even at room temperature[4].

In this study, we use a Schottky CdTe detector with a guard ring electrode for analysis of medical X-ray field. The effective area of the detector is 4x4 mm^2 and 0.3 mm thick. The response function of the detector has been investigated at various operating condition for an ^{241}Am source. The spectra of mentioned source is shown in Fig. 2 at various bias voltage and shaping time. From this figure, the optimum applied bias voltage and shaping time are obtained to be 200 V and 2 μsec respectively.

The response function of detectors can be calculated using the MCNP4C code[5]. Our detector response was calculated by the code for ^{241}Am, ^{133}Ba and ^{152}Eu sources and then the results were compared with the measured responses at optimum operating condition. Figure 2 shows the experimental results in comparison with calculation for three sources. From these results, the energy resolution (FWHM) is estimated to be 1.53 keV, 1.6 keV and 2.07 keV for 59.54 keV, 81keV and 121.78 KeV, respectively.

The full-energy-peak efficiency of the detector has also been calculated and compared with the measurement for 60 keV and 81 keV lines of ^{241}Am and ^{133}Ba sources,

respectively. Figure 3 shows the calculated and measured full-energy-peak efficiency of the detector.

The general agreement between the calculation and the measurement confirms the validity of the calculation and that the carrier trapping effect is not serious for the present CdTe detector. The detector will be applied to the characterization of medical X-ray fields with the calculated response and peak efficiencies.

References

1) Richter M., Siffert P., Nucl. Instr. Meth. A322 (1992) 529.
2) Matsumoto C., Takahashi T., Takizawa K., Ohno R., Ozaki T., Mori K., IEEE Trans. Nucl. Sci. **45** (1998) 428.
3) Takahashi T., Watanabe Sh., IEEE Trans. Nucl. Sci. **48** (2001) 950.
4) Nakazawa K., Oonuki K., Tanaka T., et al., IEEE Trans. Nucl. Sci. in press (2004).
5) Gallardo S., Rodenas J., Verdu G., Med. Phys. **31** (2004) 2028.

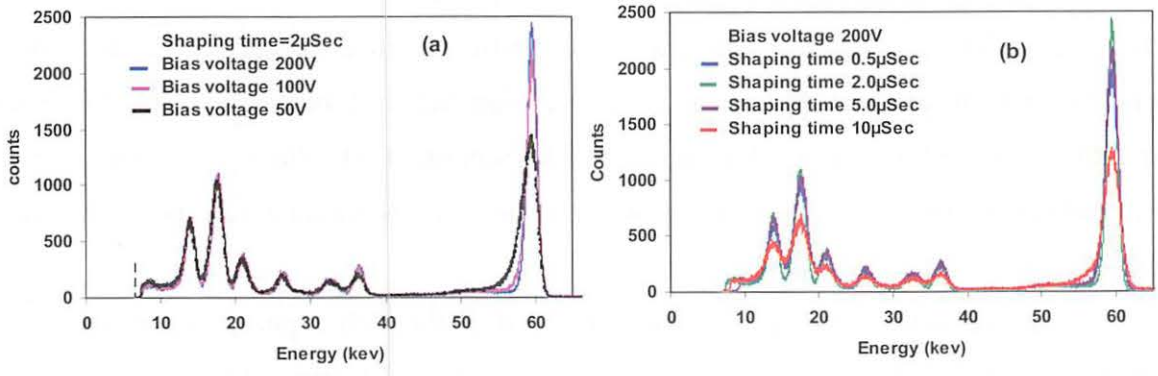

Figure 1. Spectra of ^{241}Am gamma-rays obtained with the Schottky CdTe detector with guard ring (a) at fixed shaping time of 2 μs and various bias voltage and (b) at fixed bias voltage of 200 V and various shaping time.

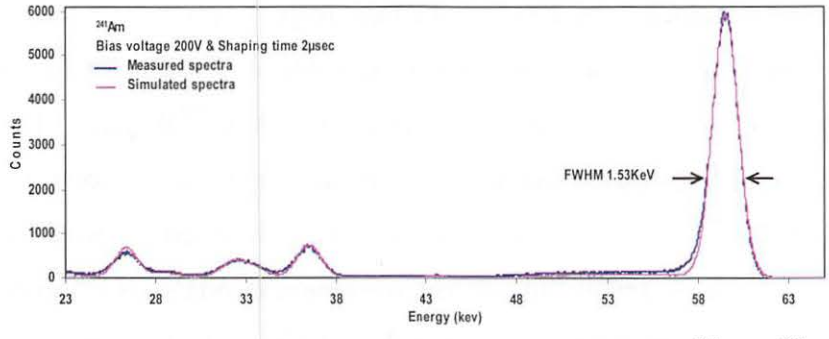

Figure 2. Comparison of the measured gamma-ray spectra for ^{241}Am, ^{152}Eu and ^{133}Ba with the calculated spectra.

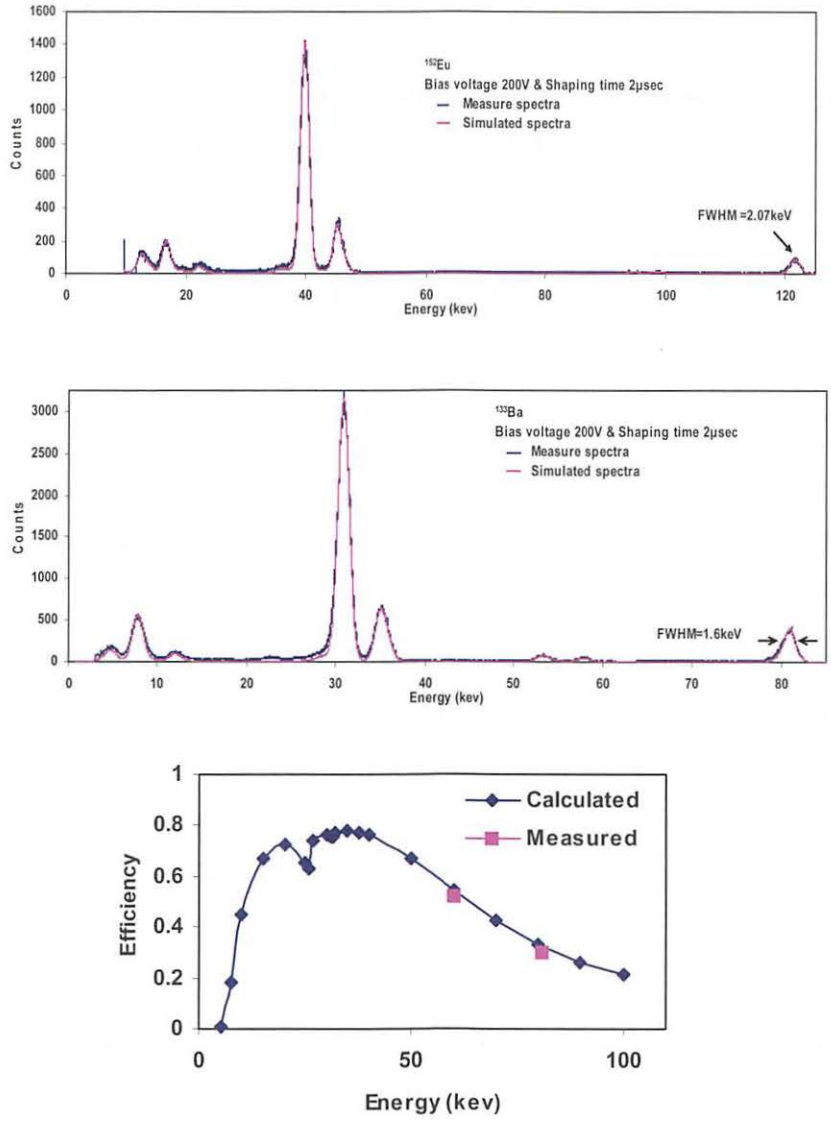

Figure 3. Comparison of calculated and measured full-energy peak efficiency of the Schottky CdTe detector with guard ring.

IV. 4. An Optical Common-mode Rejection for Improving the Sensitivity Limit of a Radiochromic Imaging Film

Ohuchi H.[1], *and Abe K.*[2]

[1]*Graduate School of Pharmaceutical Sciences, Tohoku University,*
[2]*Cyclotron and Radioisotope Center, Tohoku University*

Radiochromic plastic dye films, such as the commercially available GAFCHROMIC films (International Specialty Products, USA.), have been found to be excellent two-dimensional dosimetry tools for tissue-equivalence, having good spatial response, relatively flat energy response like LiF TLD' s (with a few exceptions, e.g. XR films1), wide dynamic range of absorbed doses, dose-rate independence and long-term storage of images, allowing multiple reevaluations, etc. Investigations up to 2002 are fully reviewed in the literature[1)]. They have, however, some drawbacks, such as low-sensitivity, non-uniformity of response, post-exposure optical density growth and film cost. Low-sensitivity and non-uniformity of response are difficult to resolve owing, mainly, to the low-Z composition of the films. The films were formerly imaging materials for high-dose radiation dosimetry and high-resolution radiography[2)]. However, their use has increasingly spread to medical and industrial applications, owing to their numerous excellent qualities. Nevertheless, their low sensitivities have become a serious obstacle, especially in medical applications. For example, doses from about 10 mGy to a few Gy are valuable for monitoring patient skin dose in interventional procedures, whereas the required doses (higher than those mentioned) for the present films preclude most applications.

Various studies have reported efforts to improve sensitivity: (1) layering five sheets of film together[3)]; (2) wrapping the film with UV phosphor screens[4)], or (3) GAFCHROMIC XR film including proprietary materials (Br, Cs, Ba)[5)]. It should be noted that the latter two improvements have been achieved with the loss of tissue-equivalence, owing to the high-Z material content. Further improvements in sensitivity seem to have reached their limit.

We considered the second drawback: macroscopic and microscopic non-uniformities of film layers, including the thickness variation of active radiochromic emulsions, discussed in Ref. 1 and inferred that these non-uniformities may be the main causes of light disturbance (noises) against the lights (signals) to be measured with a densitometer, resulting in a lowering of actual film sensitivities, i.e. generating the first drawback. The most important factor is not the intensity of signals but the optical S/N (signal-to-noise ratio) in the light paths.

Among the many devices used for film dosimetry, RGB color scanners have been extensively used by researchers[1,5,7]. Fortunately, the high absorption peaks upon irradiation are at 675 nm (main peak) and 617 nm (secondary peak), both lying in the red region of the light spectra (Fig. 2) and both responsible for the same R output from color scanners. It is noted that both R and G components are a set of raw data of the lights having passed together along the common optical path, hence, suffering a common fate upon attenuation, reflection, etc., with the exception of wavelength-dependent events. The R and G components are neighboring wavebands about 100 nm apart, nevertheless, their responses to radiation exposure are quite different. The R component is highly sensitive to radiation exposure, while the G component is nearly insensitive to radiation exposure, owing to the absence of a clear absorption peak in the green waveband. These facts indicate that the common-mode rejection (CMR) scheme may be successful in distinctively recording events not common to them, i.e. irradiated effects, if applied to paired optical signals.

The optical properties of radiochromic films1 were examined, using a spectrophotometer (DU-640, Beckman Coulter, Inc., USA.), and computer-simulated experiments carried out on the obtained absorption spectra to assess the applicability and validity of an optical version of the CMR scheme to radiochromic film dosimetry. The RGB components, needed for processing, were generated by multiplying the spectra by the RGB filter functions stated below. One way to simulate the CMR is to create a ratio of the two signals, where the factors common to both numerator and denominator will automatically disappear.

We found that, in the case of GAFCHROMIC films, the detection limit is greatly improved with the optical CMR stated above and the lowest detectable dose attained was nearly 20 mGy for the HS-14 (response range for product specification: 0.5 - 40 Gy) and 50 mGy for the MD-55-2 (response range: 2 - 100 Gy). Some studies, using a single color component (red in most cases) output from RGB scanners, have been reported[5,7], but, so far,

no publication has reported using the combination described above.

Experimental procedures were as follows: film specimens of 1 x 4 cm in size were placed on the sample stage in the X-ray irradiation system (MBR-1520R, Hitachi Medico Co., Japan.), exposed to X-ray beams of 100 kV with a 1.0-mm Al filter and monitored with a thimble ionization chamber (PTW-TN31003) installed inside the unit. They were analyzed, 24 or 25.5h after exposure, using the spectrophotometer over the range 450 - 1100 nm in 1.0-nm steps.

Figure 1 shows the RGB filter functions used for analysis, whose properties are similar to those of color filters for CCD photosystems. Figure 2 shows an example of the R and G components produced from an absorption spectrum for HS-14 film, multiplied by the filter functions. The vertical is expressed as light transmission in percentage, T (%).

The relationship between T and optical density (OD) used in film dosimetry can be expressed as follows:

$$OD = -\log_{10}(T/100) = 2 - \log_{10}T,$$

$$\text{net } OD = OD - OD_0 = \log_{10}T_0 - \log_{10}T = \log_{10}(T_0/T)$$

where subscripts denote unirradiated background quantities and 'net' stands for the quantities after removing the background.

In the case of the optical CMR scheme, T should be replaced by Rd/Gr, where Rd and Gr are the amounts of lights for the red and green components, respectively. Thus, reduced OD (ROD) in the optical CMR scheme, is:

$$ROD = 2 - \log_{10}(Rd/Gr), \quad \text{net } ROD = \log_{10}((Rd_0/Gr_0)/(Rd/Gr))$$

Figure 3 shows the dose-response curve, i.e. net ROD vs. absorbed dose, from 8.1 mGy to 1.6 Gy, for the HS-14 film 24 h after exposure. Figure 4 shows an expanded version of Fig. 3 over the range 0 - 500 mGy. The standard errors shown in the figures are less than 3.4% after repeated measurements.

Linear fits established for each of the two data sets have nearly the same slopes, demonstrating that HS-14 film is a valuable tool for monitoring doses down to about 20 mGy. Some fluctuations were observed around the lowest doses, which were, however, far lower than the normal working range of the X-ray system of 0.1- 860 Gy.

Figure 5 shows the dose-response, from 7.2 to 720 mGy, for the MD-55-2 film, 25.5 h after exposure. The lowest detectable dose was about 50 mGy. The cause of fluctuations around the doses lower than 40 mGy are unclear. However, MD-55-2 film

may contain some additional causes, owing to multilayer interference and its polarization properties[1].

References

1) Butson M. J., Yu P. K.N., Cheung T., Metcalfe P., Mat. Sci. Eng. R**41** (2003) 61.
2) McLaughlin W. L., Yun-Dong C., Soares C.G., Nucl. Instr. and Meth. A**302** (1991) 165.
3) Cheung T., Butson M. J., Yu P. K.N., Phys. Med. Biol. **46** (2001) N235.
4) Geso M., Ackerly T., Patterson W., Med. Phys. **31** (2004) 1014.
5) Devic S., Seuntjens J., Hegyi G., Podgorsak E.B., Soares C.G., Kirov A.S., Ali I., Williamson J.F., Elizondo A., Med. Phys. **31** (2004) 2392.
6) Dini S.A., Koona R.A., Ashburn J.R., Meigooni A.S., J. Appl. Clin. Med. Phys. **6** (2005) 1.
7) Aydarous A. ., Darley P.J., Charles M.W., Phys. Med. Biol. **46** (2001) 1379.

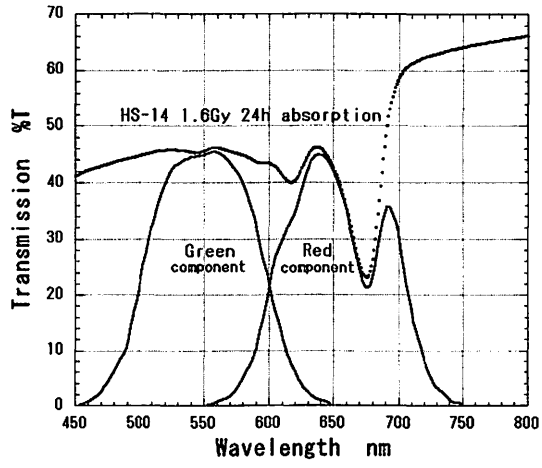

Figure 1. Filter functions for red and green wavebands used for analysis.

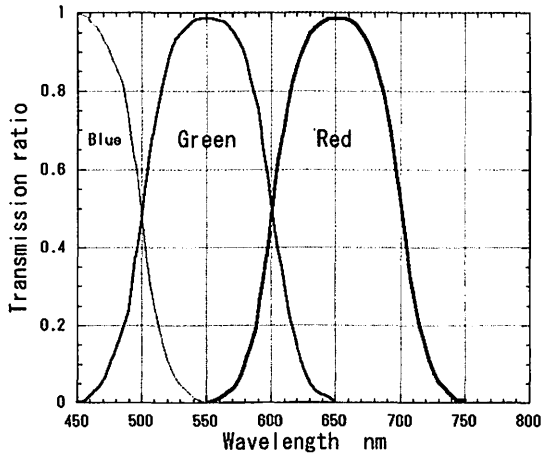

Figure 2. An example of HS-14 absorption spectrum and its color components formed with the filter functions shown in Fig. 1.

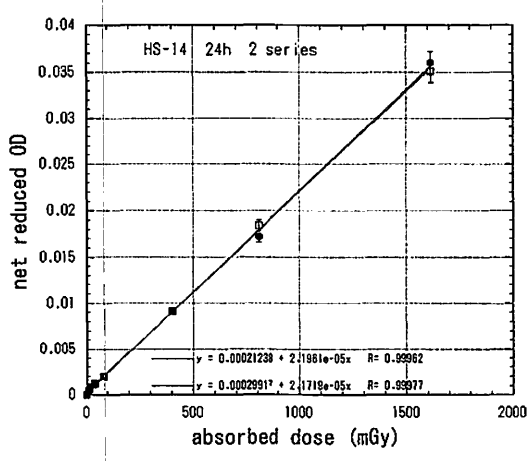

Figure 3. Net reduced optical density vs. absorbed dose for HS-14 when exposed to 100 kVp x-rays.

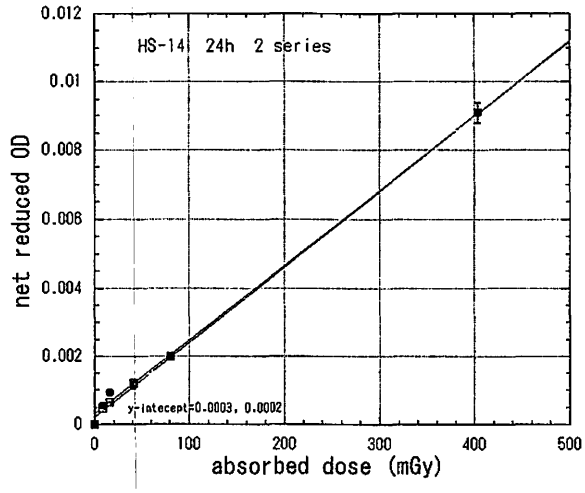

Figure 4. An expanded version of Fig. 3, net reduced OD vs. absorbed dose for HS-14.

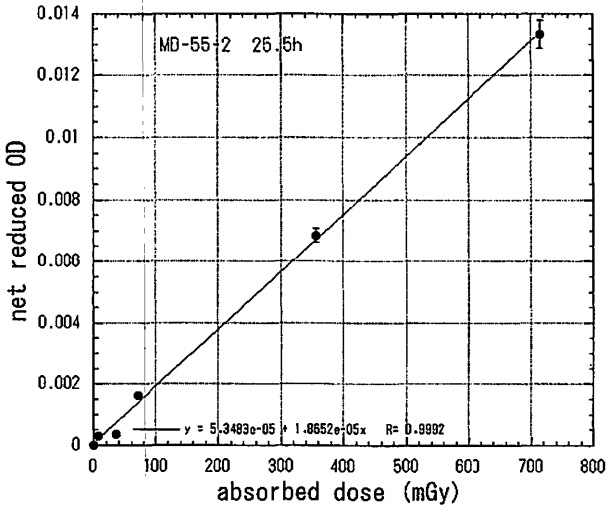

Figure 5. Net reduced optical density vs. absorbed dose for MD-55-2 when exposed to 100 kVp x-rays.

IV. 5. Preliminary Report of Position Sensitive CdTe Detector for a Semiconductor PET Camera

Kikuchi Y.[1], Ishii K.[1,2], Yamazaki H.[1], Matsuyama S.[1], and Kudo T.[1]

[1]*Graduate School of Engineering, Tohoku University*
[2]*Cyclotron and Radioisotope Center, Tohoku University*

Application of small semiconductor detectors to PET camera is an effective way to achieve high spatial resolution because it can make possible that data are obtained in fine spatial sampling width. But, the use of small detector may cause decreasing of system sensitivity. When detectors are aligned, vacancy between them is needed in order to divide detectors electrically, and this causes that packing ratio becomes lower.

In order to avoid decreasing of packing ratio, we propose to embed a position sensitive detector to a semiconductor PET camera. We report about development of a position sensitive CdTe detector for a semiconductor PET camera. From our previous research, it was determined that CdTe (cadmium telluride) semiconductor detector, whose atomic number was high (Cd: 42, Te 52), was suitable for application of PET. In particular, schottky CdTe detector which is made by evaporating In an Pt as electrode can be available in high bias voltage, so that fast timing performance is expected.

A position sensitive semiconductor detector is made by formation of resistive area electrode. Several output lines are connected to the surface and detection position is determined by calculating fraction between output amplitude of signals. In order to form the resistive electrode, thickness of evaporation metal on the crystal is controlled. This may make it possible that resistive electrode is formed, preserving good timing performance. With ion beam induced charge (IBIC) method, we confirmed formation of resistive electrode by controlling electrode thickness. IBIC is a technology which is for research about charge collection ability of radiation detector by irradiating ion beam to the detector. A CdTe detector whose electrode thickness was controlled was irradiated 3 MeV proton with micro beam line in Fast Neutron Laboratory, Tohoku University and a correlation between irradiation position on the electrode and signal outputs.

Thickness of In evaporated electrode was controlled and, two Au wire which transfers signal were attached on the electrode. 3 MeV proton beam which was focused with the micro beam line was irradiated on each position on the electrode. Signals from In electrode were measured simultaneously together with a signal of Pt electrode, using multi-parameter ADC. Schematic of the experiment is indicated in Fig. 1.

Figure 2 shows the results of irradiation at 0.5 mm pitch. This plot indicates correlation between one of signals from In electrode and the signal from Pt electrode. It was confirmed that irradiation in each position could be identified clearly. Fig.3 shows histogram of ratio of In signal amplitude to Pt signal amplitude in 1 mm pitch irradiation. Position resolution can be calculated from distance between irradiation positions and width of distribution and the resolution on a center of the detector is less than 0.3 mm. This resolution is for 3 MeV proton and it is assumed that resolution is decreased by reducing energy deposition. But, it is supposed that the detector has enough resolution to 511 keV and can be applied to PET camera.

We will optimize control parameters of the detector and discuss way to apply to PET camera.

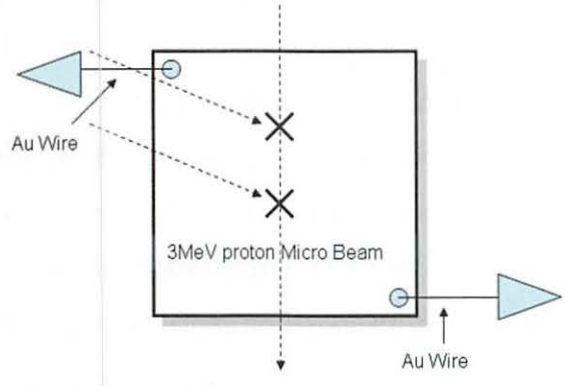

Figure 1. Schematic image of irradiation in IBIC experiment.

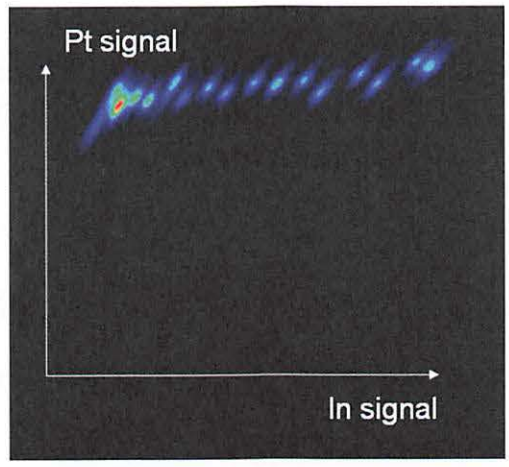

Figure 2. Correlation between Pt signal output and In signal output in each irradiation position

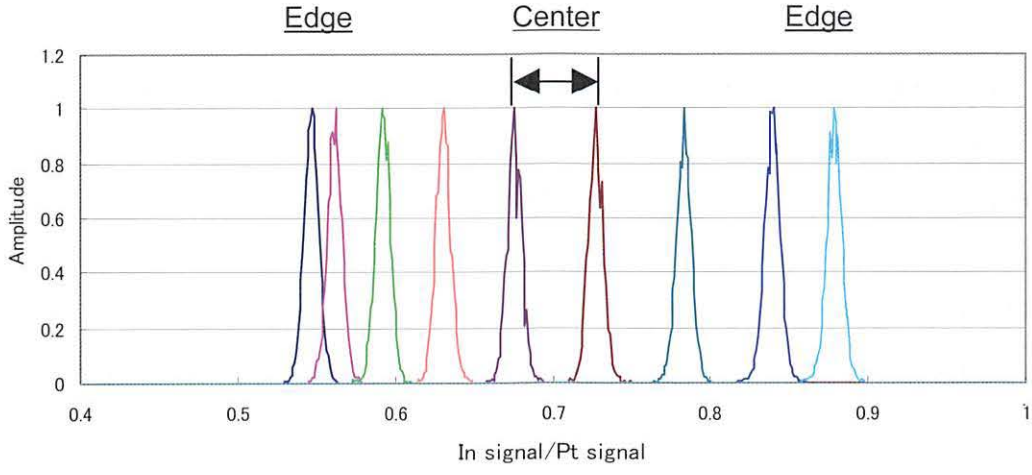

Figure 3. Ratio (In signal)/(Pt signal) in each position of 1mm pitch irradiation.

IV. 6. Development of a Pulse Height Estimation Method for a High Resolution PET Camera with Position Sensitive Semiconductor Detectors

Sakai T., Ishii K., Yamazaki H., Matsuyama S., and Kikuchi Y.

Graduate School of Engineering, Tohoku University

Introduction

In order to achieve high spatial resolution, application of semiconductor detectors to animal PET cameras is an effective way. Semiconductor detectors can be small, and these detectors enable fine spatial sampling. But, use of small semiconductor detectors may cause decrease of system sensitivity, because of vacancy between detectors aligned densely.

Against this problem, we propose use of position sensitive semiconductor detectors (PSD), which are consisted of continues crystal. Generally, one of electrode of these detectors is a resistive layer on which several wire are connected to obtain signal. Because there is a correlation between an energy deposited position in the detector and outputs fraction from detector, the position can be identified with calculation. But, devices which can acquire pulse height information, like ADCs, are necessary for position analysis, so that a measurement system become large, when considering of detectors number in a PET camera. So, it is desirable that pulse height information is acquired with a simple way. We report about pulse height estimation method based on pulse shape analysis without ADCs.

Principle

Pulse height of an analog signal from a radiation measurement circuit which is consisted of preamplifiers, amplifiers, and so on, is proportional to energy deposited to a detector, and a pulse shape depends on time constant of the circuit. In order to estimate pulse height, we propose amplitude to time conversion (ATC) method with a comparator. When an analog signal is input to comparator, a width of a comparator signal is determined

uniquely by analog pulse height. Figure1 shows an example of ATC method.

Assumed that an analog signal rises quickly, and fall exponentially, the signal, which arise at t = 0, is expressed in next equation.

$$V = Vo\exp\left(-\frac{t}{\tau}\right) \qquad \text{(Equation 1)}$$

So, correlation between output signal amplitude and comparator output width Δt is indicated by a following equation, when reference voltage of comparator is Vref.

$$Vo = Vref\exp\left(\frac{\Delta t}{\tau}\right) \qquad \text{(Equation 2)}$$

Experiments and analysis

The estimation method was evaluated with a CdTe detector which was a candidate of detectors for a semiconductor PET camera. The CdTe detector was coupled to a linear amplifier via a charge sensitive preamplifier, and amplifier outputs signals were observed and stored with a digital oscilloscope as digital pulse shape data. In order to assume comparator outputs, periods when signal was over reference voltage which was set at several conditions was calculated from the pulse shape data.

A typical pulse shape is shown in Fig 2. Although it is assumed that a pulse rise time can be neglected in equation (1) and (2), rise time is considerable in actual signal, so that Δt' is smaller than Δtc, when Δt' is a period of a actual signal and Δtc is a period calculated from the signal amplitude with equation (2).

Figure 3 shows that fraction of Δt' to Δtc. Because the fraction is unique in a constant reference voltage, accurate signal amplitude can be calculated by acquiring fraction f experimentally. A following equation is derived from equation 1 or 2 with f.

$$Vo = Vref\exp\left(\frac{f\Delta t'}{\tau}\right) \qquad \text{Equation (3)}$$

Applying the equation (3), signal amplitudes Vp(calc) were calculated according to acquired digital signal data. Figure 4 shows correlation between Vp(calc) to actual signal amplitude Vp(measurement). The correlation indicates good linearity.

Conclusion

The simple Method to estimate pulse amplitude without an ADC module is proposed for PET camera which is consisted of a large number of detector elements. In

experiments with CdTe detector, it was confirmed that a calculated signal amplitude is determined uniquely by Δt,which is a period when signal is over reference voltage. And accurate amplitude can be informed by using a correction fraction f which is obtained experimentally.

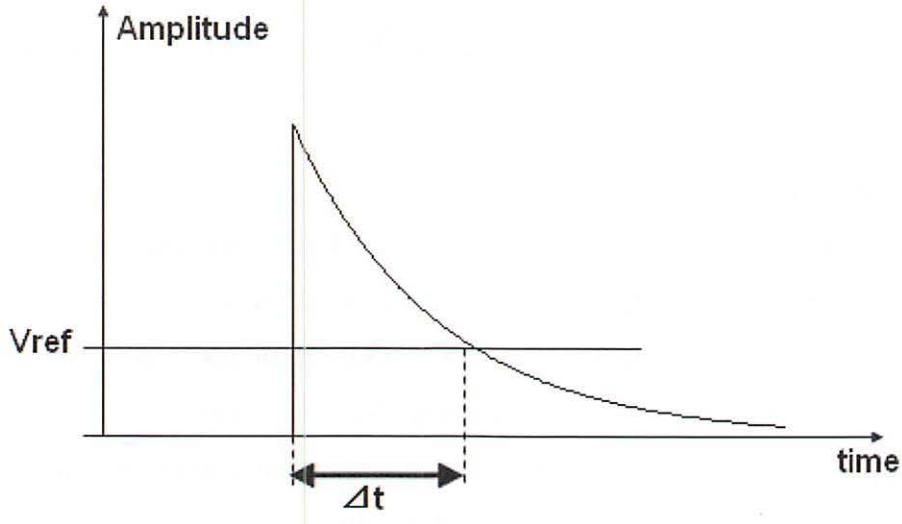

Figure 1. Principle of ATC method.

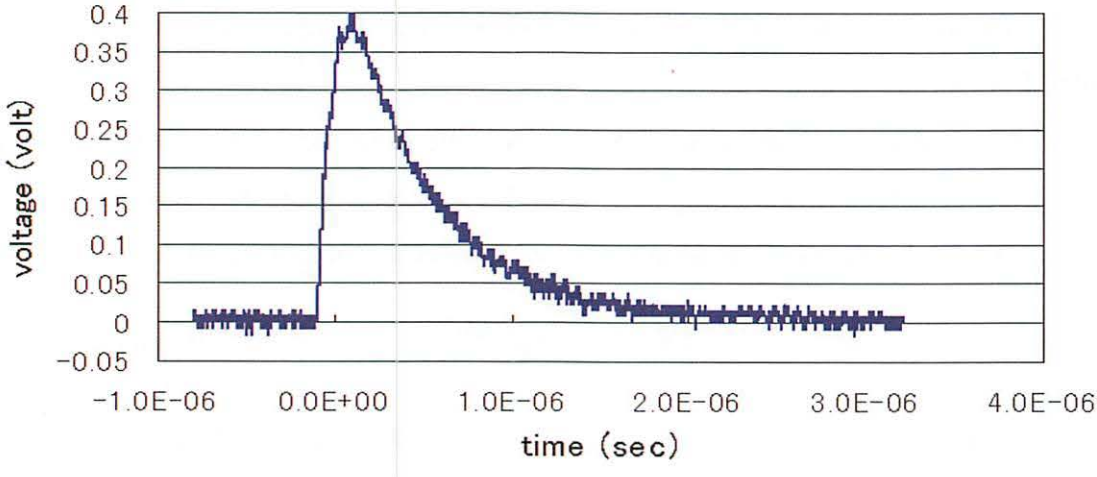

Figure 2. Actual signal shape from CdTe detector.

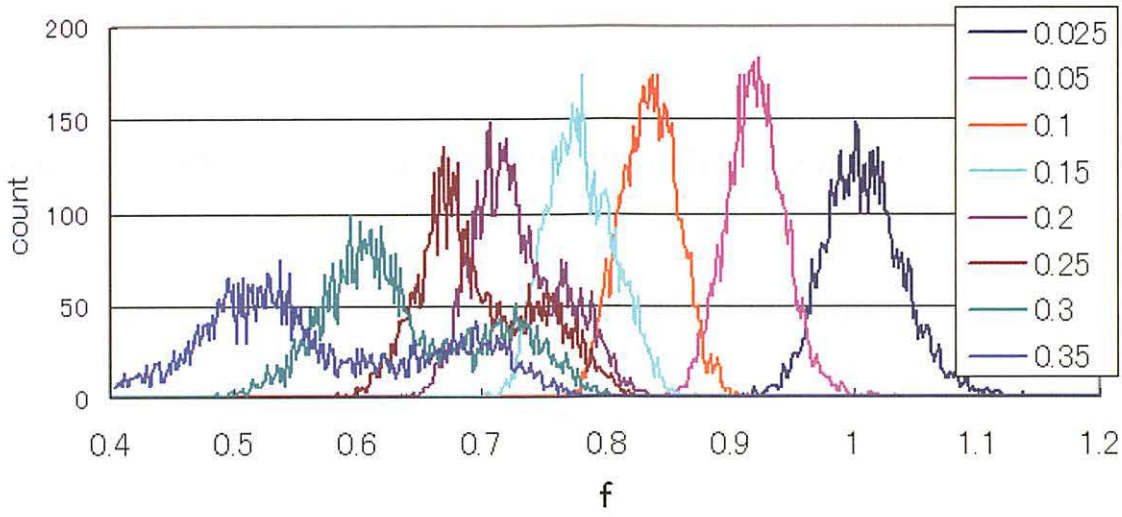

Figure 3. fraction of Δt' to Δtc in various reference voltage.

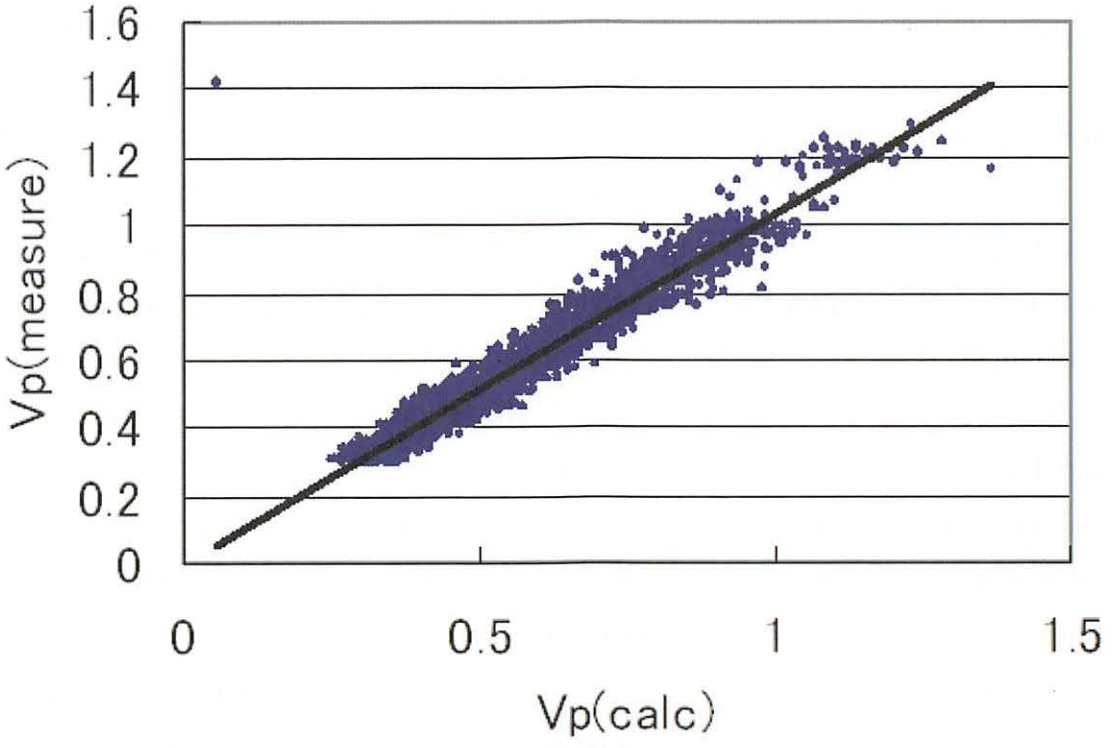

Figure 4. correlation between measured signal output voltage and calculated signal output voltage with ATC method.

IV. 7. Accuracy of Registration Algorithm Based on Mutual Information

Kumagai K., Sasaki T., Yamaguchi K., Margaretha S., Miyake M., Watanuki S., Tashiro M., and Itoh M.

Cyclotron and Radioisotope Center, Tohoku University

In medical imaging studies, it is now commonly performed to scan the same subject with different imaging devices in order to obtain the complementary information by fusing these images into one. This technique, multimodality image fusion, is one of the current subjects in many fields of 3D medical image processing. The key issue of the image fusion is assessment of registration accuracy. In this report we will summarize the results of the investigation on performance of registration algorithm. The first step of the registration process yields a rough estimates of rigid transformation parameters with images of much decreased resolution, for which Nelder-Mead Simplex method was used to find a global maximum of mutual information (MI). With increased resolution, the third and the following steps include optimization for 12 affine transformation parameters, where Davidon-Fletcher-Powell method is used for maximizing the cost function. The one dimensional maximization is solved using a line search procedure such as golden section method that does not require any derivatives. Throughout the entire process, only used matching criterion is MI. Thus, the method does not directly depend on image intensity itself and is generally applicable to inter-modality image registration with global transformation. The validation study was performed with simulated PET-MR head images. The present method has some operation parameters which include initial image resolution to begin multiresolution process, interpolation method for image transformation, histograming method to evaluate mutual information and convergence condition to stop iteration of optimization process. The latter two would not greatly affect the performance. We applied the present method with different initial image resolutions (low, medium and high) and two types of interpolation (nearest neighbor and linear) to a series of randomly mismatched simulation images and measured computation time and matching error after the registration.

In order to examine the performance of the present method, PET-MR head images were simulated to mimic finite resolution images. The simulated images can be transformed without need of interpolation which might cause serious side effects on the results of the validation study. Considering that MI does not strongly depend on shape of a overlapping image but on the intensity distribution of images, simulation images were carefully adjusted to reproduce the real intensity distribution by optimization of parameterized distribution functions of asymmetric ellipsoid shape each of which approximates both spatial and intensity distribution of PET and MR image parts. PET image was randomly transformed to be a series of test images, while MR image was held fixed as a reference image. The three kinds of the test image series were used to examine the performance and accuracy as a function of initial mismatch. The rigid body transformation were used to generate the test images. The algorithm was implemented as a computer program and was written mainly in fortran and partly in assembler source code to manually optimize execution speed, especially for FPU operation. The calculation for the validation study was performed using a PC (600 MHz-CPU, 250MB-RAM). Table 1 shows the measured CPU time and mean matching error of the registration with different operation parameters.

An average CPU time needed to register each images was 52 sec when the process has been given the highest scheduling priority. This value increases to 780 sec if the hierarchical optimization scheme was dismissed. Variance of the computation time was due mainly to the differences of number of pixels in an image. Table 1 shows that the computation time increases as initial resolution increases and that mean matching error decreases as initial resolution increases. As the validation study reveals, the performance and accuracy of the present method strongly depends on operation parameter and initial condition of mismatching images. Assuming that the resolution of PET images is larger than 3 mm, and that of MRI and CT is negligible to PET, the accuracy of registration less than 3 mm would be of no real significance. Thus, if the accuracy is sucient, that is, less than 3 mm, then the best operational parameter would be the one that gives the smallest computation time. Table 1 indicates that by using the optimum operational parameters, the present method can match PET-MR head images with an overall error of less than 3 mm in 60 seconds. Considering that in most cases PET images have the worst resolution among other 3D medical image modalities, and that the resolution is the most dominant source that afects both performance and accuracy, the results of the validation study of the present method might essentially be unchanged even if it were applied to other cases than PET-MR head images. The more detailed description about the results of the validation study will

not be reported before PET-CT image set, which consists of 12 pairs of whole or partial PET and CT image scanned with GE discovery ST, is processed by the present method. It will give some measure of accuracy of the present method in the case of real images, since the registration must give no global transformation for these images. In several cases affine matrix given by the present method was nearly diagonal and CPU time was around 690 sec for whole body images. The deviation from diagonal was at most 4 mm in the z-direction.

Table 1. The CPU time (sec) and mean matching error of the registration in the case of initial mismatch of ±10 mm and ±10°.

Initial resolution	Interpolation	CPU time	Translation	Rotation
1/16	nearest neighborer	12	4.5	10.3
1/16	linear	15	0.5	2.5
1/8	nearest neighborer	24	0.5	3.0
1/8	linear	30	0.2	0.8
1/4	nearest neighborer	80	1.5	2.2
1/4	linear	91	0.6	0.9
1	nearest neighborer	212	0.5	0.3

V. PIXE AND ENVIRONMENTAL ANALYSIS

V. 1. Micro-beam Analysis System at Tohoku University

Matsuyama S.[1], Ishii K.[1], Yamazaki H.[1], Barbotteau Y.[1], Amartaivan Ts.[1], Izukawa D.[1], Hotta K.[1], Mizuma K.[1], Abe S.[1], Ohishi Y.[1], Rodriguez M.[1], Suzuki A.[1], Sakamoto R.[1], Fujisawa M.[1], Kamiya T.[2], Oikawa M.[2], Arakawa K.[2], Imaseki H.[3], and Matsumoto N.[4]

[1]*Graduate School of Engineering, Tohoku University*
[2]*Takasaki Radiation Chemistry Research Establishment, Japan Atomic Energy Research Institute*
[3]*National Institute of Radiological Science*
[4]*TOKIN Machinery Corporation*

Introduction

The nuclear microbeam has proved to be a powerful analytical tool by combining various analysis techniques such as PIXE, RBS, NRA, CT and STIM[1,2]. A microbeam system was constructed at the Tohoku University Dynamitron Laboratory for biological applications. The microbeam line was installed in July 2002 and has since been optimized to obtain a beam spot size smaller than 1 μm. In microbeam analysis of biological specimens, simultaneous measurement of structural and elemental properties is very important[3,4] and can be obtained by combining PIXE, RBS and STIM analysis. This paper describes performance of the microbeam system and presents typical results of biological applications.

Microbeam Analysis System

The microbeam system is installed at the 4.5 MV Dynamitron accelerator at Tohoku University. Technical details of this system have been given in a previous paper[5]. The system was designed for a spatial resolution less than 1 $\times$1 μm^2 using the second order calculation code "TRANSPORT" [6]. This beam spot size is obtained with object-to-lens distance of 6 m and working distance of 30 cm when the energy resolution of the beam is $\Delta E/E = 1.3 \times 10^{-4}$ and beam divergence is limited to 0.2 mrad with object size set to 30×8 μm^2. The microbeam line consists of a doublet quadrupole lens and a system of microslits, divergence-defining slits mounted on a heavy rigid support to isolate from vibrations. Three turbo-molecular pumps evacuate the beam line and target chamber.

The quadrupole lens core is cut from a single iron piece. The bore radius is 5 mm and is machined with a tolerance less than 2 μm using a numerically controlled machine to reduce sextupole field contamination[7,8]. The focused microbeam is scanned across the sample by using electrostatic deflection plates and HV amplifiers. Offset voltages are applied to deflection plates in order to position the microbeam on a selected sample region. The scanner is located downstream of the quadrupole doublet and the maximum scanning area is larger than 1×1 mm^2. The schematic diagram of the target chamber is shown in Fig. 1. The target chamber is a rectangular box and applicable to either in-vacuum or in-air PIXE combined with RBS and STIM experiments. In the analysis under vacuum, samples are set 25 mm downstream of the chamber center and working distance is 259 mm. Horizontal and vertical demagnification factors are 1/35.1 and 1/9.2, respectively. A sample holder can sustain a CaF_2 beam viewer and a total of 8 samples. Normally, we use a Si(Li) detector (Sensitive area of 80mm^2, effective thickness of 4000 μm and Be window thickness of 12 μm) for PIXE measurement and the detector is set at 115 degrees with respect to the beam axis. Since recoil protons deform the PIXE spectra, a Mylar filter is attached to the front of the detector. The minimum distance from sample to the detector is less than 10 mm, restricted by the size of the sample holder. An ion-implanted silicon detector (sensitive area: 100 mm^2, depletion depth of 100 μm) is attached at a distance of 60 mm for RBS measurements at an angle of 140 degree. To get structural and density information, scanning transmission ion microscopy (STIM) is used. Since transmitted ions are directly detected, a very low current is sufficient for structural mapping. Therefore, the beam current has to be reduced. The silicon detector is attached to a wheel off center from the beam axis and a Faraday cup is also attached to this wheel. The wheel is turned slowly until the detector is centered on the beam axis while monitoring the count rate of the detector and adjusting beam current accordingly. Using off-axis and on/off-axis geometry, one can perform simultaneous structural imaging in PIXE analysis[9]. Off-axis geometry is obtained by rotating the wheel and respective scattering angle is determined from the counting rate of the particle detector. In on/off-axis geometry, a thin scattering foil with a collimator is set 10 mm downstream of the sample.

In in-air analysis, proton beams are extracted through a Mylar film (4 μm), which serves as backing film of the sample. Beam broadening through the film is estimated to be less than 0.01 μm and does not degrade beam quality significantly. Three samples are attached on a circular sample holder and can be changed without breaking the vacuum.

Sample position is 65 mm downstream compared to the in-vacuum sample position. Demagnification factors are 1/28.5 (horizontal) and 1/8.2 (vertical), respectively. To reduce sample damage through beam and energy loss in STIM measurement, He gas is blown on the sample. X-ray detector and RBS detectors are set in vacuum at 125 and 140 (or 162.7) degree with respect to the beam spot on the sample, respectively. STIM measurement can be performed in vacuum and in air as well. To minimize the energy loss in gas, the sample to detector distance is kept below 5 mm. Total energy loss in He gas is ~10 keV and the short distance and finite detector size make it impossible to carry out off-axis and on/off-axis STIM measurements.

The data are acquired by a multi-parameter data acquisition system which accepts 4 ADC inputs of energy pulse signals in addition to two position signals and allows to combine 4 ion-beam analysis techniques in a simultaneous measurement[5,10]. The system can be extended more than 10 ADC inputs, which is sufficient for additional ion beam applications. The beam is continuously scanning across the sample and data is taken whenever one of the ADCs detects a pulse signal. The data is acquired event-by-event (list mode) and elemental maps and energy spectra of selected regions can be generated on-line, while the system is acquiring data.

Results

The beam spot size is measured by beam scanning across mesh samples (Ni, Cu and Au mesh, 1000 or 2000 lines/inch), and measuring X-rays. Figure 2 shows the typical line profile of a 2000 Ni mesh, measured in vacuum fitted by symmetric double Gaussian convolution. The line profile is well reproduced by the symmetric double Gaussian convolution. This implies that the beam profile can be assumed to be of Gaussian shape. Beam spot sizes of less than 0.9 $\times$0.9 μm^2 are obtained at a microslit gap of 50 $\times$15 μm^2 in vacuum with a beam current of ~40 pA. These results are slightly better than those expected from the calculations. However, when we measured beam spot size with 1000 Cu mesh, the spot size rapidly converged and then saturated at 2 μm[5], which hinted at a possible system problem. Off-axis STIM analysis provided the solution, as shown in the spectrum on the Cu 1000 mesh in Fig. 3. Two peaks appear in the STIM spectrum, which implies the existence of two different mesh thicknesses. Figure 3 also shows the visual images corresponding to these two peaks. It is obvious that the mesh edges exhibit a step, which is observed in the SEM image. The edges of Ni and Au 2000 mesh are very sharp,

however, and these mesh are ideal for the measurement of the beam spot size[11].

The intensity of the beam halo is ~1/500 fraction of the central part, strongly depending on vacuum pressure. The stability of beam position on target sample is maintained during several hours of measurements. However, if we heat the rigid support of the beam line by heat gun for a few minutes, the beam spot moves by about 6 μm. It takes 30 minute for the beam spot to return to the original position after heating is stopped. If we blow cool air on the rigid support by air conditioner, the beam moves gradually and takes a long time to return to its original position after cooling is stopped. As well as temperature control, local heating/cooling, such as lightning by a light bulb and air blowing by air conditioners, on the system should be take care during measurements.

First, we applied the system to the study of radiation damage of polymer foils, whose behavior under beam irradiation is comparable to that of practical biological samples[12]. Measurements are made in-vacuum and in-air for various beam conditions. Typical results of samples irradiated in-vacuum are shown. Before and after irradiation we accumulated on/off-axis STIM data. Irradiation was carried out with 3 MeV proton beam, beam currents of ~400 pA, beam spot size of 3.7 $\times$3.7 μm^2 and scanning area of 300$\times$300 μm^2. Total accumulated charge was 2.9 μC and RBS and off axis STIM data were measured. Figure 4 shows RBS and off-axis STIM spectra at three specific times (0-0.3 μC, 1.3-1.6 μC and 2.4-2.7 μC) of the entire data set divided into eleven parts. Changes in RBS spectra are clearly seen, which correspond to elemental loss of oxygen. About 40 % of oxygen elements are lost during the irradiation. Density changes are also seen in the off-axis spectra. Peak energy is increased ~10keV at the end of irradiation, which is consistent with RBS data. Low energy peak (~500channel) in the off-axis STIM spectra is formed by protons which are scattered from hydrogen and can be used to monitor elemental loss of hydrogen.

Next, the microbeam system was used for the elemental analysis of bovine aortic endothelial (BAE) cells, which were cultured in a bromodeoxyuridin(BrdU) containing medium[13]. Figure 5 shows typical elemental maps and the optical image of BAE cells obtained in the vacuum condition. These images were obtained before the STIM system was in operation. Data accumulation took two hours to obtain these images with beam currents of ~60 pA, beam spot size of 1.5$\times$1.5 μm^2 and scanning area of 50$\times$50 μm^2. Distributions of P, S, Cl and K elements are clearly seen and correspond to the shapes of BAE cells. Trace Br elements, which are absorbed into their nuclei during DNA synthesis,

are also seen in the image.

These results demonstrate that the present microbeam analytical system is applicable to biological studies.

Acknowledgements

This study was supported by a Grant-in-Aid for Scientific Research (S) No. 13852017 (K. Ishii), from the ministry of Education, Science and Sport and Culture. The authors express their thanks to Dr. M. Fujiwara for his help to take SEM images of mesh samples. The authors would like to appreciate their thanks to Mrs. T. Takahashi, K.Komatsu, T.Nagaya and C.Akama for their help in constructing the microbeam and target system.

References

1) Watt F., Grime G.W., Principal and Applications of High energy Ion Microbeams, Adam Hilger, Bristol (1987).
2) Johansson S.A.E., Campbell J.L., Malmqvist K.G., Particle-Induced X-ray Emission Spectrometry (PIXE), John Willey and Sons (1995).
3) Sjoland K.A., Kristiansson P., *Nucl. Instr. Meth.* **B118** (1996) 451.
4) Deves G., Ortega R., *Nucl. Instr. Meth.* **B181** (2001) 460.
5) Matsuyama S., Ishii K., Yamazaki H., Sakamoto R., Fujisawa M., Amartaivan Ts., Ohishi Y., Rodoriguez M., Suzuki A., Kamiya T., Oikawa M., Arakawa K., Matsumoto N., *Nucl. Instr. Meth.* **B210** (2003) 59.
6) Brown K.L., SLAC-91 (1977).
7) Grime G.W., Dawson M., Marsh M., McArthur I.C., Watt F., *Nucl. Instr. Meth.* **B54** (1991) 52.
8) Jamieson D.N., F.Legge G.J., *Nucl. Instr. Meth.* **B29** (1987) 544.
9) Pallon J., Elfman M., Kristiansson P., Malmqvist K., Graneli, E. Sellborn A., Karlsson C., *Nucl. Instr. Meth.* **B158** (1999) 312.
10) Matsuyama S., Ishii K., Sugimoto A., Satoh T., Gotoh K., Yamazaki H., Iwasaki S., Murozono K., Inoue J., Hamano T., Yokota S., Sakai T., Kamiya T., Tanaka R., *Int. J. PIXE* **8** (1998) 203.
11) Watt F., *Nucl. Instr. Meth.* **B104** (1995) 647.
12) Themner K., *Nucl. Instr. Meth.* **B54** (1991) 115.
13) Ishii K,, Sugimoto A., Tanaka A., Satoh T., Matsuyama S., Yamazaki, H. Akama C., Amartaivan Ts., Endoh H., Oishi, Y. Yuki H., Sugihara S., Matoh M., Kamiya T., Sakai T., Arakawa K., Saidoh M., Oikawa S., *Nucl. Instr. Meth.* **B181** (2001) 448.

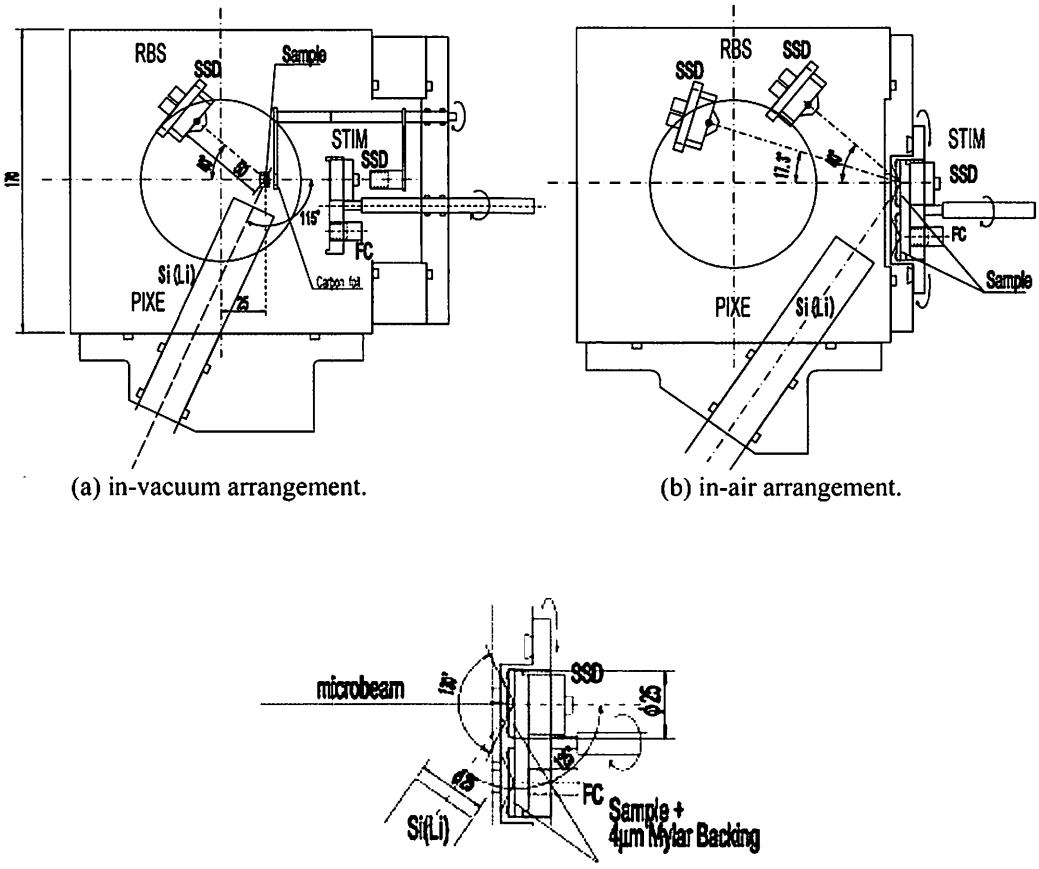

(a) in-vacuum arrangement.

(b) in-air arrangement.

(c) close-up of in-air arrangement.

Figure 1. Schematic diagram of the Target Chamber.

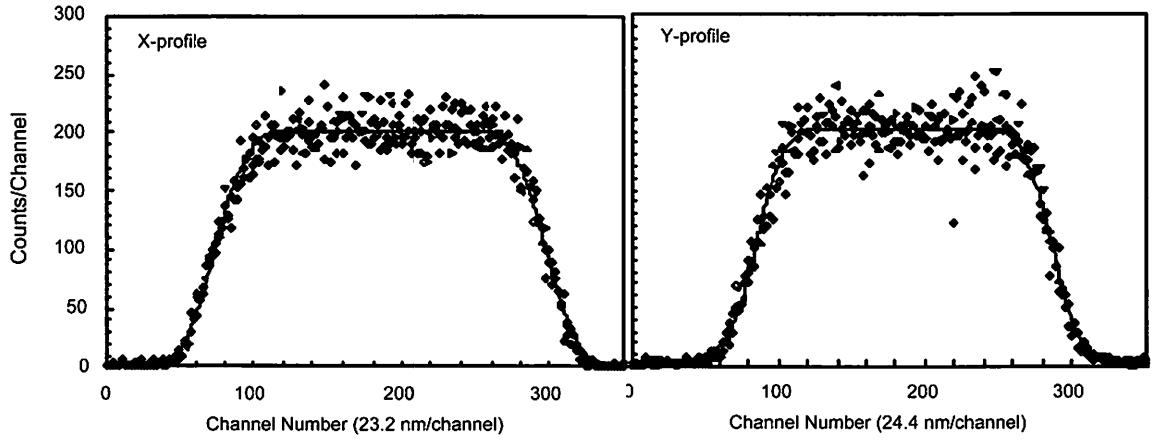

Figure 2. X-ray line profile of the Ni Mesh (2000 lines /inch).

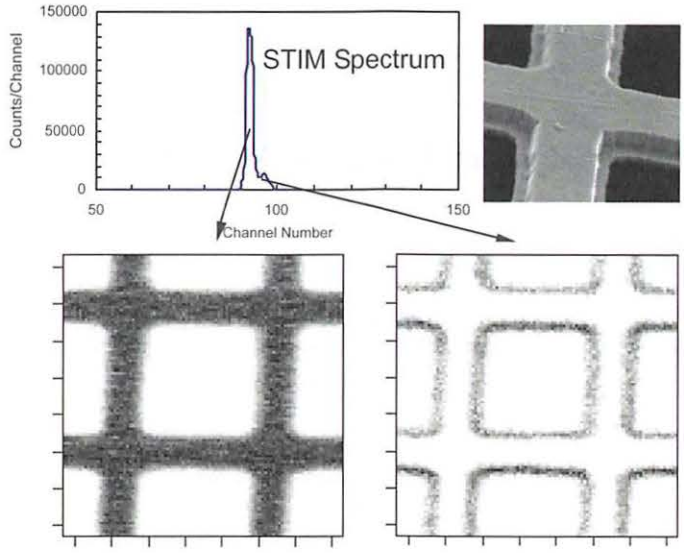

Figure 3. STIM spectrum and images of the Cu mesh (1000 lines/inch).

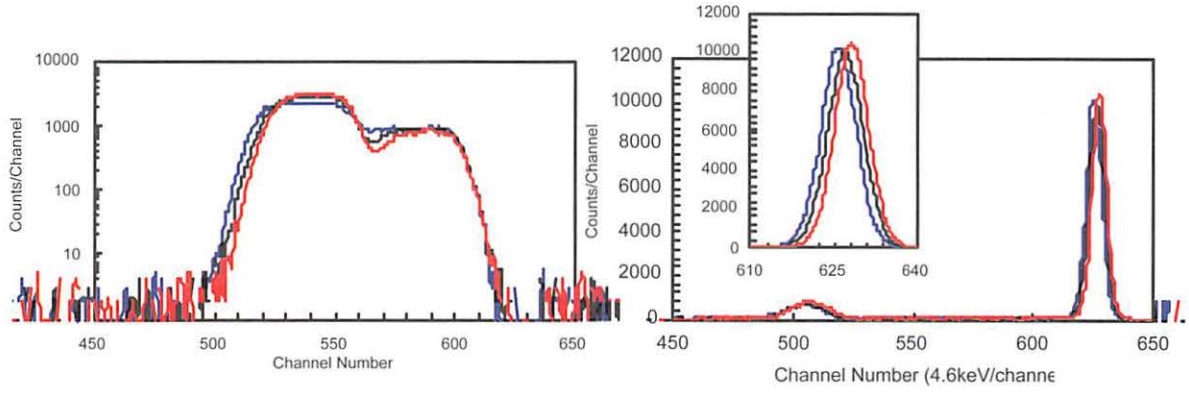

Figure 4. RBS and off-axis STIM spectra of Mylar Film (—: 0-0.3 μC, —:1.3-1.6 μC, —:2.4-2.7 μC).

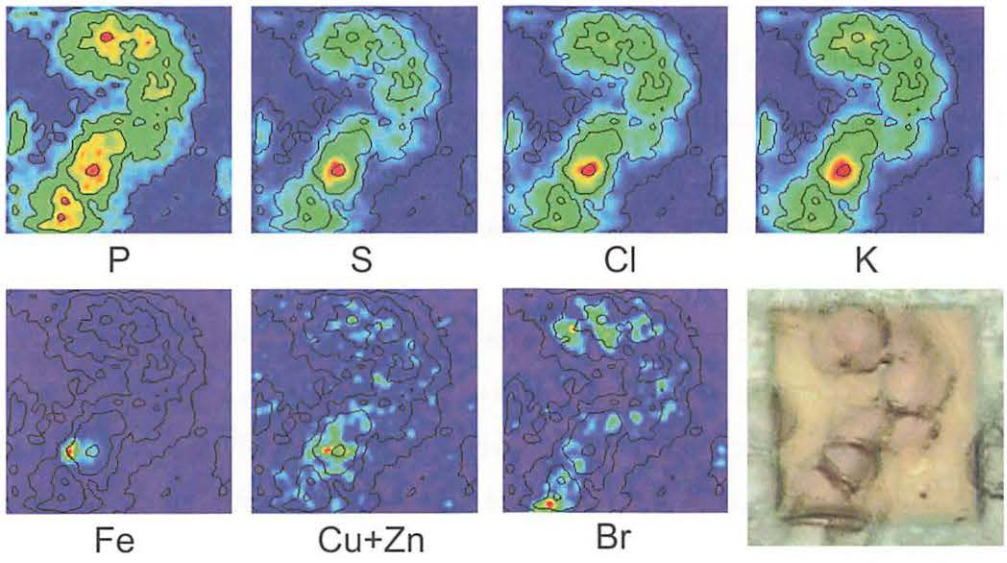

Figure 5. Elemental maps and optical images of bovine aortic endothelial (BAE) cells.

V. 2. Micro-beam Analysis at Tohoku University for Biological Studies

Matsuyama S.[1], Ishii K.[1], Abe S.[1], Ohtsu H.[1], Yamazaki H.[1], Kikuchi Y.[1], Amartaivan Ts.[1], Inomata K.[1], Watanabe Y.[1], Ishizaki A.[1], Barbotteau Y.[1], Suzuki A.[1], Yamaguchi T.[1], Momose G.[1], and Imaseki H.[2]

[1]*Graduate School of Engineering, Tohoku University*
[2]*National Institute of Radiological Sciences*

Introduction

The nuclear microprobe has been recognized as a powerful tool for analysis of single cell and tissue section in biological and biomedical research[1-3]. We have developed an in-air micro-PIXE system in collaboration with the Japan Atomic Energy Research Institute (JAERI) Takasaki[4,5] and have analyzed bovine aortic endothelial (BAE) cells, rat basophilic leukemia (RBL) cells and tumor cells AH109A implanted into Donryu rat[6-8]. We have also constructed a nuclear microbeam system at the Dynamitron laboratory of Tohoku University for biological applications in 2002-2003. A spatial resolution less than 1 μm is achieved with a beam current of 40 pA[9,10]. A simultaneous PIXE, RBS and a consecutive STIM analysis can be carried out using in-air or in-vacuum geometry in this system. This system allows to measure structural and elemental properties, which are important for biological studies. However, measurement efficiency of the previous system was not well optimized requiring a long time to obtain sufficient statistics for X-ray and RBS analysis, in particular for low density single cell measurements. Here, we report on a reconfigured detection system with improved detection efficiencies and apply the system to measure spatial distributions of elements in mouse mast cells which are small and difficult to measure using the previous system. Mast cells play an important role in allergic reactions by preserving various kinds of bioactive substances in their secretory granules and releasing them after allergic stimulation. Several bioactive substances are reported to be conjugated with certain metal ions, therefore the elemental distribution of metal ions (including sulfur) inside the cells reflects the distribution of bioactive substances and will help to understand their activity. Although the sample preparation of adhesive cells for PIXE analysis had been already established, we had not yet established the preparation for

non-adhesive cell samples such as mast cell for PIXE analysis. In this study, we established a new sample preparation method suitable for non-adhesive single cell analysis, and undertook first measurements with the improved analysis system.

Microbeam Analysis System

The microbeam analysis system is applicable to experiments using either in-vacuum or in-air PIXE combined with RBS and STIM. Biological applications were mainly carried out using in-air geometry. The previous system consisted of a X-ray detector for PIXE analysis, ion implanted silicon detectors for RBS analysis and on/off axis STM analysis. Technical details of this system were presented in part in previous papers[9,10]. A schematic diagram of our new in-air analysis system is shown in figure 1. Proton beams are extracted through a thin (a few μm) polymer film, which also serves as a backing for the sample. Three samples are attached on a circular sample holder and can be changed using a stepping motor without breaking the vacuum. To reduce sample damage by the beam and to reduce energy loss in the STIM measurement, He gas was blown on to the sample[7]. Two X-ray detectors are set in vacuum at ±125 degree with respect to the beam axis. The first one has a large sensitive area (80 mm^2) and is suitable for trace elemental analysis. To reduce pile-up events or deformation of the spectrum by recoil protons, a Mylar filter or a Funny filter can be attached to the front of the detector. Maximum solid angle is ~0.08 sr. The second detector has a high-energy resolution (~136 eV), a thin Be entrance window (7.5 μm) and serves to detect low energy X-rays. The two-detector system enables to detect X-rays ranging from 1 keV to 30 keV with sufficient energy resolution and efficiency in a single measurement.

An annular surface barrier detector is set on the beam axis to detect back-scattered protons for RBS analysis. Scattering angle and counting rates can be controlled by changing the distance between the detector and a sample. The annular detector is highly efficient and improves the solid angle (~0.15 sr) without deteriorating angular spread and without interfering with the Si(Li) detectors. The detection efficiency increases 10 times compared to the previous system. Scanning transmission ion microscopy (STIM) can be used to observe the cell morphology. A Silicon PIN-photodiode (Hamamatsu S1223) has been newly installed for charged particle detection. Energy resolution of the Si PIN-photodiode is less than 14 keV and therefore superior to the ion implanted Si detector of larger diameter used in the previous system. The Si PIN-photodiode, a Faraday cup and

a scintillator are attached to a detector wheel off center to the beam axis (see Fig. 1). The detector wheel is turned slowly until the PIN-photodiode is centered on the beam axis, while monitoring the count rate of the detector and reducing beam current accordingly. Sample to detector distance is ~10 mm. Before and after simultaneous PIXE and RBS analysis, STIM data are acquired. Data are acquired in list mode by a multi-parameter data acquisition system. The list mode is very effective to monitor elemental loss during irradiation.

Sample Preparation

Mouse mast cell line P815, which has the characteristic features of non-adhesive type mast cells, was cultured in RPMI 1640 medium supplemented with 10% FBS (Fetal Bovine Serum). After washing three times with THAM (trishydroxymethylamino-methane)-HNO_3 buffer, the cell pellet was resuspended with 15 ml (equivalent to 3 x10^7 cells) of THAM-HNO_3 buffer and passed through Nuclepore filter of 0.22 μm pore size (Millipore, Isopore Membrane filter). Although trapped cells are not uniformly distributed, the region which is suitable for single cell analysis is found easily. Then, the Nuclepore filter is attached to the 5 μm polycarbonate foil which serves as beam exit window so that cells are inserted between Nuclepore filter and polycarbonate foil. The cells are cryofixed in isopentane solution at liquid nitrogen temperature for 24 hours in vacuum[6-8].

Results

The new analysis system was employed. STIM was used to find single cells and proved to be fast and efficient especially when cells are not uniformly distributed. The cell matrix composition (C, N and O), density and thickness were determined by RBS. PIXE provided the elemental information. Typical elemental maps of mast cell are shown in figure 2. It took 90 minutes to obtain the elemental images with beam currents of ~40 pA, a beam spot size of 1×1 μm^2 and scanning size of 20×20 μm^2. Quantitative PIXE analysis was performed using the GeoPIXEII software[11]. Distributions of P, S and K elements are clearly seen and correspond to the C, O maps. Cells keep their original shape and cryofixation seems to be successful. Phosphorus appears to be concentrated in the cell nucleus but S and K are more uniformly distributed through the cell. Iron is strongly localized in one cell only but has been also seen in bovine aortic endothelial (BEA) cells in a previous study[10]. The amount of P in a cell is less than 5 pg, which is one half of the

STIM was also used to monitor the loss of cell matrix elements before and after analysis. Typical STIM maps (density maps) are shown in Fig. 3 before and after irradiation. Before irradiation, cells are clearly seen and correspond to elemental maps. However, cell density is reduced and they are hardly recognized after irradiation. Figure 4 shows the energy loss spectra in the cell at (X 30, Y 50) position in fig.3 and in the backing region around (X 25, Y 13) position before and after irradiation. While the high energy shift corresponding to mass loss is clearly seen in cell region, only peak broadening by increasing inhomogeneity are seen in the backing region. This shows that morphological change has occurred by irradiation, and cell thickness or density is reduced to ~60% of the initial value. The RBS data are consistent with STIM data. However loss of heavy elements (A>20) was not observed in PIXE data indicating that mass loss is from light elements (A<20) only. When mass normalization is needed for analysis, STIM data measured before irradiation should be used even in in-air analysis.

Simultaneous measurements of PIXE, RBS and consecutive STIM employ complementary data and are therefore a powerful tool for cell analysis. We established the preparation method for non-adhesive cells using Nuclepore filter to trap the cells on it for PIXE analysis. This sample preparation has several advantages over the previously reported preparation methods[3,12]; e.g. 1) the cells which exist in diluted suspension are concentrated, 2) the sample preparation time is short by passing excessive medium through the filter, 3) the recovery of cells used in the preparation is high because most of them are trapped on the filter. These advantages lead to a wide range of applications using non-adhesive cells in micro-PIXE analysis.

Acknowledgements

This study was partly supported by Grant-in-Aid for Scientific Research (S) No. 13852017 from the Ministry of Education, Culture, Sports, Science and Technology, Japan. The authors would like to appreciate the help of K. Komatsu, T. Nagaya and C. Akama in constructing the micro-beam and target system.

References

1) Moretto Ph., Llabador Y., Nucl. Instr. Meth. **B130** (1997) 324.
2) Labador Y., Moretto Ph., Applications of Nuclear Microprobes in the Life Science, Singapore: World Scientific (1998).
3) Hogarth A.N., Thong P.S.P., Lane D.J.W., Watt F., Nucl. Instr. Meth. **B130** (1997) 402.
4) Matsuyama S., Ishii K., Sugimoto A., Satoh T., Gotoh K., Yamazaki H., Iwasaki S., Murozono K., Inoue J., Hamano T., Yokota S., Sakai T., Kamiya T., Tanaka R., Int. J. PIXE **8** (1998) 203.

5) Sakai T., Hamano T., Hirao T., Kamiya T., Murozono K., Inoue J., Matsuyama S., Iwasaki S., Ishii K., Nucl. Instr. Meth. **B136-138** (1998) 390.
6) Ishii K., Sugimoto A., Tanaka A., Satoh T., Matsuyama S., Yamazaki H., Akama C., Amartivan Ts., Endoh H., Oishi Y., Yuki H., Sugihara S., Satoh M., Kamiya T., Sakai T., Arakawa K., Saidoh M., Oikawa S., Nucl. Instr. Meth. **B181** (2001) 448.
7) Sugimoto A., Ishii K., Matsuyama S., Satoh T., Gotoh K., Yamazaki H., Akama C., Int. J. PIXE **9** (1999) 151.
8) Tanaka A., Ishii K., Komori Y., Matsuyama S., Satoh T., Gotoh K., Yamazaki H., Akama C., Int. J. PIXE, **12** (2002) 79.
9) Matsuyama S., Ishii K., Yamazaki H., Sakamoto R., Fujisawa, M. Amartaivan Ts, Ohishi Y., Rodoriguez M., Suzuki A., Kamiya T., Oikawa M., Arakawa K., Matsumoto N., Nucl. Instr. Meth. **B210** (2003) 59.
10) Matsuyama S., Ishii K., Yamazaki H., Barbotteau Y., Amartivan Ts., Izukawa D., Hotta K., Mizuma K., Abe S., Oishi Y., Rodriguez M., Suzuki A., Sakamoto R., Fujisawa M., Kamiya T., Oikawa M., Arakawa K., Imaseki H., Matsumoto N., Int. J. PIXE **14** (2004) 1.
11) Ryan C.G., Van Achterbergh E., Yeats C.J., Drieberg S.L., Mark G., McInnes B.M., Win T.T., Cripps G., Suter G.F., Nucl. Instr. Meth. **B188** (2002) 18.
12) Ren M.Q., Thong P.S.P., Kara U., Watt F., Nucl. Instr. Meth. **B150** (1999) 179.

Figure 1. Schematic Diagram of the Target Chamber.

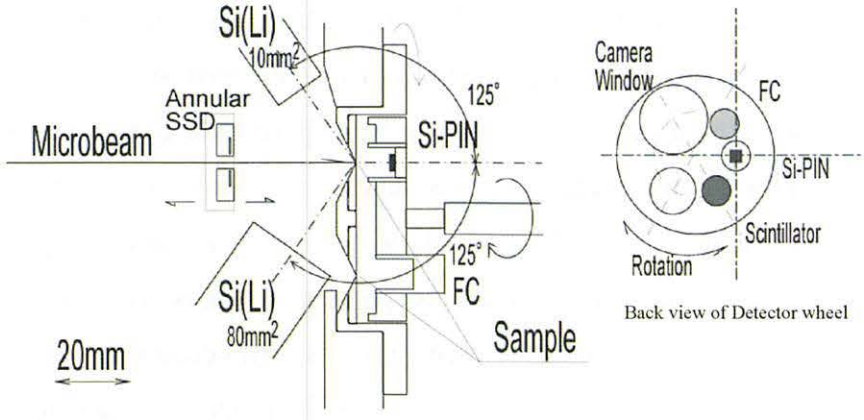

Figure 2. Elemental Maps of Mast Cell. Scanning area is $20 \times 20\ \mu m^2$.

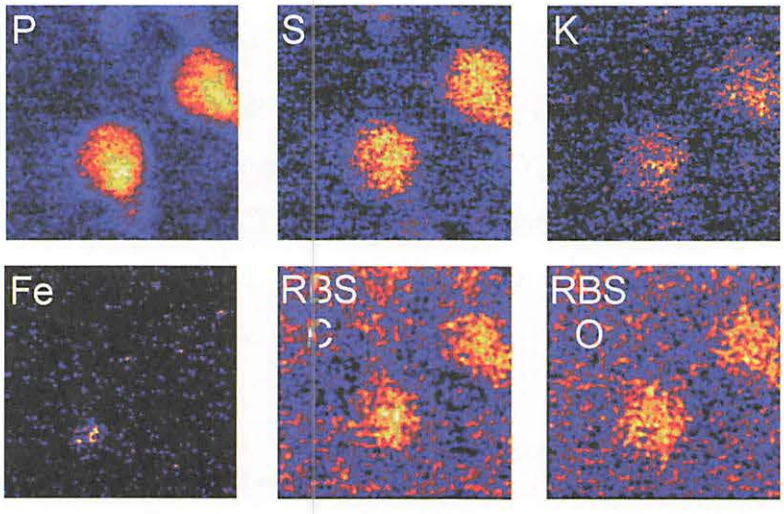

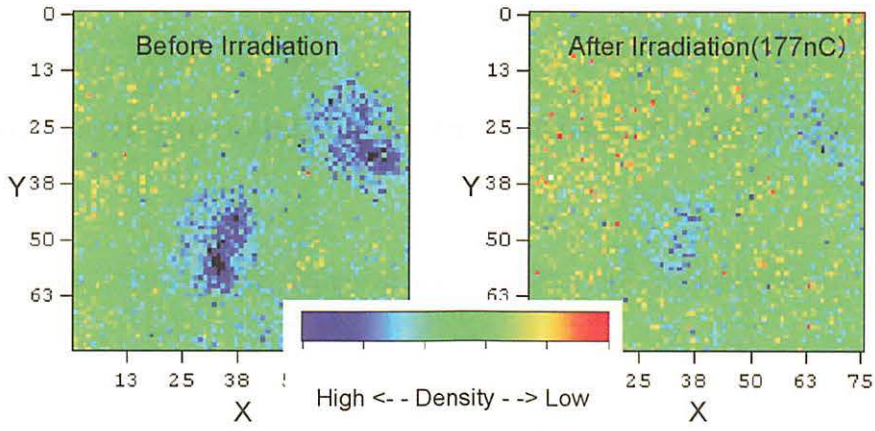

Figure 3. STIM maps before and after irradiation.

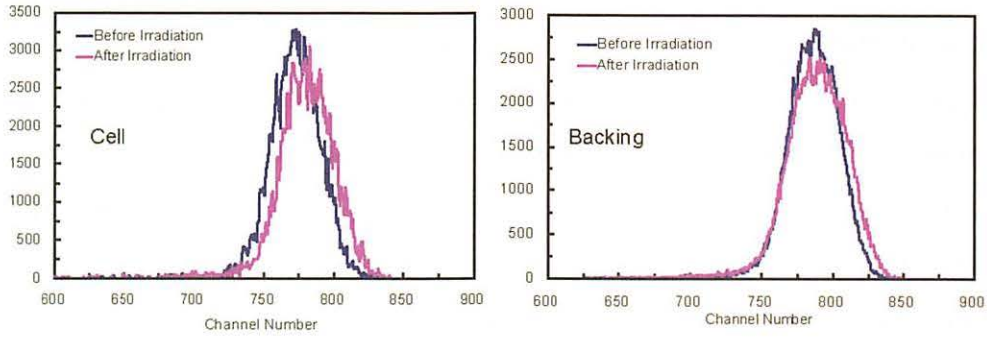

Figure 4. Energy loss spectra in cell at (X 30, Y 50) in Fig. 3 and backing regions around (X 25, Y 13) in Fig. 3 before and after irradiation.

V. 3. Chemical State Analisis of Cr Compounds Using Heavy ion PIXE

Ishii K., Amartaivan Ts., Yamazaki H., Matsuyama S., Kawamura Y., Oyama R., Ishizaki A., and Momose G.

Graduate School of Engineering, Tohoku University,

Introduction

The toxicity of heavier elements differs widely in their chemical state as well as there concentrations. Therefore, trace heavy element analysis with their chemical state and high sensitivity is of great importance for environmental monitoring. Particle induced x-ray emission (PIXE) is a powerful technique for quantitative analysis. Usually proton beams with an energy around 3 MeV are used in PIXE offering high sensitivity[1]. Since chemical shift is very small and difficult to measured with conventional Si(Li) detector, high sensitive measurement with chemical state is impossible in this condition.

The sensitivity of PIXE strongly depends on the X-ray production cross-sections, which are proportional to the square of the projectile charge[2] it can be expected that the use of heavy ion beams will improve the sensitivity of the analysis considerably. The lower limit of detection (LLD) in the PIXE analysis using 70 MeV carbon ions is improved 2-4 times compared to that using proton bombardment for heavier elements[3].

Since chemical change due to chemical state of the elements will be expanded due to multiple ionization, it may be measured with a conventional Si(Li) detector. In the last report, the three parameters, the relative change of an intensity ratio of k_β and k_α (Intensity Ratio), a ratio of k_β and k_α line width (line width ratio) and an energy difference between k_β and k_α line (relative energy shift), were measured using 70 MeV carbon ions and 3 MeV protons. Changes in those parameters were corresponds to their chemical state. It shows that PIXE with heavy ions will lead to chemical state analysis with high-sensitivity. Here, the Ar ion beams of 78 MeV are applied to chemical state analysis using PIXE. Probability of multiple ionization for Ar ion beams of 78 MeV is higher than that for C ion beams of 70 MeV, which will increase sensitivity in determining chemical state with high sensitivity.

Experimental

Experiment for Ar ions was carried out at Cyclotron Radioisotope Center. Samples are $Cr_2(SO_4)_3$, $CrCl_3$, $Cr(NO_3)_3$, $K_2Cr_2O_7$, Cr metal, CrB_2, Cr_2O_3, CrB and $CrF_3.3H_2O$. The targets were placed at an angle of 45° with respect to the beam direction. X-rays emitted from the target were measured at an angle of 90° with respect to the beam direction, by a Si(Li) detector. 1 mm Mylar film was placed in front of the Si(Li) detector to reduce pile-up events. The energy calibration was obtained with characteristic x-rays from a ^{241}Am source.

Results

The relative change of an intensity ratio of k_β and k_α (Intensity Ratio), a ratio of k_β and k_α line width (line width ratio) and an energy difference between k_β and k_α line (relative energy shift) for Ar ions is shown 3-dimentionally in Figure 1, in comparison with the results for protons and carbon ions. The changes of these parameters are within experimental errors except for intensity ratio in case of proton bombardment and difficult to specify chemical state of the elements. In case of carbon and Ar ions, changes in parameters seem to correspond to chemical states. However, tendency of these parameter changes corresponds to chemical state is different for these ion bombardments. Figure 2 shows the 3-parameters results for mixed samples which contains elements of different chemical states with different composition. As expected the previous results in Fig. 1, values of mixed samples on these parameters are close to the values of the sample in single chemical state. Since these measurements were carried out within a few minute, PIXE with Ar ions will lead to chemical state analysis with high-sensitivity.

Acknowledgements

The authors thank the working group of the Cyclotron Radioisotope Center, Tohoku University for the operation and maintenance of the accelerator.

References

1) Johansson S.A.E., Campbell J.L., "PIXE A Novel Technique for Elemental Analysis", John Wiley & Sons Ltd. (1988) 32.
2) Ishii K., Orihara., H., Iwat, Y., Bessho K., Int. J. PIXE **4** (1994) 1.
3) Amartaivan Ts., Ishii K., Yamazaki H., Matsuyama S., Suzuki A., Yamaguchi T., Abe S., Inomata K., Watanabe Y., Proceedings of 10th international conference on PIXE and its applications, Portoroz, Slovenia, June 4-8, 2004.

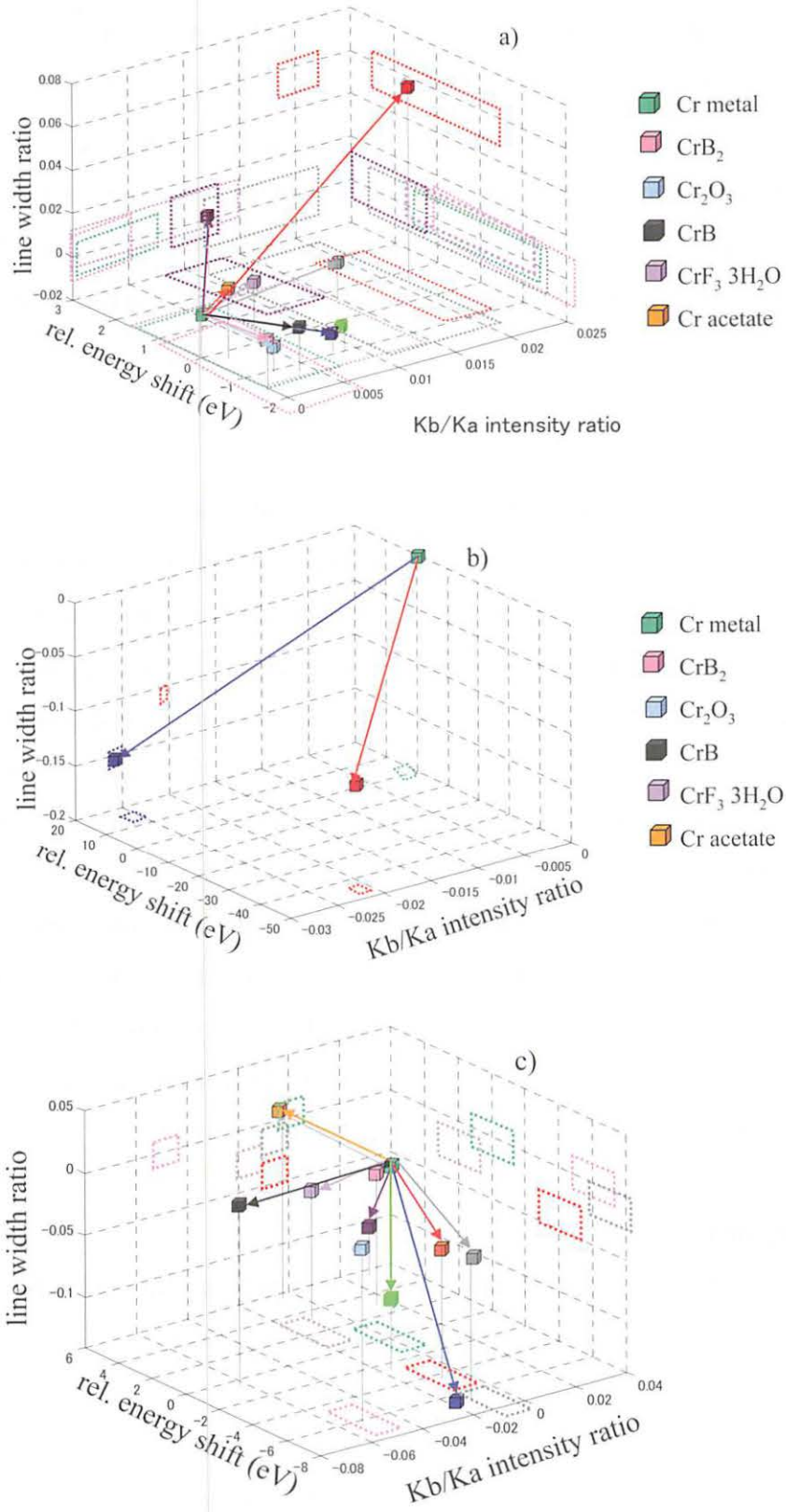

Figure 1. The relative change of an intensity ratio of k_β and k_α (Intensity Ratio), a ratio of k_β and k_α line width (line width ratio) and an energy difference between k_β and k_α line (relative energy shift) for proton, carbon and Ar ions.

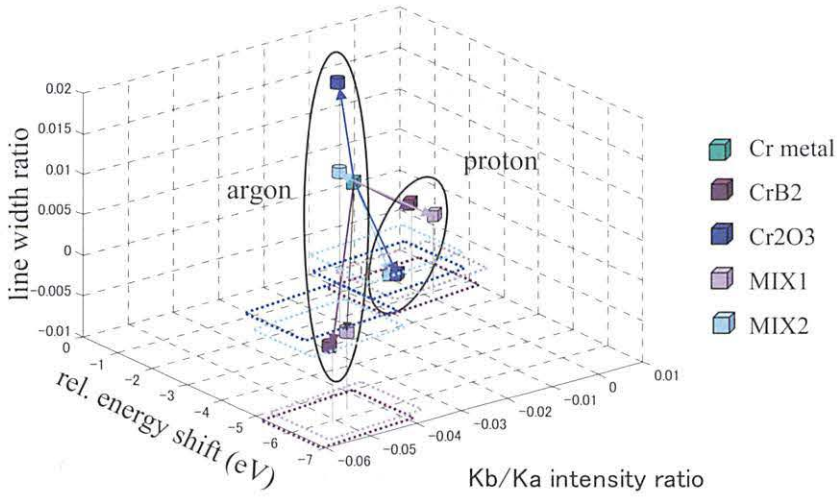

Figure 2. Relative changes of the 3 parameters of mixed samples for proton and Ar ions.

V. 4. Absorption of Arsenate and Arsenite by Arsenic Hyperaccumlating Fern (*Pteris vittata*)

Tashiro K.[1], Suto K.[1], Inoue C.[1], Matsuyama S.[2], Yamazaki H.[2], and Ishii K.[2]

[1]*Graduate School of Environmental Studies, Tohoku University*
[2]*Graduate School of Engineering, Tohoku University*

Phytoremediation using an arsenic hyperaccumulator, *Pteris vittata* L., has generated increasing interest worldwide, for it's both environmentally sound and cost effective. However, the mechanisms of arsenic uptake and accumulation by this plant are not clear at this time. This study shows the uptake of arsenate (As(V)) and arsenite (As(III)) using a hydroponic culture of *P. vittata*. The fern takes up both As(V) and As(III) from the culture which spiked with 50 mg of arsenic per litter, and can grow within 5 days of experimental period. Final amount of arsenic accumulated in the fern is 3.2 mg (As(V)), and 3.8 mg (As(III)). The submilli-scale distribution of elements by PIXE analysis clearly shows the accumulation of arsenic in fronds of *P. vittata*.

Introduction

Arsenic contamination of soils and groundwater from various sources such as mine and urban wastes, wood preservatives and pesticides is of great environmental problem[1,2]. A number of technologies for arsenic-contaminated soils have been proposed. However, most of them are generally expensive and may produce secondary wastes. Phytoremediation is an acceptable technology for relative lower level of arsenic contaminated soil because it is recognized cost-effective and environmental friendly process. Recently, *Pteris vittata* L., a kind of fern, has been found as an arsenic hyperaccumulator plant[3]. This species can accumulate up to 20 g/kg of arsenic in its above ground biomass. Recently, several other fern species have been reported to have ability to hyperaccumulate arsenic similar to *P. vittata*[4]. In case of *P. vittata* grown on arsenic-contaminated soil, most of the arsenic localized to the vacuoles in epidermal cell of fronds[3,5]. It is undoubtedly that arsenic enters in the roots and translocate to the fronds. Arsenic accumulated in the frond of *P. vittata* is mostly arsenite (As(III)) form, while

arsenic in the root occurs predominantly arsenate (As(V)) form[6]. It is believed that arsenate taken up by roots is converted to arsenite before or after it is translocated to the frond[7]. The entry system of arsenic to *P. vittata* is not studied well. Recently, Poynton et al.[8] showed that arsenate influx into the roots of hyperaccumlating ferns is greater than in nonhyperaccumulating ferns and speculated that the phosphate transporting protein has a responsibility for the influx. However, in our knowledge, there are no report concerning to arsenite influx into hyperaccumlating ferns. The aim of this work is to show the uptake of arsenate and arsenite into the *P. vittata* using chemical and PIXE analysis.

Materials and Methods

Plant material

P. vittata L.[3] was used throughout the experiment. Fern seedlings were used 3 months after spore germination. The roots were washed carefully in tap water to remove soil particles. The seedlings were then transferred to hydroponic water containing nutrient solution. To compare the effect of phosphate, phosphate-free nutrient solution was also used for several hydroponic experiments. The nutrient solution was aerated continuously. Seedlings were grown on the solution for 1 week in a growth camber with a 16 hours light period, 25 degree/20 degree day/night temperature and 70% relative humidity.

Arsenate and arsenite uptake experiments

After 1 week cultivation in hydroponic solution, the roots were washed well in tap water. Each seedling was placed in 100 ml conical beaker filled with 100 ml uptake solution. Then arsenic in the form of either As(V) as sodium arsenate ($Na_2HAsO_4\,7H_2O$), or As(III) as sodium arsenite ($NaAsO_2$) was added to the uptake solution to be final concentration 50 mg-As per litter. The seedlings treated were incubated in the growth camber at the same condition for a day. After 24 hours incubation, total weight of the beaker was measured to determine the amount of transpiration by the fern. Then the roots were washed and the seedling was placed new conical beaker filled with 100 ml of fresh solution containing the same kind and amount of arsenic. This cycle was repeated for 5 days. Arsenic concentration of the uptake solution was determined by ICP-MS (Hewlett Packard, HP-4500). Distribution image of elements in the plant sample was analyzed by submilli-PIXE camera equipped in the Dynamitron laboratory of Tohoku University. Details of the system and analytical methods are described previously[9,10].

Results and Discussion

Figure 1 shows a time course of arsenic concentration in hydroponic culture solution. Concentration of arsenic is obviously decreased from the initial concentration especially in the arsenite treatment at the first day while the concentration of arsenic is same in both of arsenate and arsenite treatment after 2 days. Although about 10% of the culture solution was decreased per day by transpiration, the arsenic concentration in the solution is not changed to the initial value in both cases. This result means that most of arsenic, both arsenate and arsenite, are transferred into the plant from root with a flow of water absorption. Figure 2 shows cumulative curve of arsenic in biomass of *P. vittata.* Final amount of arsenic accumulated in the fern is 1,500 mg per kg (wet weight) of the plant biomass in the arsenite treatment and 1,100 mg per kg in the arsenate treatment after 5 days. These values well agree to total amount of arsenic accumulated in the plant determined by whole plant analysis (data not shown). Based on these results it is concluded that arsenite influx into the roots of *P. vittata* is same as or greater than arsenate influx.

Submilli-PIXE analysis was applied to detect the distribution of arsenic in the plant. Figure 3 shows the distribution of arsenic in frond of *P. vittata* using submilli-PIXE camera. Arsenic was concentrated especially to near edge of the frond in both of arsenate- and arsenite-containing hydroponic culture. There is no significant difference for the distribution of arsenic in these two cases. On the other hand, it is difficult to detect the arsenic in root by submilli-PIXE analysis (data not shown). These results indicate that once arsenic, both arsenate and arsenite, enter from the medium, it translocates quickly from root to frond. Arsenic distribution image of a frond of *P. vittata* grown with or without phosphate are shown in Fig. 4. There is no effect of phosphate ion on arsenic accumulation so the entry system of arsenic to *P. vittata* must be proposed.

Conclusion

- Both arsenite and arsenate transferred into *P. vittata.*
- Phosphate does not effect on arsenic accumulation of *P. vittata*
- Arsenic was stored in frond of *P. vittata*, especially concentrated near edge.

Acknowledgements

This research was partially supported by Grant-in-Aid for Science Research from the Japan Society for Promotion Science (16656277).

References

1) Smith E., et al., Adv. Agron **64** (1998) 149.
2) Tu C., Ma L.Q., J. Environ. Qua.l **31** (2002) 641.
3) Ma L.Q., et al., Nature **409** (2001) 579.
4) Zhao F-J., et al., New Phytol. **156** (2002) 27.
5) Lombi E., et al., New Phytol. **156** (2002) 195.
6) Zhang W., et al., Sci. Total Environ. **300** (2002) 167.
7) Gumaelius L., et al., Plant Physiol. **136** (2004) 3198.
8) Poynton C., et al., Planta **219** (2004) 1080.
9) Matsuyama S., et al., Int. J. PIXE **8** (1998) 209.
10) Watanabe R., et al., Int. J. PIXE **14** (2004): 5.

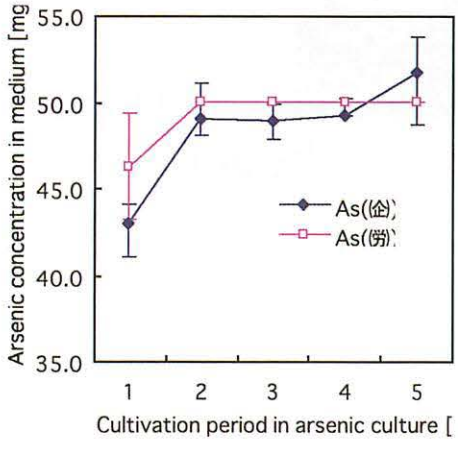

Figure 1. Time course of arsenic concentration in culture solution.

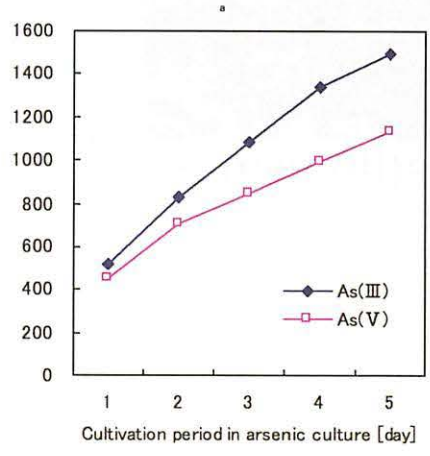

Figure 2. Cumulative curve of arsenic in biomass of *P.vittata*.

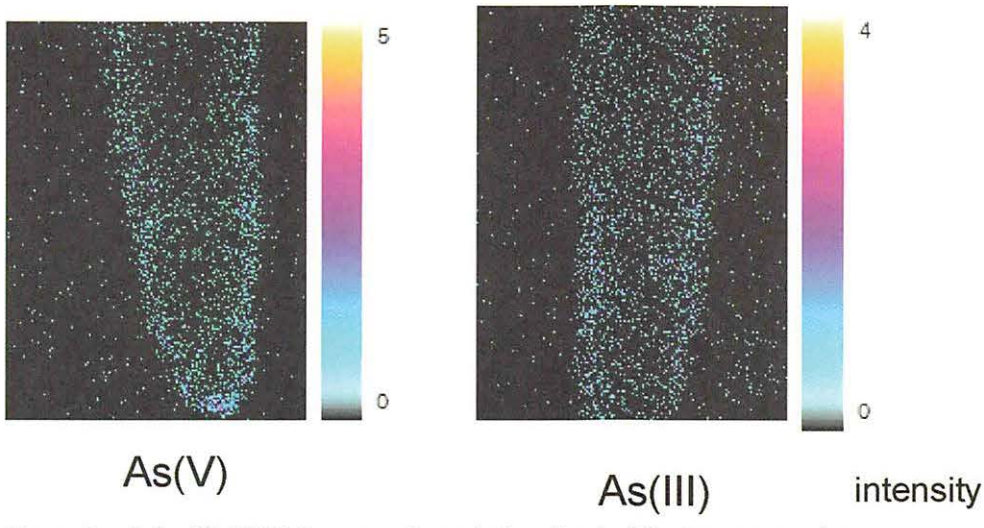

Figure 3. Submilli-PIXE dot-map of arsenic in a frond of *P. vittata* grown in an arsenate- or arsenite-containing hydroponic culture.

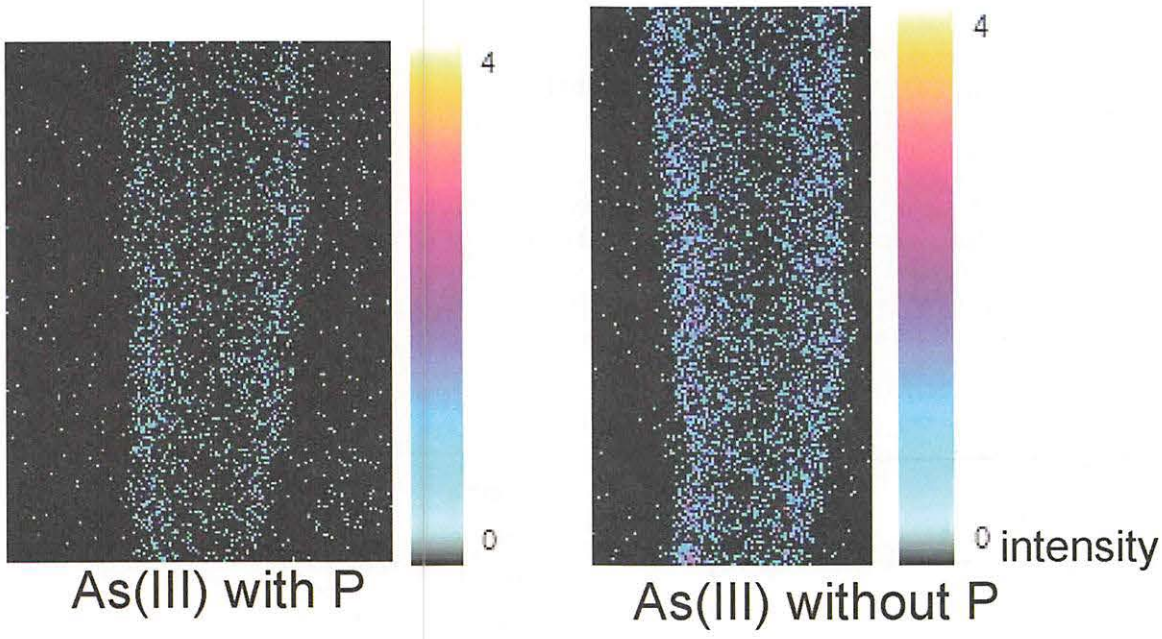

Figure 4. Submilli-PIXE dot-map of arsenic in a frond of *P. vittata* grown with or without phosphatecontaining hydroponic culture.

V. 5. Development of Monitoring System of Aqueous Environment by PIXE VII: Identification of Oxidation States of Trace-Level Arsenic in Environmental Water Samples

Yamazaki H., Ishii K., Matsuyama S., Kikuchi Y., Amartaivan Ts., Yamaguchi T., Momose G., Inomata K., Watanabe Y., Ishizaki A., Oyama R., and Kawamura Y.

Graduate School of Engineering, Tohoku University

Introduction

A large amount of hazardous chemicals is discharged into the environment in the process of industrial activities. Thus water quality monitoring becomes increasingly important as we must use new water resources such as deep underground water. The environmental degradation due to inclusion of a harmful element into flora and fauna strongly depends on the element's oxidation state. In monitoring pollution, it is thus necessary to determine both the quantity and the chemical state of a harmful element in environmental samples. Arsenite is more toxic than arsenate to the metabolism of flora and fauna and in Japan the quality limit of environmental water samples is legally set to lower than 10 ppb (ng/ml) for arsenic irrespective of the valence state[1]. However complex separation and pre-concentration procedures are required in order to determine arsenic concentrations below 10 ppb in environmental water samples by using the spectrophotometric method, graphite furnace atomic absorption spectroscopy or induced coupled plasma atomic emission spectroscopy[1-5]. PIXE using 3 MeV protons offers high sensitivity for arsenic[6]. Chemical state analysis of elements in percent-level concentrations can be determined by using the wavelength-dispersive PIXE technique, but this technique cannot be applied to assay the oxidation state of arsenic at trace level concentrations[7-8].

Experimental

An enhanced sample preparation method for PIXE analysis was developed for assaying the oxidation state of arsenic ions dissolved in water samples. Trivalent AsO_3^{3-} and pentavalent AsO_4^{3-} ions are separately adsorbed at pH 4 with indium hydroxide colloids,

generated in the solution by adding competing ions of the sorption reaction such as sulfates and phosphates. PIXE analyses of the two kinds of targets reveal the fractions of arsenic of the different oxidation states. This technique is combined with a 3-step target preparation method, previously developed for soluble and insoluble constituents in trace concentra- tions[9-11]. The multi-element analysis capability of PIXE provides information on elements that are discharged from an arsenic pollution source. These sample preparation techniques are then applied to analyze the arsenic concentration in a river basin, where hot springs are located upstream being a possible source for emitting arsenic.

The targets prepared were analyzed in a vacuum chamber by using the submilli-PIXE camera (3 MeV protons, 0.5-4 nA beam currents, 4x4mm scanning area, irradiation time 5-10 minutes) at Tohoku University, Japan[12]. A target containing AsO_4^{3-}, Fe^{3+} and Cu^{2+} of known amounts (40 ppb in a 25 ml solution) was prepared by a DBDTC-DBS pre-concentration technique[11] and used as an external standard for normalization of PIXE spectra from the filtration targets. In PIXE-spectrum analysis, we used a least-squares fitting computer code based on the pattern analysis method, which has been developed in our laboratory[13].

Results and discussion

Hydroxide colloids of trivalent or tetravalent metals are produced in a solution of pH > 3.5 and possess anion-exchange property on the acidic side of the isoelectric point located at pH 7 to 8. By changing the pH value, the collection rates of arsenic of AsO_3^{3-}or AsO_4^{3-} in 100 ppb concentrations were examined for hydroxides of Fe^{3+},Ga^{3+},In^{3+} and Zr^{4+} under the condition of coexisting representative constituents of river water like K^+, Cl^- and SO_4^{2-} in ppm-concentrations. In order to confirm separation of arsenic from lead that may cause an error to PIXE spectrum analysis of arsenic, test solutions were prepared containing Pb^{2+} in 50 ppb concentrations. None of the four sorbents showed perfect separation for arsenic of different oxidation states, but indium hydroxide colloids quantitatively adsorbed arsenates separating them from lead ions in the pH region of 4 to 5. The adsorption of coexisting ions in excess of more than 50 times higher concentrations had no adverse effect on the recovery of pentavalent arsenic with metal hydroxide colloids generated in test solutions. The detection limit was estimated to be 0.3 ppb As in a 25 ml solution based on exceeding the 3σ statistical error of background counts. It is clear that the quality of environmental water samples relevant to human life can be assessed for harmful arsenic at

the limit < 10 ppb by means of PIXE measurement using indium hydroxide targets scavenging arsenic selectively in a solution. The PIXE analysis's high sensitivity for arsenic is attributable to the high pre-concentration factor of 10^5 in preparation of indium hydroxide targets scavenging arsenate in solutions.

In order to improve separation of arsenic ions of different oxidation states, indium hydroxide targets were prepared for arsenic in 100 ppb concentrations by adding SO_4^{2-} and PO_4^{3-} in ppm-concentrations, as shown in Fig. 1. These anions compete with arsenate and arsenite ions when they are adsorbed with indium hydroxide colloids in a solution of pH 4. Figure 1-a reveals that sulfate cannot depress sorption of arsenite even in 50 ppm concentration but 1 ppm phosphate completely controls the arsenite sorption onto indium hydroxide colloids. The sorption of arsenate ions is not sensitive to addition of competing ions and the arsenate recovery decreases by 15% only in the case of coexistence with 5 ppm phosphate ions. As shown in Fig. 1-b, addition of 25 ppm sulfate and 1 ppm phosphate controls the arsenite sorption within 11% in a wide concentration region of 4 to 50 ppb arsenite, while almost all of arsenate is collected with hydroxide colloids of indium of 10 ppm concentrations in original solutions. These results indicate that thin and uniform targets of pentavalent arsenic ions are obtained well separated from trivalent arsenic ions under acidic condition at pH 4. The separation of AsO_4^{3-} from AsO_3^{3-} is ascribed to the fact that metal hydroxides possess an anion-exchange property with higher affinity for PO_4^{3-} than for CrO_3^{3-}. A complete separation of arsenic of different oxidation states was also confirmed under the same experimental condition in solutions containing 1ppm arsenate or arsenite ions. In the case of separation without coexistence of sulfate, more than 60% of indium hydroxide colloids were lost in filtration even after aging of colloids in a solution heated to 80 °C. It is suggested from these findings that coexistence of sulfate is indispensable to coagulate fine colloids of indium hydroxide into filterable particulates.

In order to confirm the applicability of the sample preparation technique to monitoring arsenic pollution in the environment, we collected 0.5 dm^3-volume samples at 7 places in the Natori river valley at a length of 35 km, where five different spas are located upstreams (Fig.2). Samples were also collected at five spas in upstream locations and at one place in a branch of this river where no spas exist. Four kinds of PIXE targets were prepared from each water sample using the indium hydroxide coprecipitation for arsenic and the three-step method developed previously, that is, the Nuclepore filtration target for insoluble constituents, the preconcentration target for trace amount of heavy metal ions

using a combination of chelation by dibenzyl-dithiocarbamate (DBDTC) ions with subsequent condensation into dibenzylidene-*D*-sorbitol (DBS) gels, and the deposit target of soluble major constituents.

Indium hydroxide scavenged targets with and without the oxidation reaction of arsenic ions by permanganate ions were prepared from four river water samples (P4, P6-P8) and five spa water samples. That is, the As(V) fraction is determined by PIXE analysis for indium hydroxide targets of non-oxidized samples containing sulfate and phosphate ions inhibiting arsenite sorption, and the total (As(III) +As(V)) fraction is determined by PIXE analysis for samples oxidized by permanganate ions. No appreciable difference is observed in arsenic concentrations analyzed for two kinds of targets prepared from each sample of spa water and river water, indicating that pentavalent arsenic is contained in soluble fractions of spa water samples and river water samples.

In PIXE analyses for three kinds of targets, filtration, deposit and preconcentration targets, fifteen elements were detected in samples collected along the 35-km valley of Natori river and hot springs located upstream of the river. Figure 3 shows concentrations of elements whose change is correlated with the As concentration change. Arsenic concentra- tions are largely different in five spa water samples and at the two furthermost downstream hot springs the concentration is beyond 100 ppb, the legal discharge limit of As to the aqueous environment. As a whole, arsenic concentration in the river rises gradually by influx from these spas and saturates downstreams of the hot springs. It is found that the arsenic concentration is quite low at the branch (P5) where no hot springs exist upstream. The highly sensitive PIXE analysis of arsenate scavenged by indium hydroxide precipitation allows to identify the source of arsenic at ultra low concentrations below the legal limit. In addition, a chemical back-ground concerning the distribution of arsenic in river water was also clarified by the PIXE analysis for the three kinds of targets. That is, concentrations of S, K, Mn, Ca and Sr are quite high in spa water samples collected at S2, S4 and S5, which results in the gradual increase of these elemental concentrations along the valley of Natori river.

References

1) Goulden P.D., Anthony D.H.J., *Anal. Chem.* **54** (1982) 1678.
2) Sandell E.B., "Colorimetric Determination of Traces of Metals," 3rd ed., Inter-science, New York (1965) 282.
3) Wilson C.L., Wilson D.W., "Comprehensive Analytical Chemistry," vol. 1c, Amsterdam, Elsevier (1962) 237.
4) Furman N.H., *ed.*, "Standard Methods of Chemical Analysis," 6th ed., vol. 1, New York, Van

Nostrand (1962) 106.
5) Haraguchi H., Inagaki K., Bunseki **1998-7** (1998) 494.
6) Ishii K., Morita S., Nucl. Instrum. Meth. **B3** (1984) 57.
7) Mukoyama T., Taniguchi K., Adachi H., Phys. Rev. **B 34** (1986) 3710.
8) Vrsic M., Kavcic M., Budnar M., Nucl. Instrum. Meth. **B211** (2003) 7.
9) Yamazaki H., et al., Int.J. PIXE **7** (1997) 31.
10) Yamazaki H., et al., Int.J. PIXE 7 (1997) 101.
11) Yamazaki H., et al., Int.J. PIXE **9** (1999) 83.
12) Matsuyama S., et al., Int.J. PIXE **8** (1998) 209.
13) Murozono K., et al., Nucl. Instrum. Meth. **B150** (1999) 76.

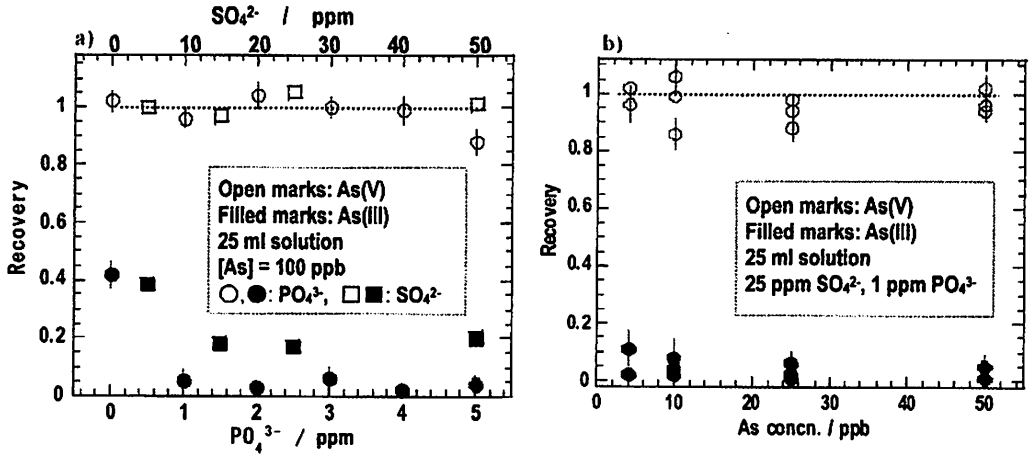

Figure 1. Separation of arsenic ions of different oxidation states by 10 ppm indium hydroxide scavenger prepared at pH4. PIXE measurement: 0.8-1.5 μC irradiation, Si(Li) detector with Mylar absorber of 200 μm thickness; a): Improvement of As separation by adding sulfate and phosphate ions; b) As separation in trace-level concentrations.

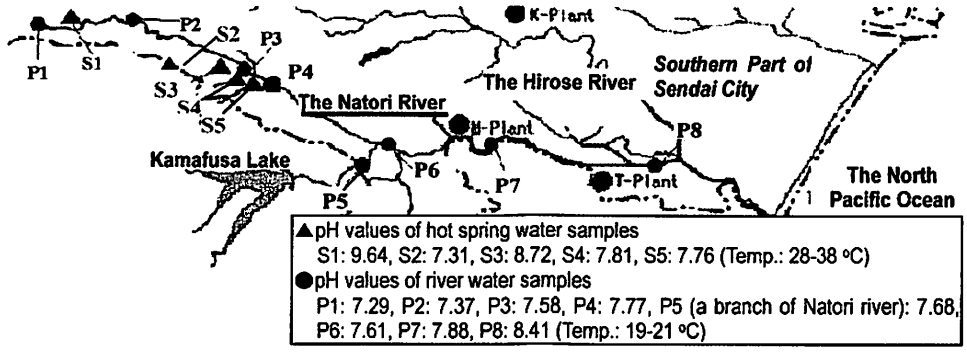

Figure 2. Location of sampling points in the Natori river basin over 35 km and pH values of water samples.

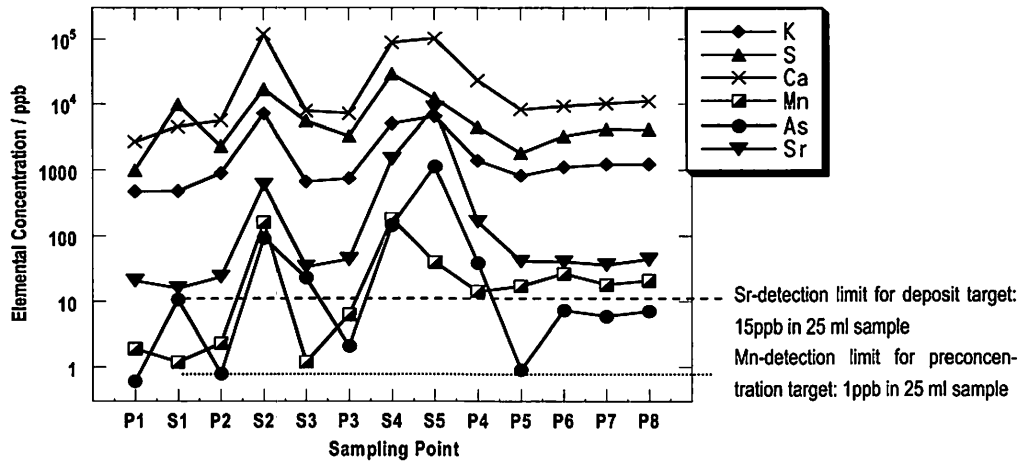

Figure 3. Elemental concentrations in river water and hot spring water samples. Sampling points of river water (P) and sampling points of upstream hot spring water (S) are the same as those in Fig. 1, 0.5-3 μC irradiation in PIXE measurements.

V. 6. Transfer Factors of Technetium-99 for Various Plants in Forests

Tagami K.[1], Uchida S.[1], and Sekine T[2].

[1]*Environmental and Toxicological Sciences Research Group, National Institute of Radiological Sciences*
[2]*Center for the Advancement of High Education, Tohoku University*

Introduction

Technetium belongs to the Mn group and it has no stable isotopes. Among its radioactive isotopes, ^{99}Tc is of potential long-term importance in the environment, because ^{99}Tc is a pure beta emitter (E_{max}=0.29 keV) and its half-life is 2.11 x 10^5 y. It is produced in the fissions of ^{235}U and ^{239}Pu at relatively high ratios of ca. 6%, which is similar to the values for ^{137}Cs and ^{90}Sr. Technetium-99 is widely distributed in the environment as a result of fallout from nuclear weapons testing and discharges from nuclear facilities. The quantity of ^{99}Tc produced by atmospheric nuclear weapon explosions was estimated to be 140 TBq using an equal fission yield to that of ^{137}Cs and actual ^{137}Cs deposition data[1)]. The release of ^{99}Tc by nuclear industries through 1986, as estimated by Luykx[2)], was of the order of 1000 TBq. This was mainly from nuclear fuel reprocessing and most of the ^{99}Tc was discharged into the sea and ^{99}Tc concentration in the terrestrial environment is very low[3)]. The amount introduced via nuclear medical use of ^{99m}Tc (half-life: 6.01 h) is negligible. For example, the amounts from ^{99}Mo-^{99m}Tc generators and ^{99m}Tc used during 2004 in Japan were 173 TBq and 325 TBq, respectively[4)], which corresponds to ca. 1.6 MBq of ^{99}Tc generation in total.

Due to very low concentration and analytical difficulties for determination of ^{99}Tc in environmental samples, there is a general lack of data on the levels in the literature. Therefore, the behavior of ^{99}Tc in the terrestrial environment is not well understood. However, it is necessary to obtain transfer parameters under natural conditions for a realistic long-term radiological assessment such as soil-to-plant transfer factors (TFs, concentration in plant/concentration in soil). Thus, we focused on the Chernobyl site where ^{99}Tc concentration levels have already been shown to be higher than those from global fallout Tc[5)]. The concentrations of ^{99}Tc in plant leaves collected in three forests

near the Chernobyl site were determined. The samples were leaves of raspberry, strawberry and pink plants, black alder, birch, cowberry and oak trees, and ferns. Since TFs are usually high in leafy vegetables and grass as reported in Reference 6, leaves of raspberry, strawberry and pink plants are of the most interest in this study for comparison purposes.

Experimental

A Tc-selective chromatographic resin (Eichrom Industries Inc., TEVA resin) was used for Tc purification. Deionized water (>17.6 MΩ) was used throughout the work. Technetium-95m, which was obtained from an Nb foil using the reaction ^{93}Nb (a, 2n) ^{95m}Tc, was applied to determine the recovery of ^{99}Tc in the samples during the chemical separation procedure. The ^{95m}Tc was made at Cycrotron and Radioisotope Center, Tohoku University[6]. A standard ^{99}Tc solution available from Amersham (Solution TCZ.44) was used for calibrating the ICP-MS.

Leaves of 27 plant samples were collected at the Chernobyl site in 1994 and 1995 by the Federal Office for Radiation Protection, Germany, assisted by Moscow State University, Russia, and the Research and Industrial Association 'Pripyat', Ukraine. The sampling was carried out in three forests, D1, D3 and K2, around the Chernobyl Nuclear Power Plant. Forests D1 and D3 were 28.5 km and 26 km to the south of the reactor, respectively, while forest K2 was 6 km to the southeast. Soil samples were also collected at the same sampling sites and the details were reported previously[5].

A simple wet digestion method in combination with an TEVA resin separation method was applied for ^{99}Tc. After incineration of the soil samples at 450°C, a certain amount of ^{95m}Tc was added and they were mixed uniformly. Then, Tc was extracted with 4M HNO_3 while heating the samples at 100°C in a glass beaker covered with a watch glass. The residue was removed by filtration and the solution was diluted to obtain the acidity of ca. 0.1M HNO_3 and passed through a TEVA resin column to purify and concentrate Tc isotopes. Technetium adsorbed on the resin was eluted with 5 mL of 8 M HNO_3 solution. The volume of the ^{99}Tc fraction from the TEVA column solution was reduced to near dryness (<70°C) and then dissolved in 5mL of 2% HNO_3 solution. Radiochemical recoveries of Tc plant samples were monitored with ^{95m}Tc activities. Then the solution was introduced into an ICP-MS (Yokogawa, PMS-2000).

Results and Discussion

Total chemical recoveries throughout the method with ^{95m}Tc ranged from 0.48 to 0.92 with an average of 0.76. No relation was found between sample amount and recovery. Three replicates of samples K2-94F-1 and D3-94G-1 were used in amounts of 1 - 2.6 g and 1.8 - 10.2 g, respectively, and there were no differences between their recoveries. However, the recoveries of two sub-samples of K2-94G-2 and D1-94G-1 differed by about 0.1 and 0.2, respectively; when sample amounts increased, the recoveries decreased. Possibly, plant matrices, such as K, Ca and Cl, would affect the ^{99}Tc recovery, especially at the TEVA resin separation steps.

Technetium-99 concentrations in all samples are listed in Table 1 and they ranged from <0.006 to 6.0 mBq g^{-1}. For 11 samples, especially in the tree group, it was hard to determine ^{99}Tc, because of its low concentration.

TF is defined as the ratio of activity concentration in plant (in Bq g^{-1} dry weight (DW)) to activity concentration in soil (in Bq g^{-1} DW). It has been noted that forest under story plants are expected to take up radionuclides mainly from organic layers and therefore, concentration of ^{99}Tc in organic soil would be important for estimation of its uptake. Thus, TFs were calculated in terms of activity concentration in a plant relative to activity concentration in organic soil. Table 1 also shows the TFs of Tc for all the samples. They ranged from <0.016 to 0.28 for Fern, 0.009 to 0.47 for Herb and <0.006 to 0.05 for Tree groups based on the ^{99}Tc contents of the organic layers. The highest TF was found in the leaves of raspberry. The observed-TFs were lower than the IAEA-compiled values of 8.1 - 2600 for leafy vegetables, fodder and grass[7]; other reported values are as listed in Table 2. Comparing the TF for Tc reported for various plants grown in soil, the present results were almost the same as the data observed in reclaimed land[10], although the data from pot experiments[11] were much higher.

From these results, we concluded Tc bioavailability in the natural environment would be lower than the bioavailabilities obtained from laboratory studies that used TcO_4^- to obtain Tc TFs. It is known that the most plant-available form of Tc is TcO_4^-, and other forms have less availability to plants. Thus, TcO_4^- was not the only Tc chemical from in these forests. Possibly most Tc was in less soluble form, such as organically bound forms, sesquioxide bound and lower oxidation forms[12].

Concerning the Herb group, the TFs were 0.17-0.47 at K2, 0.20-0.32 at D1 and 0.009-0.086 at D3. The TFs for the samples collected at D3 were lower than those at D1 and K2. This might be due to the fact that D3 was a so-called wet forest and reducing

conditions might possibly exist. The bioavailable Tc was presumably influenced by the soil redox conditions: Tc would be transformed from to a lower oxidation and less available form under a relatively low redox condition. Due to the relatively low redox conditions of the D3 site, the TFs were lower than those in K2 and D1 sites.

Thus, the low TFs we observed in this study implied that 8-9 years after ^{99}Tc release from the Chernobyl Nuclear Power Plant, Tc should have been transformed to insoluble or less plant-available forms. Technetium would not be in readily available form to plants in the natural environment.

References

1) Aarkrog A., Dahlgaard H., Hallstadius L., Holm E., Mattson S., Rioseco J., Technetium in the Environment (Desmet G. and Myttenaere C. eds.), Elsevier Appl. Sci. Pub., London (1986) 69.
2) Luykx F., Technetium in the Environment (Desmet G. and Myttenaere C. eds.), Elsevier Appl. Sci. Pub., London (1986) 21.
3) Tagami K., Uchida S., J. Nucl. Radiochem. Sci. **3** (2002) 1.
4) Japan Isotope Association, Statistics on the Use of Radiation in Japan (2005) 38.
5) Uchida S., Tagami K., Wirth E., Rühm W., Chemosphere **39** (1999) 2757.
6) Sekine T., Konishi M., Kudo H., Tagami K., Uchida S., J. Radioanal. Nucl. Chem. **239** (1999) 483.
7) IAEA, Handbook of Parameter Values for the Prediction of Radionuclide Transfer in Temperate Environments, Technical Reports Series No. 364. IAEA, Vienna, (1994) 14.
8) Vandecasteele C.M., Dehut J.P., Van Laer S., Deprins D., Myttenaere C., Health Phys. **57** (1989) 247.
9) Hoffman F.O., Garten C.T., Jr., Lucas D.M., Huckabee J.W., Environ. Sci. Technol. **16** (1982) 214.
10) Green N., Wilkins B.T., Davidson M.F., Hammond D.J., J. Environ. Radioactiv. **27** (1995) 35.
11) Echevarria G., Morel J.L., Florentin L., Leclerc-Cessac, E. J. Environ. Radioact. **70** (2003) 85.
12) Tagami K., Uchida S., Toxicol. Environ. Chem. **56** (1996) 235.

Table 1. Chemical recovery of ^{95m}Tc, concentration of ^{99}Tc and transfer factor in plant samples collected in forests within the 30-km zone around the Chernobyl Nuclear Power Plant.

Plant type	Place		Tc-95m Recovery	Tc-99 mBq g^{-1} dry	Transfer factor
Fern	K2	94Fern-1a	0.847	2.42 ± 0.18	
		94Fern-1b	0.895	2.37 ± 0.29	
		94Fern-1c	0.884	2.31 ± 0.26	0.276 ±0.019
		95Fern-1	0.829	0.603 ± 0.045	0.045 ±0.003
		95Fern-2	0.749	3.79 ± 0.35	0.283 ±0.026
	D3	94Fern-1	0.661	< 0.040	< 0.016
		95Fern-2	0.483	< 0.031	< 0.018
		95Fern-3	0.844	< 0.069	< 0.040
Glass	K2	94Glass-1	0.599	4.04 ± 0.42	0.470 ±0.051
		94Glass-2a	0.747	1.30 ± 0.17	
		94Glass-2b	0.852	1.57 ± 0.16	0.168 ±0.015
		95Glass-1	0.739	6.02 ± 0.52	0.450 ±0.039
		95Glass-2	0.762	3.61 ± 0.33	0.269 ±0.025
	D1	94Glass-1a	0.596	0.254 ± 0.022	
		94Glass-1b	0.824	0.451 ± 0.090	0.318 ±0.042
		94Glass-2	0.563	0.222 ± 0.017	0.200 ±0.015
		95Glass-1	0.901	0.257 ± 0.021	0.231 ±0.019
	D3	94Glass-1	0.868	0.215 ± 0.016	0.092 ±0.006
		94Glass-2	0.706	0.094 ± 0.008	0.039 ±0.003
		94Glass-3	0.553	0.128 ± 0.011	0.053 ±0.004
		95Glass-1	0.915	0.016 ± 0.003	0.009 ±0.002
Tree	D1	94Tree-1	0.898	< 0.006	< 0.006
		95Tree-1	0.883	0.013 ± 0.001	0.012 ±0.001
	D3	94Tree-1	0.878	< 0.035	< 0.014
		94Tree-2	0.652	< 0.040	< 0.016
		94Tree-3	0.850	< 0.056	< 0.023
		94Tree-4	0.633	< 0.028	< 0.011
		95Tree-1	0.685	< 0.028	< 0.016
		95Tree-2	0.543	< 0.023	< 0.013
		95Tree-3	0.856	< 0.028	< 0.016
		95Tree-4	0.843	0.094 ± 0.011	0.055 ±0.007

Table 2. Transfer factors for Tc reported for various plants grown in soil.

Crop	TF	Conditions	Reference
Grass pasture mixture	6	Lysimeter	8
Herbaceous vegetation	6.7-22	Silt loam, Field	9
Grass	0.91-3.02	Reclaimed land, Field	10
Rye grass	44-371	Cambisol, Pot	11
Herbaceous vegetation	0.009-0.47	Podzol, Peat-gley, Field	This study

VI. RADIOCHEMISRTY AND NUCLEAR CHEMISTRY

VI. 1. Investigation of Excitation Function for $^{238}U(^{12}C,4\text{-}6n)^{244\text{-}246}Cf$

Takamiya K.[2], Kasamatsu Y.[3], Ohtsuki T.[1], Yuki H.[1], Takabe T.[3], Nakashima K.[3], Hasegawa H.[3], Shinohara A.[3], Shibata S.[2], Mitsugashira T.[4], Sato N.[5], Suzuki T.[5], Miyashita Y.[5], Shinozuka T.[5], Kikunaga H.[6], and Nakanishi T.[6]

[1]*Laboratory of Nuclear Science, Tohoku University*
[2]*Research Reactor Institute, Kyoto University*
[3]*Department of Chemistry, Osaka University*
[4]*Institute of Materials Research, Tohoku University*
[5]*Cyclotron Radioisotope Center, Tohoku University*
[6]*Department of Chemistry, Kanazawa University*

The investigation for the excitation function of $^{238}U(^{12}C,xn)$ reaction has been carried out by on-line and off-line measurement system. An He-jet transport and a rotating-wheel measurement system was used for on-line experiments, and off-line experiments were carried out by radiochemical method. Furthermore, a simple and unique method of target preparation using a membrane filter of an Al_2O_3 disk (25 $\mu m/cm^2$ in thickness) that can be useful with precipitation after filtering the target material[1)] was applied in these experiments. The ^{238}U deposited on prepared Al_2O_3 disk was irradiated with ^{12}C ions and the isotopes of Cf were produced with $^{238}U(^{12}C,4\text{-}6n)$ reactions. The obtained excitation functions of $^{244\text{-}246}Cf$ were compared with those obtained by other previous results.

The irradiation experiments were carried out using the 930-AVF cyclotron in the CYRIC. In order to measure isotopes which has various half-lives efficiently, two kinds of experiments, off-line and on-line experiments, were carried out. In the off-line experiments, uranium hydroxide collected on the membrane filter of an Al_2O_3 was used as the targets (300 $\mu g/cm^2$ in thickness). The target was mounted in an aluminum holder and placed in the reaction chamber on the end of a beam line as the sample side face to the upstream of ion beam. The energetic ^{12}C ions accelerated by the accelerator was irradiated to the target through a few aluminum degraders. The reaction products lost their kinetic energies in the target of filter and remained there. The irradiation time was varied from 20 - 40 min

according as the half-life of dominant isotope of Cf at the irradiation energy. The beam current was typically 150 particle-nA. After the irradiation, the target was dissolved in hydrochloric acid, and ^{252}Cf and Fe^{3+} ions were added as carrier materials. Sodium hydroxide solution was added to produce a precipitate. After repeating these procedures, the precipitate was dissolved in hydrochloric acid of 9 mol/L and poured into the anion exchange column (DOWEX 1X8, 200 - 400 mesh). Hydrochloric acid of 9 mol/L was injected to the column to elute the isotopes of Cf. Samarium was added to the eluent as a carrier material, and after that, ammonia water was added to precipitate as hydroxides of Cf and Sm. The precipitate was filtered and dried to prepare the measurement source for α-particle spectroscopy using SSBD.

In the on-line experiments, the same precipitation targets (200 μg/cm2 in thickness) or electrodeposited targets was used for the irradiation. The target was mounted in an aluminum holder and placed in the He-gas jet reaction chamber on the end of a beam course. The reaction chamber was connected to the He-gas (containing KCl clusters) jet transport system. He-gas (flow rate, 2 L/min) was applied through a KCl-cluster generator at 640°C. Reaction products were recoiled out from the targets by nuclear reactions, and kinetic energies were reduced in He-gas containing KCl clusters. The products adsorbed on the cluster were then transported with He-gas through a capillary tube to an automated rotating-wheel chamber placed in the room next door. Six α-particle detectors equipped with PIN-photodiode were installed in the rotating-wheel chamber to measure the α-particles emitted from the transported nuclides. The products transported by He-gas were blown onto polyethylene terephthalate films. The beam current was typically 150 particle-nA, that is almost the same as off-line experiments. Accumulation of the products on rotating-wheel and measurements of the α-particles of Cf isotopes was repeated at 10 - 20 min intervals according as the half-live of dominant isotope of Cf.

The α-particle spectra of ^{245}Cf and ^{244}CF, produced by $^{238}U(^{12}C, 5n)$ and $^{238}U(^{12}C, 6n)$ reactions, respectively, are shown in Fig. 1. The spectra illustrated in the upper and lower panels in this figure were obtained by off-line and on-line experiments, respectively, at the irradiation energy of 83 MeV. It was found that the energy resolution of the spectrum obtained by off-line experiment is better than that by on-line experiment. In the upper panel, the peak at 7.22 MeV of ^{244}Cf and that at 7.15 MeV of ^{245}Cf are clearly identified. On the other side, the spectrum obtained in the on-line experiments could be separated to several components by calculation with a computer; however, short-lived isotope of ^{244}Cf could be measured with enough statistics. Finally, we have obtained the

cross section of the $^{238}U(^{12}C,4\text{-}6n)$ reactions in several irradiation energies on target. The excitation functions of $^{238}U(^{12}C,4\text{-}6n)^{244\text{-}246}Cf$ are shown in Fig. 2 with those reported by Sikkeland et al.[2] as a function of laboratory energy system. In this figure, open and closed symbols show the results by the present work and by Sikkeland, respectively. We found that the cross sections for the $^{238}U(^{12}C,4\text{-}6n)$ were estimated to be one order of magnitude lower than those reported.

In order to examine the discrepancy between the results by our work and Sikkeland et al., the maximum cross sections for 5n reaction of ^{238}U and ^{244}Pu as a function of the proton number of the compound nuclei are shown in Fig. 3. There seems that the cross section values of the previous reports[3-6] decreases as the proton number increases in the both case of the targets of ^{238}U and ^{244}Pu. It was found that our present result is consistent with the systematics although the result by Sikkeland is inconsistent.

References

1) Takamiya K., et al., to be published.
2) Sikkeland T., Maly J., Lebeck D., Phys. Rev. **169** (1968)1000.
3) Andreyev A.N., et al., JINR Rep. E-7-93-57, Dubna (1993) 44.
4) Nishio K., et al., Phys. Rev. Lett. **93** (2004) 162701.
5) Lazarev Yu. A., et al., Phys. Rev. Lett. **75** (1995) 1903.
6) Lazarev Yu. A., et. al., Phys. Rev. C**62** (2000) 064307.

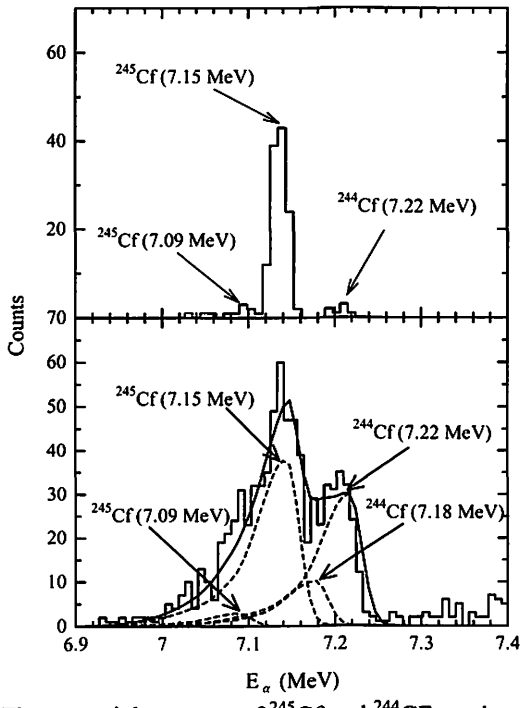

Figure 1. The α-particle spectra of ^{245}Cf and ^{244}CF produced by $^{238}U(^{12}C, 5n)$ and $^{238}U(^{12}C, 6n)$ reactions, respectively. The upper and lower panels show the spectrum for off-line and on-line experiments, respectively.

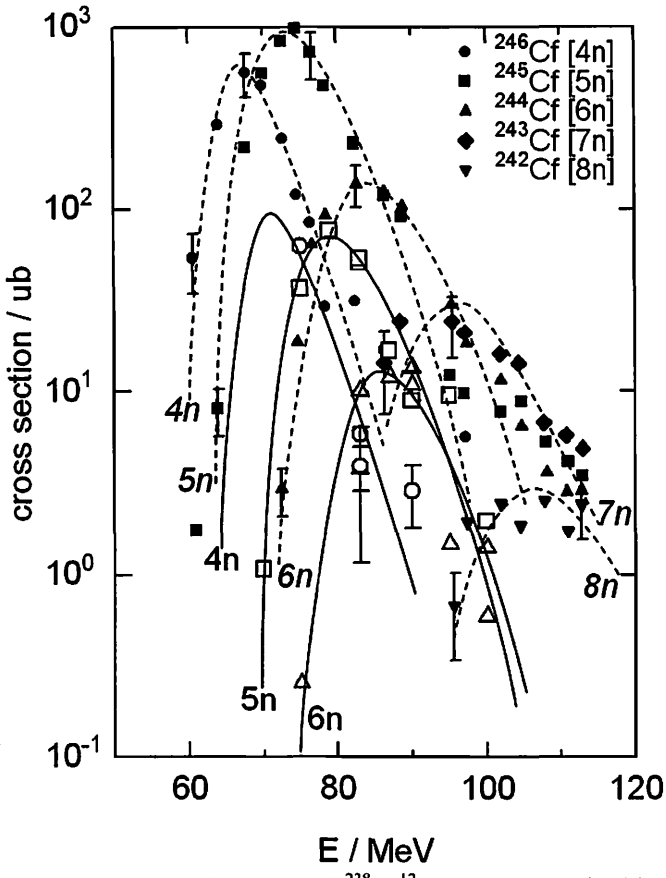

Figure 2. The excitation functions of $^{238}U(^{12}C,xn)$ obtained in this work (open symbols) and those reported by Sikkeland et al. (closed symbols) as a function of laboratory energy system.

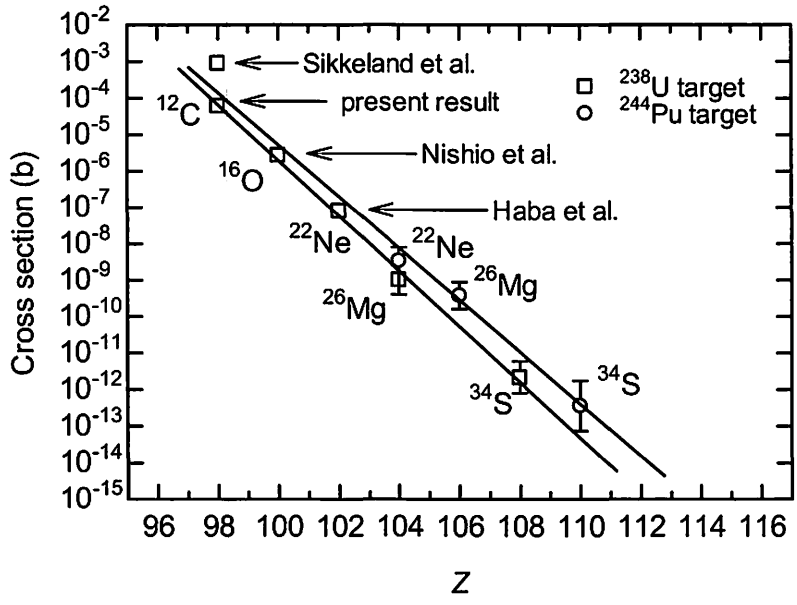

Figure 3. The systematics of the maximum cross sections for 5n reaction as a function of the proton number of compound nuclei.

VI. 2. Measurement of the Cross Section of the $^{40}Ar(\alpha,2p)^{42}Ar$ Reaction

Yuki H.[1], Satoh N.[2], Ohtsuki T.[1], Shinozuka T.[2], Baba M.[2], Ido T.[2], and Morinaga H.[3]

[1]Laboratory of Nuclear Science, Tohoku University
[2]Cyclotron and Radioisotope Center, Tohoku University
[3]Technische Universitat Munchen

Introduction

Radiation sources are great important not only for research in basic science, material science, medical and radiopharmaceutical use but also for education in those area, and even in that in high school.

A ^{42}Ar-^{42}K generator was firstly proposed by Morinaga, who produced ^{42}Ar by the $^{40}Ar(t, p)^{42}Ar$ reaction using tritium accelerator. The half-lives of each nuclide, ^{42}Ar (parent) and ^{42}K (daughter), are 33 years and 12 hours, respectively, and they are in correlation of a secular equilibrium as shown in Fig. 1. Therefore, one can use for long time as a ^{42}K generator if a sufficient amount of ^{42}Ar is produced.

However, no tritium accelerator is available nowadays. Therefore, $^{40}Ar(\alpha, 2p)^{42}Ar$ reaction should be used to produce the ^{42}Ar-^{42}K generator even though the reaction cross section might be smaller than that of the $^{40}Ar(t, p)^{42}Ar$ reaction. No evaluated data for the cross section of the $^{40}Ar(\alpha, 2p)^{42}Ar$ reaction measured experimentally have been reported so far. In order to investigate its availability and the effective production of ^{42}Ar, we have measured the excitation function of $^{40}Ar(\alpha, 2p)^{42}Ar$ reaction[1-3].

Experimental

Since the experimental details have been described in ref.[3], here we briefly show the experimental procedure. The stacked gas cell targets have been irradiated and the excitation functions has been measured by means of and a γ-ray spectroscopy without chemical separation. Irradiations were carried out five times by changing the beam energies of E_α=40, 50, 60, 70 and 80 MeV.

The target cells of quartz glass 30 mm long and 30 mm inside diameter with 0.05

mm windows of polyimide foils (Kapton, Goodfellow Metals, England) were used to the irradiation. The cells were filled with natural argon gas by 1 atm. Thereafter four cells were set in a cylindrical cell holder at the beam course of CYRIC for the irradiation with the α-particles. The irradiated time was set in 7-9 hours by 500 nA. After the irradiation, the γ-rays emanating from ^{42}K were measured with a Ge detector coupled with multi-channel analyzer. Since the ^{42}Ar is 100 % β^-decay nuclide, the amount of ^{42}Ar can be deduced by an amount of ^{42}K by 1524 keV γ-ray, which is under correlation with a secular equilibrium. However, the ^{42}K was also produced simultaneously by the ^{40}Ar(α, pn)^{42}K reaction, An amount of ^{42}K produced by the decay of ^{42}Ar was deduced after the decay out of ^{42}K produced by the ^{40}Ar(α, pn)^{42}K reaction.

Results and Discussion

The cross sections of ^{40}Ar(α, 2p)^{42}Ar and ^{40}Ar(α, pn)^{42}K reactions obtained in the present work are shown in Fig.2. The energies of α-particles at midpoints of each target cell were determined by the calculation of energy degradation in Ar gas, air, Harvar, polyimide and Cu foils using TRIM code[4]. Horizontal error in each energy scale were calculated by the energy degradation and the straggling of α-particles in Ar gas in each target cell, and which were almost inside each symbols in Fig. 2. Vertical error of the cross sections dominates the statistical errors and the uncertainty of the efficiency of Ge detector.

The cross section of ^{40}Ar(α, pn)^{42}K reaction has been presented by Tanaka *et al.*[5] so far, and it was also shown in Fig.2. It should be noticed that our result is fair agreement with that obtained by Tanaka *et al.* The calculated cross sections by using ALICE code[6] are also given in Fig.2. From the figure, it seems that the calculated values for the cross section of the ^{40}Ar(α, 2p)^{42}Ar with ALICE code can be overestimated in 30 MeV < E_α< 60 MeV and that for the ^{40}Ar(α, pn)^{42}K reaction can also be underestimated in E_α > 40 MeV.

References

1) Nozomi N., et al., CYRIC Annual Report (2003) 127.
2) Yuki H., et al., CYRIC Annual Report (2003) 130.
3) Yuki H., et al., CYRIC Annual Report (2004) 109.
4) Ziegler J.F., Biersack J.P., Littmark U., The stopping and range of ions in solids, Pergamon, New York (1984).
5) Tanaka S., Furukawa M., Mikumo T., Iwata S., Yagi M., Amano H., J. Phys. Soc. Jpn. **15** (1960) 952.
6) Blann M., Vonach K.H., Phys. Rev. C **28** (1983) 1475.

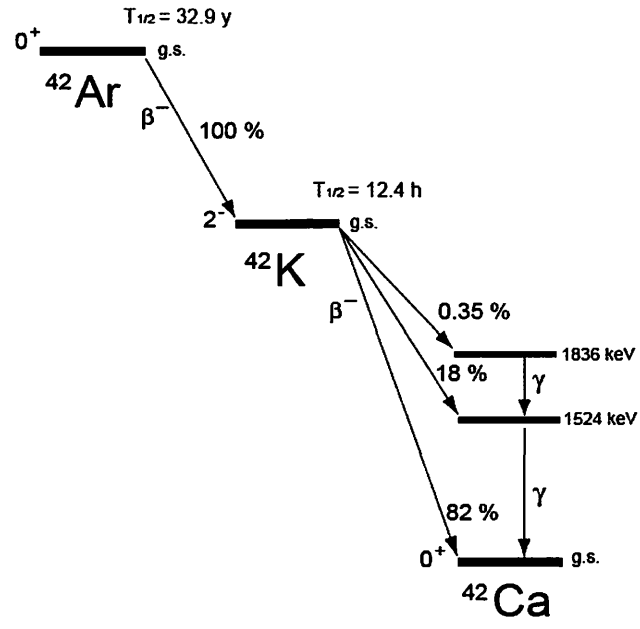

Figure 1. Decay scheme of Ar-42 and K-42.

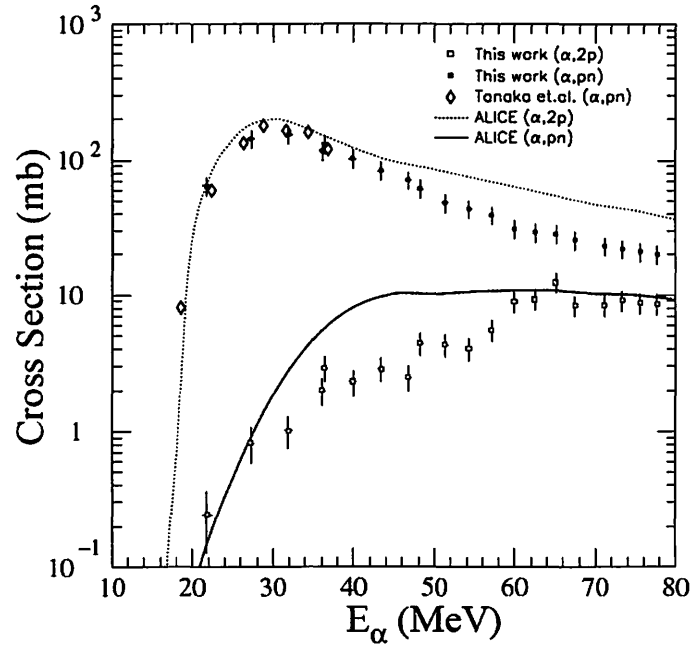

Figure 2. Comparison of the experimental and calculated excitation functions for the (α, 2p) and (α, pn) reaction on Ar-40 target.

VII. RADIOPHARMACEUTICAL CHEMISTRY AND BIOLOGY

VII. 1. Development of a Miniature Module for On-column Preparation of [^{11}C]Methionine from [^{11}C]Metyl Triflate

Watanabe T.[1], Ishikawa Y.[2], Ishiwata K.[3], Sato T.[1], and Iwata R.[2]

[1]*Sumitomo Heavy Industries, Ltd.*
[2]*Cyclotron and Radioisotope Center, Tohoku University*
[3]*Tokyo Metropolitan Institute of Gerontology*

L-[*S-methyl*-^{11}C]Methionine ([^{11}C]MET) is one of the most widely used amino acids for PET oncology. Due to its short half-life repeated preparations of [^{11}C]MET two or three times a day are often needed for routine PET practice. Therefore, a simple synthesis method without HPLC purification or evaporation is desirable for routine preparations. Pascali et al. developed a simple synthesis method using on-column labeling on a disposable solid phase extraction column[1]. However, this method requires the use of EtOH in the precursor solution for efficient trap of flowing [^{11}C]CH_3I and consequently, the removal of EtOH from a product solution with a rotary evaporator is an inevitable procedure in Japan according to the regulations. Någren et al. reported on the method for synthesizing [^{11}C]MET in an aqueous solution using [^{11}C]CH_3OTf[2]. We combined the above two methods and realized a simple automated method on a miniature module for routine preparation of [^{11}C]MET.

[^{11}C]CH_3I or [^{11}C]CH_3OTf was prepared by the gas phase method. Each labeled precursor was directed to a tC18 Sep-Pak Plus cartridge, which had been loaded with 0.2 mL of a solution of L-homocysteine thiolactone HCl (6 mg dissolved in 1 mL of 0.1 M NaOH) followed by purging the tubing and the tC18 Sep-Pak Plus cartridge with He and the radioactive fraction breaking through was trapped in charcoal. The trapping efficiency by the tC18 was evaluated. The [^{11}C]MET produced on the tC18 cartridge was then eluted with physiological saline (4 mL). The eluate was passed through a combined ion exchange cartridges of Accell Plus QMA Light and CM for neutralization. The solution was finally collected in a vented sterile vial through a 0.22 μm sterile membrane filter.

A miniature module for the above synthesis procedures is shown in Fig. 1. It consisted of a synthesis block, where microsolenoid valves, Sep-Pak cartridges and vials

(15 mL) were assembled on a manifold block (D. 100 x W. 120 x H. 100 mm), a miniature heater for a AgOTf column, a manifold 6-way switching valve and an interface/power supply/relay box. Advantages of manifolds are:

- Reduction of equipment space requirements.
- Elimination of external connections between valves.
- Combination of valves and pumps and vessels into a single component.
- Reduction of internal volumes between valves and thus loss of materials during transfers.

The module was controlled using a LabVIEW program on a PC through USB.

[^{11}C]CH_3OTf was trapped in 98% efficiencies on a tC18 cartridge preloaded the precursor solution, while [^{11}C]CH_3I was only trapped in 4%. As shown in Table 1, a single use of cation exchange cartridge for simply removing Na^+ resulted in the decrease in radiochemical purity down to 84% from a nascent high radiochemical purity of >97%. This was probably due to the decomposition of [^{11}C]MET in a strong acidic condition in the cartridge where the Cl^- brought by the homocysteine thiolactone locally decreased pH of the passing reaction solution when Na^+ was removed by cation exchange. Thus, no decrease

in radiochemical purity was observed when the Cl^- was first removed with anion exchange.

The combination of Sep-Pak Accell Plus QMA Light (OH^-) and CM (H^+) was found to afford adequate radiochemical purity and pH for an injection of [^{11}C]MET. Table 2 summarizes the results obtained for the synthesis of [^{11}C]methionine using the miniature module.

In conclusion, [^{11}C]MET was efficiently synthesized using [^{11}C]CH_3OTf on a tC18 cartridge preloaded with the aqueous solution of L-homocysteine thiolactone. The reaction solution was neutralized simply by passing through QMA Light and CM cartridges without decreasing radiochemical purity. The synthesis module for the radiosynthesis of [^{11}C]MET from [^{11}C]CH^3OTf was successfully miniaturized by assembling miniature valves and Sep-Pak cartridges and vials on a small manifold block.

References

1) Pascali C. et al., J. Label. Compd. Radiopharm. **42** (1999) 715.
2) Någren K. et al., J. Label. Compd. Radiopharm. **41** (1998) 831.

Table 1. Comparison of ion exchange cartridges for neutralizing the reaction solution.

Columns for neutralizing	pH	Radiochemical purity (%)
No cartridge	>12	97~98 %
CM Plus(H^+)	4~5	85 %
SCX (H^+)	3~5	87 %
SAX (OH^-) + CM Plus (H^+)	>10	94 %
QMA Light (OH^-) + CM Plus (H^+)	7~8	98 %

Table 2. Summary of the [^{11}C]methionine synthesis with the miniature module.

	Results
Radiochemical yield (EOS)	81%
Synthesis time	3~4 min
Radiochemical purity	>97%
pH	7~8
%Distribution of radioactivity	
Product vial	92%
tC18 cartridge	<1%
QMA cartridge	<1%
CM cartridge	<1%
Charcoal cartridge	6%

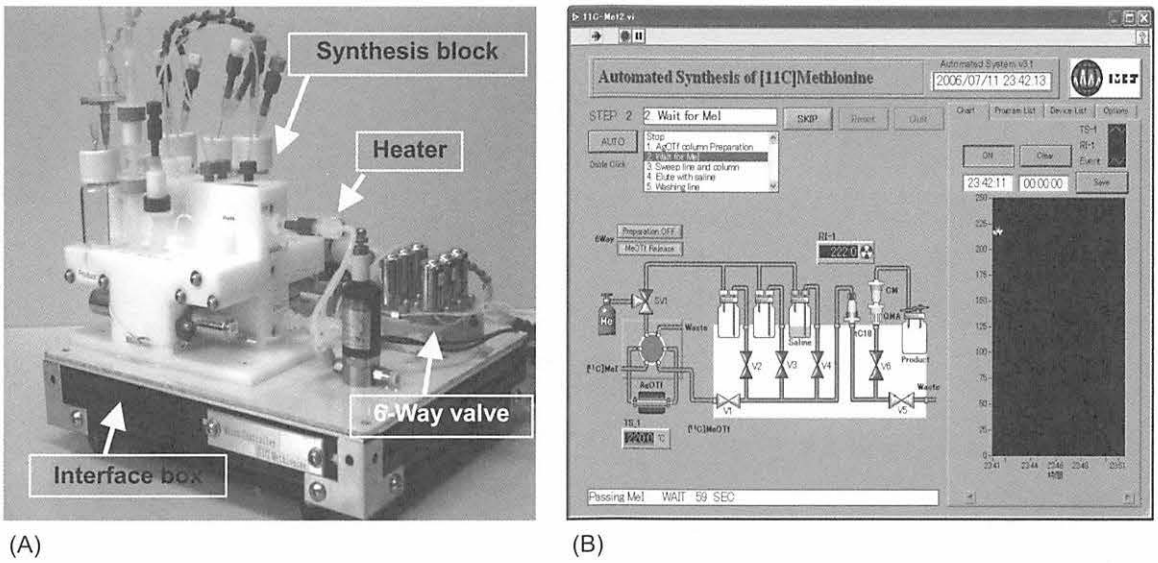

(A) (B)

Figure 1. The miniature module (A) and the LabVIEW graphical control screen on a PC monitor (B).

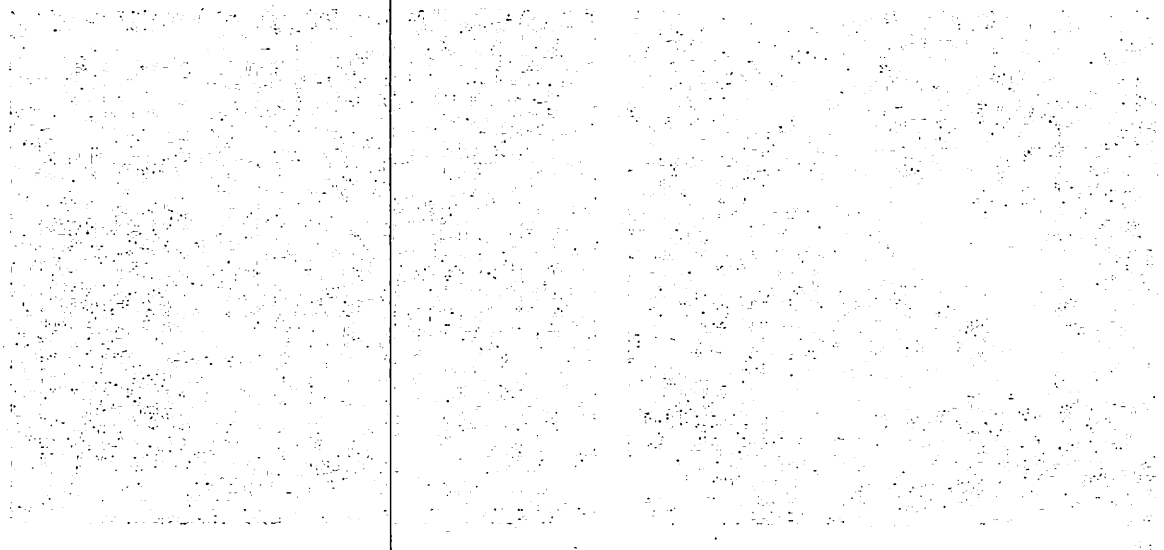

VIII. NUCLEAR MEDICINE

VIII. 1. Functional Neuroimaging of Actual Car-driving

Jeong M.[1,4], Tashiro M.[1], Singh LN.[1], Yamaguchi K.[1], Miyake M.[1], Watanuki S.[1], Fukuda F.[2], Takahashi T.[3], and Itoh M.[1]

[1]Cyclotron and Radioisotope Center, Tohoku University,
[2]Institute of Development, Aging and Cancer, Tohoku University
[3]Graduate School Program, Tohoku Gakuin University
[4]Bio-housing Research Institute, Chonnam National University Medical School

Introduction

Car-driving is a combination of complex neural tasks such as attention, perception, integration of visual and somatosensory inputs, generation of motor outputs and action controls. All drivers might sometimes encounter potentially-dangerous situations induced by cognitive and psychomotor deficits due to aging and neurological disorders[1)], alcohol and other sedative drugs[2)], and mobile phone use[3)], etc. Therefore, elucidation of the brain mechanism during car-driving is important. New findings regarding neural activities during simulated car-driving have been demonstrated, using high resolution neuroimaging techniques such as functional magnetic resonance imaging (fMRI)[4-6)] and positron emission tomography (PET)[7)]. Several investigators detected brain activations in the occipital and parietal regions bilaterally as neural substrates of simulated driving[4-7)]. However, until now, no study on actual car-driving has been conducted. Therefore, our aim was to elucidate brain activation during actual car-driving using PET and [^{18}F]2-deoxy-2-fluoro-D-glucose (FDG), that has a unique property of "metabolic trapping" where neuronal activity during 30 to 60 min post-injection can be stored[8,9)].

Methods

Thirty healthy male volunteers, all right-handed, aged 20 to 56 years old, participated in the present study. All the subjects had held a driving license for at least 6 months. The study protocol was approved by Clinical Research and Ethics Committee of Tohoku University Graduate School of Medicine. Each subject provided a written informed consent for participation to the study after receiving sufficient explanation.

The subjects were divided into the following 3 groups: (1) the active driving group (n=10; mean age ± S.D.: 35.8 ± 12.2 y.o.) who drove on an ordinary road; (2) the passive driving group (n=10; mean age: 34.8 ± 13.1 y.o.) who remained seated on a front passenger seat during the driving experiment; and (3) the subjects belonging to the control group (n=10; mean age: 32.7 ± 9.6 y.o.) who remained seated on a comfortable chair in a laboratory building, looking outside of the windows. All subjects were kept in fasting state for at least 5 hours before the study.

The subjects of the active driving group were requested to start driving a testing car, with automatic transmission, shortly after intravenous injection of FDG. They were requested to keep driving for 30 min at an approximate speed of 40 km/h along a quiet driving route around Tohoku University Aoba-yama Campus. The active-driving subjects were not informed of the details of the driving route in advance, and at each square they followed the directions of an investigator sitting on the rear seat. The passive-driving subjects followed the same protocol except for the point that they were sitting on the front passenger seat simply looking at the landscape ahead of the car throughout the driving experiment. The control subjects were sitting on a soft chair similar to that of the testing car for 30 min simply looking at the landscape outside and with their ears unplugged so that they could hear normal conversation around them.

PET emission scan started 45 minutes after FDG injection using an SET-2400W scanner (Shimadzu Inc., Kyoto, Japan), with spatial resolutions of 4.0, 4.0 and 4.5 mm at full-width-half-maximum (FWHM) in radial, tangential and axial directions, respectively. The subjects' heads were fixed gently to the head-holder with a plastic spacer inflated with air to minimize the subjects' head movement. The mean radiological dose given to the subjects was 40.7 ± 7.4 MBq (1.1 ± 0.2 mCi). Three-dimensional emission scan was performed for 5 min and post-injection transmission scan was performed for 8 min using a $^{68}Ge/^{68}Ga$ external rotating line source for tissue attenuation correction. PET image data were transferred to a supercomputer at the Synergy Center, Tohoku University, for reconstruction into 128×128×63 matrices based on a filtered back-projection algorithm using the Colsher Filter with an 8 mm cut-off frequency[10]. Driving-related brain activation was examined using Statistical Parametric Mapping (SPM) software package. The peak voxel-based significance of statistics was set at $p< 0.001$ ($Z > 3.18$) without corrections for multiple comparisons.

Results

Significant brain activations in the active driving group compared with the control were found in the visual cortices (BA17-19), primary sensorimotor (BA1-4) areas, premotor area (BA6), the parietal association area (precuneus), the cingulate gyrus (BA24), the parahippocampal gyrus (BA35) as well as in the thalamus and cerebellum (Figure 1). Brain activations in the passive driving compared with the control looked similar to those of active driving except for absence of activations in the premotor, cingulate, parahippocampal areas and in the thalamus.

Discussions

The present study is, as far as the authors know, the first study that demonstrates neural correlates of actual car-driving using a high-resolution imaging technique such as PET. For this purpose, FDG is a radiotracer of choice that may allow PET scans following completion of driving tasks. As mentioned in the introduction section, neural correlates of car-driving have been studied using a driving simulator and fMRI[4-6] or PET with $[^{15}O]H_2O$[7]. The present study demonstrated several brain activations resembling those of the previous simulated-driving studies[4,5]; namely, the primary sensorimotor areas (BA3 and 4), premotor area (BA6), visual cortex (BA17-19), medial temporal cortex (BA39), precuneus (BA7/31) and the cerebellum. The all available neuroimaging studies, including four fMRI[2,4-6] and one PET studies[7], measured brain perfusion but not brain (glucose) metabolism. The present findings are basically consistent with the previous fMRI[4,6] and PET[7] results obtained from contrasting active and passive driving conditions.

Activations in the cingulate and parahippocampal gyri were observed during active driving in the present study. Uchiyama et al., using a specific "keep-a-safe-distance" task, reported activation in the anterior cingulate, where hemodynamic responses significantly correlated to task performance[6]. These findings suggest that actual driving is more-strongly associated with the cingulate activation since actual drivers must always be careful in keeping safe distances not only to preceding cars but also to pedestrians and guardrails etc. The activation in the parahippocampal gyrus seems to be also associated with attention and cognition during actual driving.

In summary, the actual driving experiment demonstrated similar findings to those of simulated driving in spite of several differences in methodologies and protocols[4,6,7], and the results suggested that visual perception and visuomotor coordination were the main brain

functions while actual driving as well. As for autonomic responses, however, it seems there is a significant difference between simulated and actual driving conditions possibly due to absence/presence of possible risk of actual accidents. It seems that perceptive and visuomotor components can be studied by simulation, but other components of autonomic and emotional responses should be studied using actual driving, or at least a highly-sophisticated driving simulator that can imitate vibration and acceleration, etc. For drawing a definitive conclusion, the authors should indicate the importance of future replication where the same subjects undergo both actual and simulated driving using the same protocol.

References

1) Ott B.R., Heindel W.C., Whelihan W.M., et al., Dement Geriatr. Cogn. Disord. **11** (2000) 153.
2) Calhoun V.D., Pekar J.J., Pearlson G.D., et al., Neuropsychopharmacology.**29** (2004) 2097.
3) Tashiro M., Horikawa E., Mochizuki H., et al., Hum. Psychopharmacol. **20** (2005) 501.
4) Walter H., Vetter S.C., Grothe J., et al., Neuroreport. **12** (2001) 1763.
5) Calhoun V.D., Pekar J.J., McGinty V.B., et al., Hum. Brain Mapp. **16** (2002) 158.
6) Uchiyama Y., Ebe K., Kozato A., et al., Neurosci. Lett. **352** (2003) 199.
7) Horikawa E., Okamura N., Tashiro M., et al., Brain Cogn. **58** (2005) 166.
8) Fujimoto T., Itoh M., Kumano H., et al., Lancet. **348** (1999) 266.
9) Tashiro M., Itoh M., Fujimoto T., et al., J. Sports Med. Phys. Fitness. **41** (2001) 11.
10) Fujiwara T., Watanuki S., Yamamoto S., et al., Ann. Nucl. Med. **11** (1997) 307.

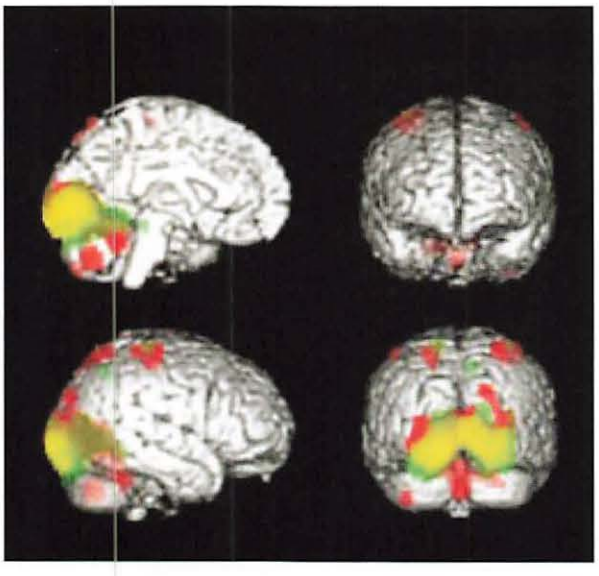

Figure 1. The main effect of car-driving was tested by inter-group comparison of the active (red) or passive (green) driving groups (n=10 for each) to the control group (n=10). Regions of common activation in the both groups are denoted in yellow color. The statistical threshold: $p < 0.001$ (uncorrected).

VIII. 2. Functional Neuroimaging of Autonomic Nervous Responses During Aroma-therapy Using [^{18}F]FDG PET

Duan X.[1], Tashiro M.[1], Wu D.[2], Yambe T.[3], Wang Q.[3], Sasaki T.[1], Kumagai K.[1], Luo Y.[3], Nitta S.[4], and Itoh M.[1]

[1]*Cyclotron and Radioisotope Center, Tohoku University*
[2]*Division of Music Education, Miyagi University of Education*
[3]*Institute of Development, Aging and Cancer, Tohoku University*
[4]*Biomedical Engineering Research Organization, Tohoku University*

Introduction

It is well known that olfactory stimulus has a powerful influence on mammalian behaviors and physiological functions, and the relationship between olfactory sensation and autonomic changes has been studied extensively. Various smells can induce autonomic changes compatible with autonomic relaxation[1,2] or excitation[3,4], as well as changes compatible with basic emotions[5]. Such autonomic changes following treatments with perfumed fragrances (aroma-therapy) can be detected by power spectral analysis (PSA) of heart rate variability (HRV). A few studies have demonstrated usefulness of HRV measurement for evaluation of autonomic changes induced by various odorants such as lavender[6,7]. It has been said that "lavender", one of the most popular flower fragrances used in aroma-therapy, usually does not induce strong emotions but does comfortable feeling and relaxation. The effects of these fragrances on brain functions do not seem to be simple. It is expected that many brain regions, including sensory and limbic regions, are involved in olfaction. So far, positron emission tomography (PET) and functional magnetic resonance imaging (fMRI) have been used to investigate regional brain activation due to various sensory and emotional stimuli. However, functional neuroanatomy of autonomic changes induced by aroma-therapy has not been studied well using PET. The aim of the present study is to investigate the effects of lavender fragrance on autonomic nervous functions in terms of HRV and to observe brain responses in terms of brain glucose metabolic changes measured by PET.

Methods

Ten healthy female volunteers, ranging 20 to 27 years old (mean age ± S.D.: 23±3.0 years old), were recruited for the present experiment after obtaining their written informed consent. The present study protocol was approved by the Ethics Committee of Tohoku University Graduate School of Medicine. Before starting the study, each subject was interviewed for her preferences to the lavender fragrance, and was also requested to rate her own stress using the Stress Response Scale (SRS-18). The subjects were requested to be seated on a comfortable chair with the eyes open in the PET operation room. Holter ECG recording in the NASA leads (FM-300, Fukuda Denshi, Tokyo, Japan) was performed for evaluation of the HRV. Respiratory rate was also monitored in order to ensure the absence of respiratory changes after lavender administration, but the data were lost because of technical problem. Then, the respiratory data were collected again from other 15 subjects (ranging 20 to 23 years old; mean age +/- S.D.: 21.0 +/- 1.0 years old).

To supply the lavender fragrance, a plaster prepared for aroma-therapy ("Lavender girl", Teikoku Pharmaceuticals, Tokyo, Japan) was attached on the subjects' right shoulder shortly before administration of [^{18}F]labeled fluorodeoxyglucose (FDG) injected through the right cubital vein (37 MBq). After 40-min-long uptake phase of FDG, all the electrodes and the lavender plaster were removed and soon PET scanning procedure was initiated using SET2400W scanner (Shimadzu Inc., Kyoto, Japan). Subjects were requested to rate their own stress again using was also requested to rate her own stress using SRS-18 after PET scanning. PET brain images were analyzed to identify regional changes of glucose metabolic rate using Statistical Parametric Mapping (SPM2[10,11]). The threshold for the significance was set at $p< 0.001$ without corrections for multiple comparisons.

Analyzing HRV in the frequency domain is a valuable method to determine quantitatively the sympathetic and parasympathetic modulations of heart rate (HR)[8,9]. Two main spectral components are most commonly distinguished in the HRV spectrum: low frequency (LF: 0.04 to 0.15 Hz) and high frequency (HF: 0.15 to 0.4 Hz) components, respectively[8,9]. For further evaluation, normalized LF and HF (nLF and nHF, respectively) and low-high frequency ratio (LF/HF) were used.

Results

Representative data of HRV measurement taken from a subject are demonstrated in Fig. 1. R-R intervals tended to be longer later in the experiment compared to the initial resting condition. The R-R intervals were somewhat shorter in the lavender

resting condition. The R-R intervals were somewhat shorter in the lavender administration condition in comparison to the control. The fraction of HF was higher and the LF/HF ratio was lower in the lavender condition. nHF tended to increase and nLF tended to decrease in the first 10 min following lavender plaster administration, resulting in decreased LF/HF.

PET analysis revealed changes in cerebral metabolism between the conditions ($p < 0.001$). Administration of lavender administration was associated with activation in the orbitofrontal cortex, posterior cingulate cortex, brainstem (mainly pons), thalamus and cerebellum while deactivation was observed mainly in the pre/post-central gyrus and frontal eye field (Fig.1).

Discussion

So far, psychological and physiological effects of various odorants have been investigated, and it has been reported that lavender elicited mostly "relaxation" and "happiness"[12]. In the present study, spectral analysis of HRV indicated a significant increase in HF component and reduction in LF/HF ratios during the lavender use. The present results go in accordance with the previous study by Saeki and colleagues[6] where 10 healthy female subjects were studied. They demonstrated that lavender fragrance induced HRV changes associated with relaxation. Kuroda and colleagues[7] conducted a study using 12 subjects to find the similar results to those by Saeki et al.

It was expected that various olfactory regions, including the primary olfactory cortex and the most limbic regions, would be activated. A previous fMRI study demonstrated activation of these regions induced by olfactory stimulations[17]. A similar study was conducted using PET as well[18]. Another fMRI study demonstrated that the pleasant smell activated the medial part of orbitofrontal cortex and the unpleasant smell did the lateral part, respectively[19]. Metabolic reduction in the olfactory regions was reported in patients with disturbed olfaction[20].

Contrary to the authors' expectation, the present study did not find involvement of any primary olfactory regions but involvement of a few association regions such as the orbitofrontal cortex, thalamus and cerebellum. A possible explanation for this discrepancy may be the difference of time window because of methodological difference. FDG accumulation in the brain tissue is a rather slow process while olfaction is a relatively instantaneous phenomenon. Since the FDG PET method tends to average brain activities of longer time span (approximately 30 to 40 min), it does not detect brain responses which

may last temporally. Therefore, it seems that an interpretation of the present results should be done based on the concept of "identifying brain regions influenced by environmental changes due to lavender fragrance lasting 40 minutes" that would make the interpretation easier.

Based on such a standpoint, lack of activation in the anterior cingulate gyrus in the present study would be reasonable because this region is regarded as one of the centers of sympathetic nervous activities that were possibly suppressed after lavender administration. Metabolic increase in the brainstem and posterior cingulate gyrus, though not usually included in the olfactory regions, seems to be associated with improved mental functions during relaxation rather than olfaction itself. The combined finding of a reduced sensorimotor activity and an improved arousal/cognitive function seem to be a good brain representation of "physical relaxation" and "improved mental functions" induced by lavender, as recognized as a calming or relaxing agent[21].

In summary, the authors have demonstrated that lavender fragrance can promote relaxation by depressing sympathetic activity while augmenting parasympathetic activity in normal adults. Our findings suggest a possible use of lavender fragrance to treat patients with various types of autonomic dysfunctions.

References

1) Alaoui-Ismaili O., Vernet-Maury E., Dittmar A., et al., Chem Senses **22** (1997) 237.
2) Nagai M., Wada M., Usui N., et al., Neurosci. Lett. **289** (2000) 227.
3) Brauchli P., Ruegg P.B., Etzweiler F., et al., Chem. Senses **20** (1995) 505.
4) Alaoui-Ismaili O., Vernet-Maury E., Dittmar A., et al., Chem. Senses **22** (1997) 237.
5) Vernet-Maury E., Alaoui-Ismaili O., Dittmar A., et al., J. Auton. Nerv. Syst. **75** (1999) 176.
6) Saeki Y., Complement Ther Med. **8** (2000) 2.
7) Kuroda K., Inoue N., Ito Y., et al., Eur. J. Appl. Physiol. **95** (2005) 107.
8) Novak V., Saul J.P., Eckberg D.L., et al., Circulation **96** (1997) 1056.
9) La Rovere MT., Bigger JT Jr., Marcus FI., et al., Lancet **351** (1998) 478.
10) Friston K., Ashburner J., Frith C., et al., Human Brain Map. **2** (1995) 165.
11) Friston K.J., Holmes A., Poline J.B., et al., Neuroimage **4** (1996) 223.
12) Vernet-Maury E., Alaoui-Ismaili O., Dittmar A., et al., J. Auton. Nerv. Syst. **75** (1999) 176.
13) Pomeranz B., Macaulay R.J., Caudill M.A., et al., Am. J. Physiol. **248** (1985) 151.
14) Malliani A., Lombardi F., Pagani M., Br. Heart J. **71** (1994) 1.
15) Dunn C., Sleep J., Collett D., et al., J. Advanced Nursing **21** (1995) 34.
16) Stevensen C.J., Complementary Therapies in Med. **2** (1994) 27.
17) de Araujo I.E., Rolls E.T., Kringelbach M.L., et al., Eur. J. Neurosci. **18** (2003) 2059.
18) Qureshy A., Kawashima R., Imran M.B., et al., J. Neurophysmol. **84** (2000) 1656.
19) Rolls E.T., Kringelbach M.L., de Araujo I.E., Eur. J. Neurosci. **26** (2002) 695.
20) Levy L.M., Henkin R.I., Lin C.S., Finley A., J. Comput. Assist. Tomogr. **23** (1999) 767.
21) Buchbauer G., Jirovetz L., Jager W., et al., J. Biosciences **46** (1991) 1067.

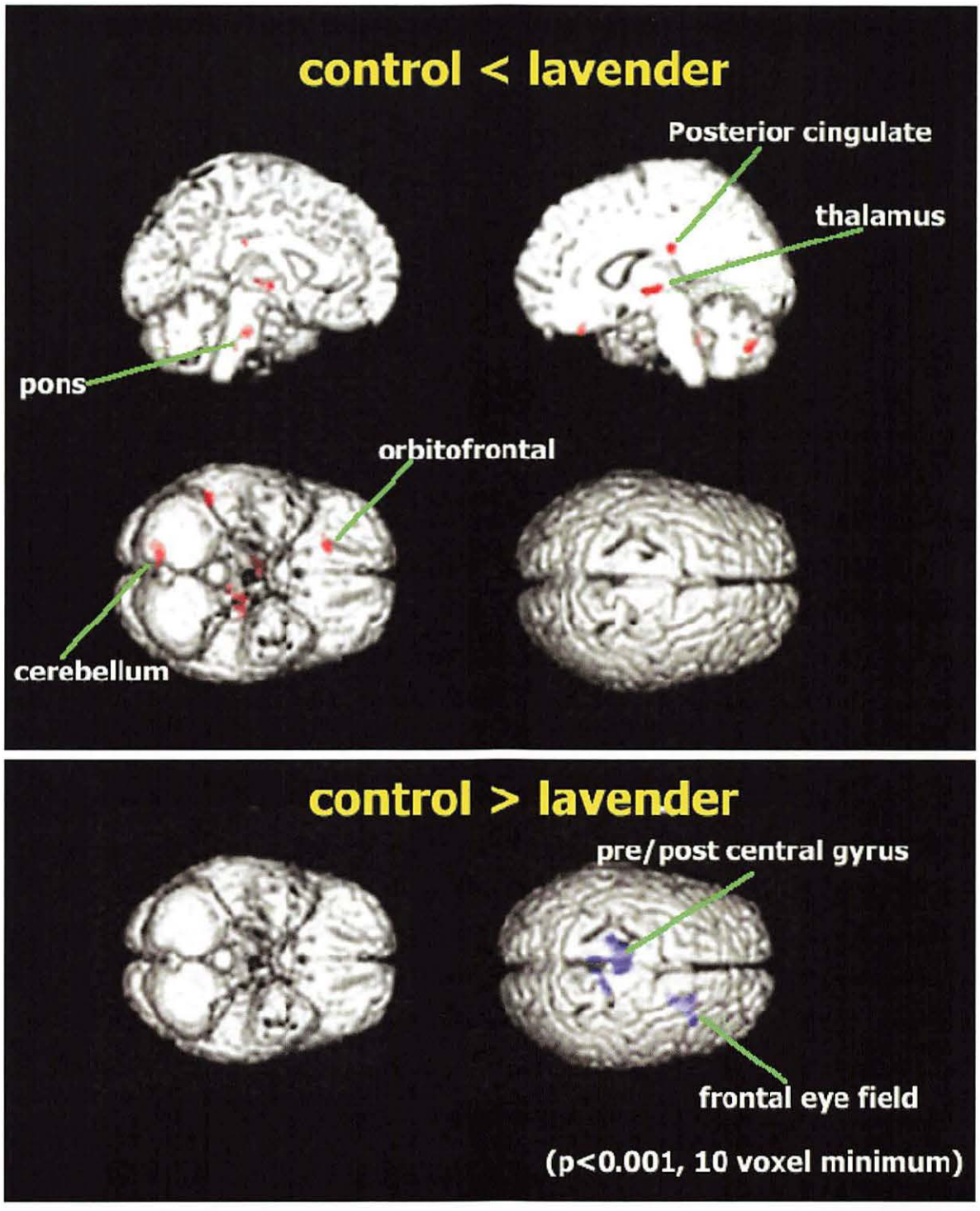

Figure 1. Results of voxel-by-voxel comparison of brain glucose metabolic images. Brain regions with metabolic increase due to lavender administration (control<lavender). And brain regions with metabolic reduction due to lavender administration (control>lavender). ($p<0.001$, 10 voxel minimum).

VIII. 3. Brain Histamine H_1 Receptor Occupancy of Antihistamines, Bepotastine and Diphenhydramine, Measured by [^{11}C]Doxepin PET

Duan X.[1], Tashiro M.[1], Kato M.[2], Miyake M.[1], Watanuki S.[1], Ishikawa S.[1], Funaki Y.[1], Iwata R.[1], Itoh M.[1], and Yanai. K.[1,2]

[1]*Cyclotron and Radioisotope Center, Tohoku University*
[2]*Graduate School of Medicine, Tohoku University*

Introduction

Histamine H1 receptor (H1R) antagonists, or antihistamines, are often used for treatment of allergic disorders such as seasonal rhinitis. Antihistamines mainly act on the peripheral tissues but can induce sedation. This undesirable central side effect is caused by blockade of nerve transmission in the histaminergic neuron system which projects from the tuberomammillary nucleus in the posterior hypothalamus to almost all cortical areas[1-3]. First-generation antihistamines, such as diphenhydramine and d-chlorpheniramine, that can easily penetrate blood-brain barrier (BBB) tend to occupy a large proportion of post-synaptic H1Rs[4-6]. Second-generation antihistamines, such as fexofenadine, cetirizine and olopatadine, can slightly penetrate BBB and H1Rs are slightly occupied as having been demonstrated using positron emission tomography (PET)[4,7-9]. Variation in cerebral H1R occupancy (H1RO) of antihistamines results mainly from their different BBB permeability. Thus, sedative property of antihistamines can be evaluated in terms of H1RO measured with PET and [^{11}C]doxepin, a radiopharmaceutical that specifically binds to H1Rs.

Methods

The present study was approved by the Committee on Clinical Investigation at Tohoku University Graduate School of Medicine, Japan, and was performed in accordance with the policy of the Declaration of Helsinki. All experiments were performed at the Cyclotron and Radioisotope Centre, Tohoku University. Eight healthy male volunteers (mean age +/- s.d.: 24.4 +/- 3.3 years old) were studied after single oral administration of bepotastine 10 mg, diphenhydramine 30 mg or placebo, using PET with [^{11}C]doxepin in a crossover study-design. Binding potential ratio and H1R occupancy values were

calculated using placebo data, and were compared between bepotastine and diphenhydramine. PET brain images, after being corrected for tissue attenuation, were reconstructed with a filtered back projection algorithm. The brain images were then normalized by plasma radioactivity at 10 min post-injection to yield static distribution volume (DV) images according to our static scan protocol reported previously[10].

For visualization at a whole-brain level, DV brain images were analyzed statistically on a voxel-by-voxel basis by Statistical Parametric Mapping (SPM2). Differences in parameter values between bepotastine, diphenhydramine and placebo (control) were statistically examined, and regional maxima of statistical significance ($p< 0.001$) were projected onto the surface-rendered MRI-T1 standard brain images.

Results

Brain images following administration of bepotastine demonstrated slightly lower binding potential in comparison to those following placebo, and images following diphenhydramine administration demonstrated significantly lower binding potential in comparison to both placebo and bepotastine (Figure 1). Using SPM2 on a voxel-by-voxel basis, parametric brain BPR images following treatment with bepotastine or diphenhydramine were statistically compared to those following treatment with placebo. Areas such as ACC, MPFC and DLPFC, TC demonstrated significantly low BPRs after treatment with diphenhydramine as compared to treatment with placebo. On the other hand, SPM analysis did not reveal any brain area where BPRs were significantly lower following treatment with bepotastine than following treatment with placebo. Overall cortical mean H1RO of bepotastine and diphenhydramine were 14.8% and 56.8%, respectively. H1R occupancy of both bepotastine and diphenhydramine correlated well with their respective drug plasma concentration ($p< 0.001$).

Discussion

Human molecular imaging, especially a non-invasive imaging of biological phenomena at a molecular level in living human brain, has been actively conducted. In the present study, H1RO of bepotastine, a second-generation antihistamine, was compared to that of diphenhydramine, a typical sedative antihistamine, in a single-blinded placebo-controlled crossover study-design. H1RO after a single oral administration of bepotastine 10 mg or diphenhydramine 30 mg was calculated as approximately 14.8% and

56.8%, respectively. It has also been reported that, single-oral administration of d-chlorpheniramine (2 mg) achieved approximately 50 to 77% of H1RO[4,8]. As a whole, previous PET studies demonstrated that first-generation antihistamines occupied more than 50% of available H1Rs.

On the other hand, H1RO after single-oral administration of bepotastine (5 mg) was much lower than that of first-generation antihistamines (15% vs. 50%). This result is in accordance with the categorization of bepotastine as a second-generation antihistamine. Previous studies have demonstrated H1ROs due to other second-generation antihistamines: epinastine 20 mg (8.2 to 13.2%)[5,6], terfenadine 60 mg (12.1-17.1%)[4,6], astemizole 10 mg (28.7%), azelastine 1 mg (20.3%), mequitazine 3 mg (22.2%)[6] and ebastine 10 mg (9.9%)[6]. As a whole, second-generation antihistamines would occupy around 0 to 20% of brain H1Rs[6]. Later, single-oral doses of cetirizine 20 mg and fexofenadine 120 mg, both double oral doses in Japan, were reported to achieve 26% and 0%, respectively[6]. Based on such findings, second-generation antihistamines can be further separated into two subgroups according to their BBB permeability[2,3]; a category that cause little sedation at low doses, but cause dose-related cognitive impairment at higher doses as seen with cetirizine, and the other category that does not cross BBB and therefore induces no sedation even at exceeded doses as seen with fexofenadine[9].

The reasons for the small number of placebo-controlled crossover studies would be their disadvantages such as increased radiological exposure to subjects as the same subject is scanned more than twice. Investigators are therefore advised to minimize total radiation exposure to subjects by choosing a minimum radiological dose and by using 3D data acquisition mode with high sensitivity. In addition, mental and physical stress of the subjects should be reduced by simplifying measurement protocol, as in the present study where complete dataset were obtained for all of the eight subjects. In a previous study, only 6 of the 11 subjects completed all of the four 100-min-long PET scans planned, possibly suggesting how hard it is to conduct crossover PET studies[11].

In summary, we examined H1RO of bepotastine at its recommended single oral dose (10 mg) and compared it to that of single oral administration of diphenhydramine (30 mg) using PET measurement in a placebo-controlled crossover study. Bepotastine occupied approximately 15% of available H1Rs in human brain while approximately 57% of H1Rs were occupied by 30 mg of diphenhydramine. It is therefore suggested that oral administration of bepotastine (10 mg), with its low H1RO and thus minimal sedation, could safely be used an anti-allergic treatment for various allergic disorders. It would be of a

great benefit to estimate the appropriate therapeutic doses of new antihistamines and other drugs using PET measurement and the smallest number of volunteers[6-10]. Collection of more H1RO data is encouraged for establishment of a reliable international database for evaluation of the sedative profile of antihistamines.

References

1) Haas H., Panula P., Nat. Rev. Neurosci. **4** (2003) 121.
2) Holgate S.T., Canonica G.W., Simons F.E., et al., Clin Exp Allergy. **33** (2003) 1305.
3) Casale T.B., Blaiss M.S., Gelfand E., et al., J. Allergy Clin. Immunol. **111** (2003) 835.
4) Yanai K., Ryu J.H., Watanabe T., et al., Br. J. Pharmacol. **116** (1995) 1649.
5) Yanai K., Ryu J.H., Watanabe T., et al., Methods Find Exp. Clin. Pharmacol. **17** (1995) 64.
6) Yanai K., Okamura N., Tagawa M., et al., Clin. Exp. Allergy. **29** (1999) 29.
7) Okamura N., Yanai K., Higuchi M., et al., Br. J. Pharmacol. **129** (2000) 115.
8) Tagawa M., Kano M., Okamura N., et al., Br. J. Clin. Pharmacol. **52** (2001) 501.
9) Tashiro M., Sakurada Y., Iwabuchi K., et al., J. Clin. Pharmacol. **44** (2004) 890.
10) Mochizuki H., Kimura Y., Ishii K., et al., Nucl. Med. Biol. **31** (2004) 1005.
11) Martinez D., Hwang D., Mawlawi O., et al., Neuropsychopharmacology **24** (2001) 209.

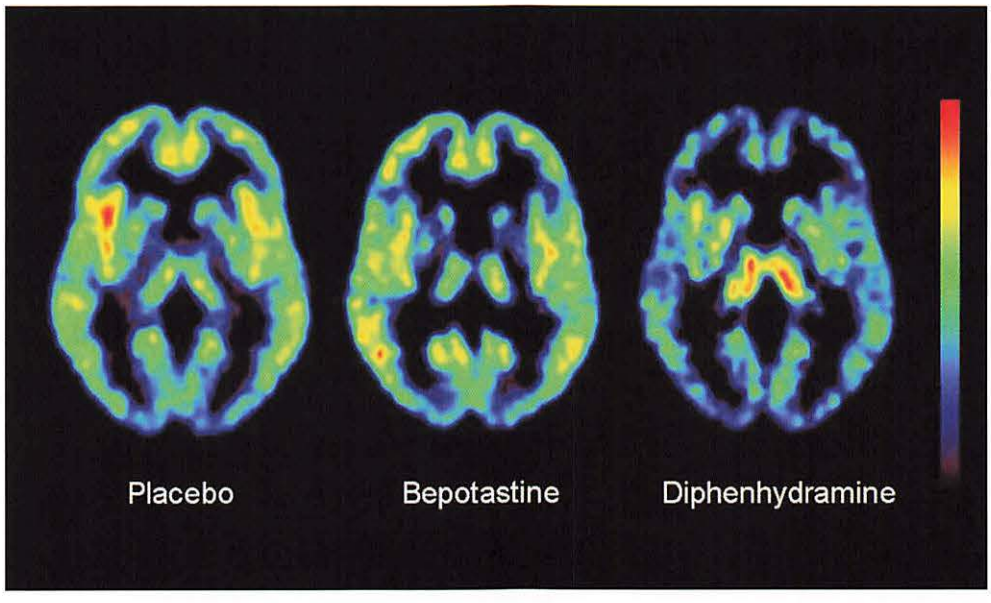

Figure 1. Mean brain images of healthy volunteers after administration of placebo, bepotastine and diphenhydramine.

VIII. 4. Whole Body Metabolic Imaging for Sport Science

Masud M.[1], Fujimoto T.[2], Tashiro M.[1], Watanuki S.[1], Miyake M.[1], Iwata R.[1], and Itoh M.[1]

[1]Cyclotron Radioisotope Center, Tohoku University
[2]Center for the Advancement of Higher Education,

[^{18}F]Fluorodeoxy-glucose (^{18}FDG) and three dimensional positron emission tomography (3DPET) is a useful device for clinical and basic medicine that maps physiopathology of organs *in vivo* in humans. ^{18}FDG-3DPET technique assesses the changes in the muscle usage as well as physiology of organs during tasks. Imaging analysis of muscle use difference between trained and non-trained subjects would be helpful for rational body training of future athletes. Inevitably, brain is a vital organ which has a keen participation at physical task evaluated by PET technique. We propose the use of 3DPET for sport science.

Measurement of whole body glucose metabolism for sport science

PET technique assesses the metabolic activity of organs in humans *in vivo* at rest or during task[1-5]. Figure 1 depicts the whole-body ^{18}FDG distribution at one hour after injection while the person was in resting state. The highest uptake is seen in the brain than other organs. During exercise, jogging in this case, ^{18}FDG uptake is dramatically increased in the lower limbs. In this experiment, the subject ran around our university campus for a total of 35 minutes, 15 minutes prior and 20 minutes after the intravenous injection of ^{18}FDG. A group study using seven healthy male volunteers, average age of 32.2 ± 13.5 y (mean±SD) showed redistribution of energy metabolism, i.e., the highest in lower leg muscles while ^{18}FDG uptake was reduced in other organs except in the brain and heart (Fig. 2). Whole-body PET imaging was carried out by a series of 9 to 11 scanning table movements taking 180 sec for each table position. A transmission scan (post injection transmission mode) then followed using the same time schedule as the emission scan using a ^{68}Ge/^{68}Ga external rotating line source to correct tissue photon attenuations for the emission scans. The exercise strength was below the anaerobic threshold and kept

constant (140 to 150 beat/min,) using heart rate as a marker, which was monitored by a wrist pulse monitor (Vantage-XL Polar Electro, Finland). Plasma glucose level was within normal range (103 ± 9.7 mg/dl, mean ± SD), and did not show any change between the beginning and end of the experiment.

ROIs analysis showed that ^{18}FDG uptake by the skeletal muscles of legs increased two folds while abdominal organs, such as the kidneys, liver, and intestines showed reduction in ^{18}FDG uptakes during running compared with the controls as shown in Fig. 2 and Fig. 3. These results clearly show the homeostatic control of energy resources, i.e., glucose was sent to the working skeletal muscles from abdominal organs.

Exercise inducing energy metabolism between trained and non-trained subjects

Training integrates and adjusts the skeletal muscle physiology from homogeneous perfusion distributions within muscles[6]. Although PET has limited time resolution, it can visualize the relative work of all the body muscles utilized in a particular exercise. An example is shown for this evaluation. Two subjects collaborated in this experiment, one is a beginner and the other is a proficient golf player with a handicap of zero. They continuously practiced a total of 240 shots, at the rate of 6 shots/min for 40 minutes with a driver after 40 MBq of ^{18}FDG administration. ^{18}FDG uptake of the proficient golfer was much higher than that of the beginner, except in the brain. The difference was mostly noted in the forearms, hands and leg muscles. Accumulation of ^{18}FDG uptake was more prominent in the posterior compartment of both the legs and the trunk than in the anterior compartment (Fig. 4). These asymmetrical distributions are reasonable since the role of the posterior compartment muscles of the legs is to support the body against gravity, and simultaneously transmit the force of reaction from the ground to the upper part of the body. In case of the beginner, the work exerted by the posterior compartment muscles was not stronger than the anterior compartment muscles. As a result, the beginner could not produce enough power to generate effective shots. This suggests the usefulness of physical training to ameliorate the tissue oxidative metabolism[7,8].

The role of the brain at physical exercise.

The brain is a vital organ that regulates the functional behaviour of rest of the body[9]. Meanwhile, brain would have a keen participation in the regulation of physical exercise. PET with certain tracers such as ^{18}FDG or ^{15}O-H2O are useful in evaluation of brain function at rest or physical exertion[10,11]. Figure 5 shows the activated brain areas during

field running using statistical parametric mapping analysis (SPM-96)[12]. The results show that the posterior parietal, occipital, premotor cortices and the cerebellum are the principal brain areas working during field running. Activation of the occipital cortex was more prominent than those of sensori-motor brain areas. This suggests that main task of the brain during running is to process visual information, while the control of the body movement itself is rather automatic and requires less attention. Indeed, the visual information processing of the external environment is crucial for runners to go forward quickly and smoothly. Another important role of the brain during running is the integration of both visual and spatial information and motor control. The parietal brain, which is known for this integration of motor control and visual information, was also active during the task.

Conclusion

High sensitivity 3DPET is a unique imaging modality to map regional whole-body energy metabolism during any task. A whole body mapping of muscle work would make the ^{18}FDG-3DPET technique suitable to create a database of famous athletes' muscle usage for future research. We propose the application of ^{18}FDG-3DPET method for sport science.

Acknowledgements.

This work was supported in part by a grant-in-aid (No.09470195 to K. Kubota and Nos. 08558082 and 08835002 to M. Itoh from the Ministry of Education, Science, Sports and Culture, Japan. This research program was also supported by the 13th Research-Aid Report in Medical Health Science of Meiji Life Foundation of Health and Welfare (to T. Fujimoto, Ph.D, and K. Ozaki, Ph.D.). The authors would like to convey special thanks to all the staffs in the Cyclotron Radioisotope center for their courageous collaborations.

References

1) Harris M.L., Julyan P., Kulkarni B., Gow D., Hobson A., Hastings D., et al., J. Cereb. Blood Flow Metab. **25** (2005) 520.
2) Buysse D.J., Nofzinger E.A., Germain A., Meltzer C.C., Wood A., Ombao H., Sleep **27** (2004) 1245.
3) Small G.W., Silverman D.H., Siddarth P., Ercoli L.M., Miller K.J., Lavretsky H., Am. J. Geriatr. Psychiatry **14** (2006) 538.
4) Willis M.W., Ketter T.A., Kimbrell T.A., George M.S., Herscovitch P., Danielson A.L., Psychiatry Res. **114** (2002): 23.
5) Youn T., Lyoo I.K., Kim J.K., Park H.J., Ha K.S., Lee D.S., Biol. Psychol. **60** (2002) 109.

6) Kalliokoski K.K., Laaksonen M.S., Knuuti J., Nuutila P., Int J Sports Med. **24** (2003) 400-3.
7) Kalliokoski K.K., Oikonen V., Takala T.O., et al., Am. J. Physiol. Endocrinol. Metab. 280 (2001) E1015.
8) Kalliokoski K.K., Knuuti J., Nuutila P., J. Appl. Physiol., **98** (2005) 380.
9) Newberg A., Cotter A., Udeshi M., Alavi A., Clark C., Clin. Nucl. Med. **28** (2003) 565.
10) Kim J.J., Kim M.S., Lee J.S., Lee D.S., Lee M.C., Kwon J.S., Neuroimage **15** (2002) 879.
11) Christensen L.O., Johannsen P., Sinkjaer T., Petersen N., Pyndt H.S., Nielsen J.B., Exp. Brain Res. **135** (2000) 66.
12) Tashiro M., Itoh M., Fujimoto T., et al., J. Sports Med. Phys. Fit. **41** (2001) 11.

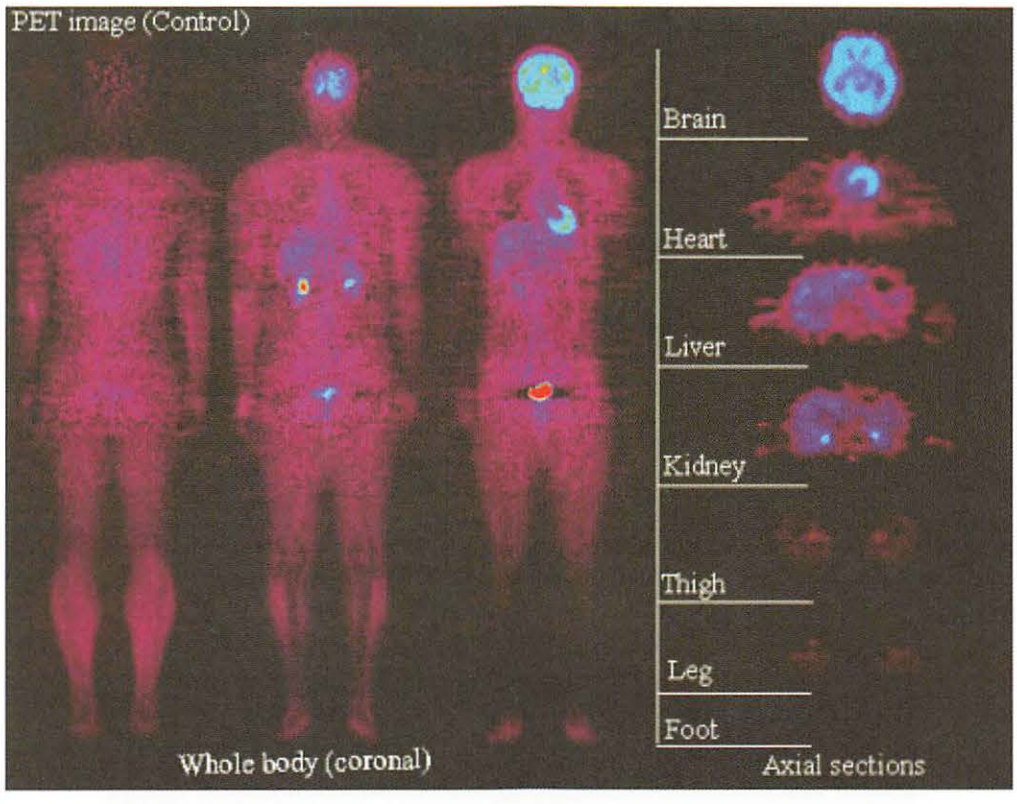

Figure 1. Whole body coronal PET images from one of the controls with representative axial images (right panel) are illustrated. Images are viewed from back (left of the figure) to the front (toward right).

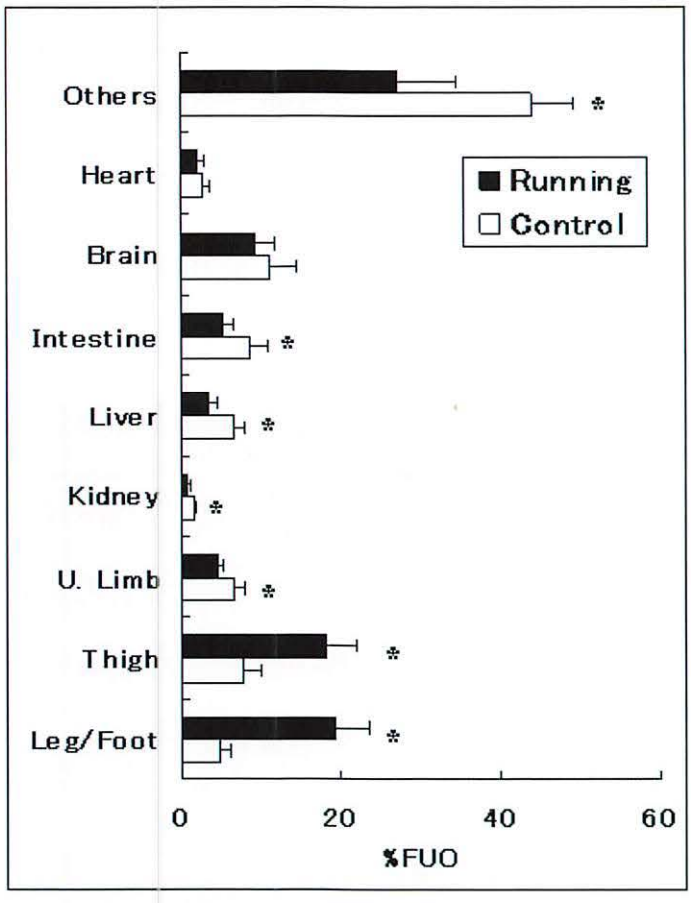

Figure 2. %FUO values of 14 male subjects as controls (N = 7) and running (N = 7) were shown as mean with their standard deviation. %FUO values presented statistically significant at *p<0.05 among control and runners.

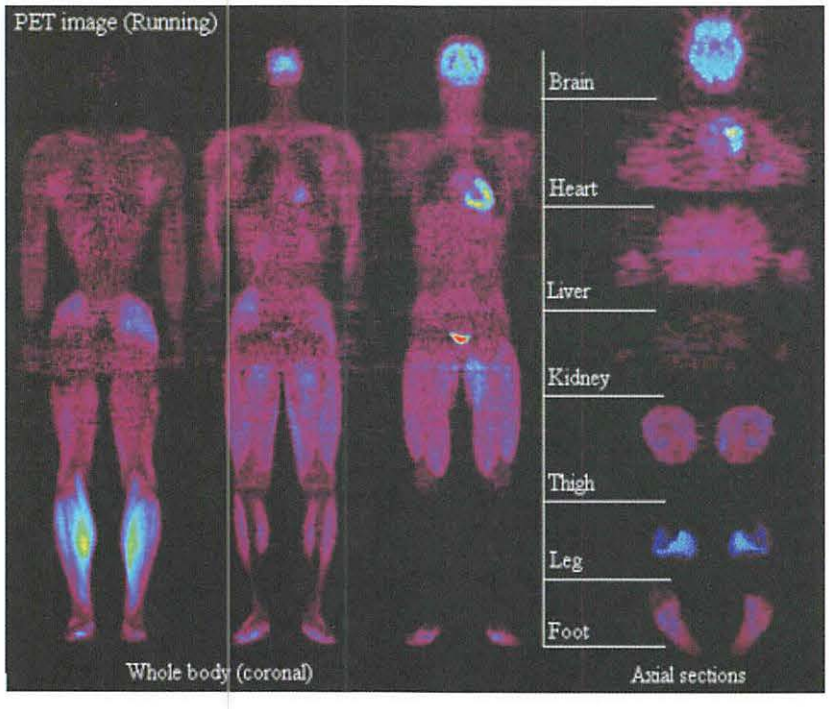

Figure 3. Whole body coronal PET image from a typical running subject with representative axial images on the right panel are illustrated. Leg/foot and thigh showed increases of ^{18}FDG uptake.

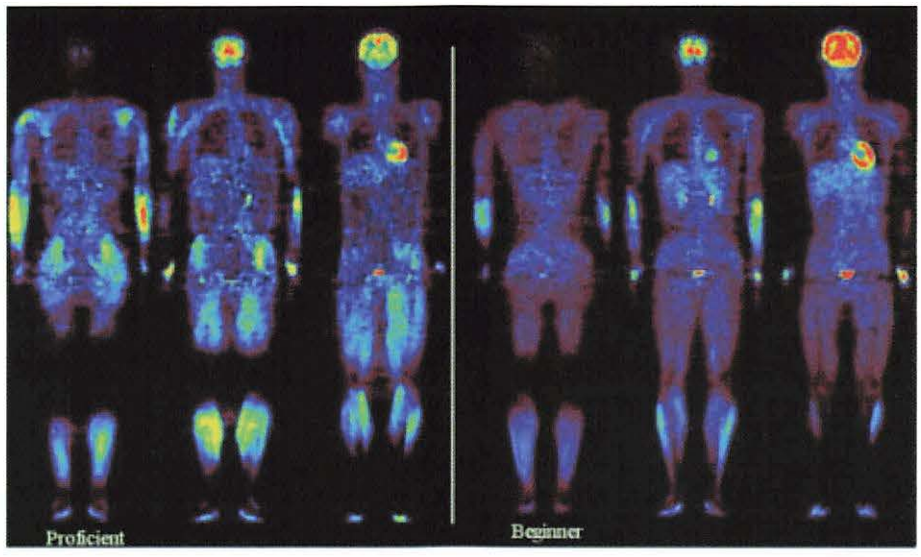

Figure 4. ^{18}FDG uptake was increased in the skeletal muscles of leg, forearm and hands in the proficient golfer.

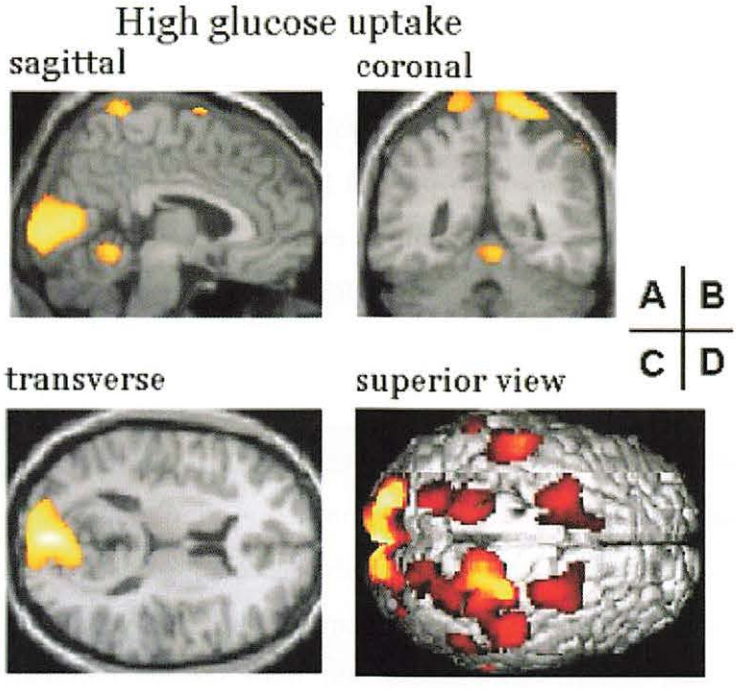

Figure 5. Regional brain ^{18}FDG uptake was statistically compared between running and control subjects, seven in each group, using a statistical parametric mapping (SPM96) software adopting a $p<0.001$ threshold. Significant activation by running was found in the posterior parietal, occipital, cortices and cerebellar vermis. The activated areas are shown over the SPM MRI Template in the sagittal (A), coronal (B), transverse (C) planes, and on rendering (D) (Tashiro et al; 99).

VIII. 5. Differential Activation of the Midbrain Periaqueductal Grey by Experience of Visceral Stimulation in Humans

Hamaguchi T.[1], Kano M.[1], Kanazawa M.[1], Rikimaru H.[2], Watanabe S.[1], Itoh M.[2], Yanai K.[1], and Fukudo S.[1]

[1]Graduate School of Medicine, Tohoku University
[2]Cyclotron Radio Isotope Center, Tohoku University

Introduction

The midbrain periaqueductal grey (PAG) plays a pivotal role in integrating the analgesic and cardiovascular responses of an animal to threat, stress or pain[1)]. The PAG is also an important site for acute opioid actions [2] and the expression of some signs of opioid withdrawal[3)]. Experience of pain minimizes immediate harm by motivating escape[4-6)]. Anticipation of pain is mechanism to prevent future harm by learning signs of impending pain[7-10)], allowing avoidance of future painful events.

Hypersensitivity to visceral stimulation is major pathophysiology of IBS[11-13,14)]. Recent advances in the neurophysiology are providing a series of plausible mechanisms to explain the development of hyperalgesia of the human gastrointestinal tract[15-17)]. However, the brain area related to initial programming of sensitization provoked by the visceral perception is still unknown. Detailed information on brain activation in the initial programming of sensitization to distention of the descending colon in humans is needed.

This study clarified that brain activation due to the colonic distention is different between with initial intense stimulation and with intense stimulation after the mild stimulation. The brain behaves differently in response to the different order of visceral stimulation. This differential brain activation to colonic distention seems to be due to summation of central processing.

Methods

Subjects

This study was approved by the Ethics Committee of Tohoku University School of Medicine. All subjects gave written informed consent. Fifteen normal volunteers (4

female, 11 male, 20-26 years old, all right-handed) participated in this study. All subjects were free from gastrointestinal disorder symptoms or signs. All subjects scored Spielberger's State and Trait Anxiety Inventory (STAI)[18] and Zung's Self-rating Depression Scale (SDS)[19] before the experiment.

On the day before examination, the subjects took a low residue diet and at night (21:00), they ingested 17 g (13.6%) of magnesium citrate, 75 mg of sodium picosulfate, and 24 mg of sennoside A & B to cleanse the colon. By using a colonoscope, a plastic tube with a thin polyethylene bag (Synectics Medical, Stockholm) was inserted into the descending colon.

PET scanning

^{15}O-Labeled water was injected into the right arm vein at the beginning of colonic distention. rCBF in each subject was measured during 4 scans (70 seconds each) using a PET scanner in three-dimension sampling mode (HEADTOME V SET-2400W, Shimadzu, Japan).

The descending colon was distended with a computerized barostat pump (Medtronics Synectics, Shoreview, MN). To clarify the sensitization process to colonic distention, orders of stimuli was set with 2 different patterns as follows: group 1: 40 - 20 (n = 8), group 2: 0 - 20 (n = 7). No subject was informed of the order or intensity of stimuli.

After each stimulation, the subjects were asked to report the following 7 items of visceral perception or emotion: abdominal discomfort, abdominal distention, abdominal pain, urgency for defecation, perceived stress, sleepiness, and anxiety. Each sensation was evaluated on an ordinate scale[20] from 0 (no sensation) to 10 (maximal sensation).

Data Analyses

PET images were analyzed using SPM2 (Wellcome, Department of Cognitive Neurology, London, UK) on a MATLAB platform (Mathworks Inc.). To estimate the neural sensitization to visceral stimulation by stimulus effect of 0, 20, and 40 mmHg distention, a conjunction analysis were made using 'multi-group, conditions and covariates' SPM model[21]. All brain images were analyzed in a conjunction analysis[21], rectified for gender difference and order effect on this analysis[22]. Ordinate visceral perception and emotion were compared between groups with Mann-Whitney U test.

Results

Visceral perception and emotional changes during equivalent stimulus in different order

Visceral perception and emotion were found no difference in equivalent stimuli depending on stimulus order of the descending colon. Abdominal discomfort ($Z = -1.56$, $p = 0.12$) and abdominal pain ($Z = -0.90$, $p = 0.37$) during 20 mmHg distention after 40 mmHg were lower than during 20 mmHg distention only (not significant, Fig. 1).

rCBF changes during equivalent colonic distention in different order

Colonic distention with 20 mmHg after the experience of 40 mmHg significantly more activated the midbrain including PAG ($Z = 4.95$), left insula (BA13, $Z = 4.93$), right putamen ($Z = 3.96$), right middle temporal gyrus ($Z = 3.94$) and cerebellum than that without prior experience of visceral stimuli (group 3 and 4) (uncorrected $p < 0.001$, Fig. 2).

rCBF changes by colonic distention

Colonic distention with 20 mmHg and 40 mmHg induced significant activation of the regional brain; right orbitofrontal gyrus (BA 11), bilateral inferior parietal gyrus (BA 40), right putamen, bilateral caudate, bilateral thalamus, and cerebellum (data not shown). These area are essentially the same brain regions of the first report in our laboratory[23]. Sham distention with 0 mmHg also induced significant activation of the right inferior parietal gyrus (BA 40) (data not shown), replicating the previous analysis with smaller sample size[23].

Basic Characteristics of Subjects

There were no difference in age and sex ratio among groups. Moreover, STAI and SDS did not differ among groups.

Discussion

By establishing a direct comparison to equivalently visceral stimulus in the different order, these data show the possibility that the modulation of visceral perception and emotion by experience of stimulation dependent on neural activity in a specific area of midbrain, insula, and cerebellum.

The PAG is an important component of the descending noxious inhibitory system[24], which contains a high concentration of opiate neurons with descending spinal

afferents[25]. One mechanism by which the PAG modulates visceral perception may involve the release of endogenous opioids. The PAG contains significant quantities of all families of endogenous opioid peptides, and it is known that μ opioids act by releasing PAG projection cells from GABAergic inhivition[26]. Specific projections of the medial network to the PAG, hypothalamus, and amygdala presumably mediate integrated autonomic and antinociceptive responses to acute aversive stimuli[24, 27]. Activation in the PAG is significantly increased during attentional modulation of pain intensity[25], and changes in pain responses attributable to changes in arousal or attention result from the action of modulatory networks that control the transmission of nociceptive signals of the brain[28]. Therefore, this study suggest that mild (20 mmHg) distention after the experience of 40 mmHg distention to the descending colon might be enough to reduce visceral sensation with activating descending pain inhibitory system in normal subjects.

In the previous study has shown in humans that a conditioning stimulus is able to modulate the perceptual and reflex response to intestinal distention[29]. In healthy human subjects and patients with IBS, repetitive distention of a balloon in the rectum or colon to noxious pressures altered the perception of colonic distention consistent with the development of hyperalgesia[14, 30]. Analogous short-term stimulation paradigms have been shown to induce central sensitization in animal models[31]. Because the development of central sensitization is modulated by endogenous pain modulation systems, including bulbospinal descending inhibitory system[32], a short-term sensitization paradigm may detect differences in the activation of these systems. Our findings indicated an adequate activation of central perceptional systems in response to preceding visceral stimuli as a possible mechanism in the etiology of altered visceral perception in functional bowel disorders.

References

1) Bandler R., Shipley M.T., Trends Neurosci. **17** (1994) 379.
2) Yaksh T.L., Yeung J.C., Rudy T.A., Brain Res. **114** (1976) 83.
3) Christie M.J., Williams J.T., Osborne P.B., Bellchambers C.E., Trends Pharmacol. Sci. **18** 1 (1997) 34.
4) Tanimoto S., Nakagawa T., Yamauchi Y., Minami,M., Satoh M., Eur. J. Neurosci. **18** (2003) 2343.
5) Harmer C.J., Thilo K.V., Rothwell J.C., Goodwin G.M., Nat. Neurosci. **4** (2001) 17.
6) Cipher D.J., Fernandez E., Behav. Res. Ther. **35** (1997) 437.
7) Rainville P., Duncan G.H., Price D.D., Carrier B., Bushnell M.C., Science **277** (1997) 968.
8) Ploghaus A., et al., Science **18** (1999) 1979.
9) Rainville P., Curr. Opin. Neurobiol. **12** (2002) 195.
10) Porro C.A., Cettolo V., Francescato M.P., Baraldi P., Neuroimage **19** (2003) 1738.
11) Fukudo S., et al., J. Gastroenterol. **37** (Suppl 14) (2002) 145.
12) Fukudo S., Nomura T., Hongo M., Gut. **42** (1998) 845.
13) Kanazawa M., Nomura T., Fukudo S., Hongo M., Neurogastroenterol. Motil. **12** (2000) 87.

14) Munakata J., et al., Gastroenterology **112** (1997) 55.
15) Kim D., et al., Science **302** (2003) 117.
16) Mayer E.A., Gebhart G.F., Gastroenterology **107** (1994) 271.
17) Mertz H., Gut. **51** (Suppl 1) (2002) 29-33.
18) Spielberger C.D., Gorsuch R.L., Lushene R.E., Vagg P.R., Jacobs G.A., Manual for the state-trait anxiety inventory STAI (From Y) (Consulting Psychologist Press, Palo Alto, CA, 1983).
19) Zung W.W., Arch. Gen. Psychiatry **12** (1965) 63.
20) Talley N., The Functional Gastrointestinal Disorders: Diagnosis, Pathophysiology, and Treatment (eds. Drossman, D. et al.), Little Brown and Company, Boston (1994) 265.
21) Price C.J., Friston K.J., Neuroimage **5** (1996) 261.
22) Friston K.J., et al., Human Brain Mapping **2** (1995) 189.
23) Hamaguchi T., et al., Neurogastroenterol. Motil. **16** (2004) 299.
24) Vogt B.A, Sikes R.W., Vogt L.J., Neurobiology of Cingulate Cortex and Limbic Thalamus (eds. Vogt, B., A & Gabriel, M.), Birkhauser, Boston (1993) 313.
25) Tracey I., et al., J. Neurosci. **22** (2002) 2748.
26) Fields H.L., Basbaum A.I., Textbook of Pain (eds. Patrick, D. W. & Ronald, M.), Churchill Livingstone, London (1999) 309.
27) Steinmetz J.E, Logue S.F., Miller D.P., Behav. Neurosci. **107** (1993) 941.
28) Petrovic P., Petersson K.M., Ghatan P.H., Stone-Elander S., Ingvar M., Pain **85** (2000) 19.
29) Serra J., Azpiroz F., Malagelada J.R., Gastroenterology **109** (1995) 1742.
30) Ness T.J., Metcalf A.M., Gebhart G.F., Pain **43** (1990) 377.
31) Traub R.J., Pechman P., Iadarola M.J., Gebhart G.F., Pain **49** (1992) 393.
32) Handwerker H., Reeh P., in Hyperalgehusia and allodynia (ed. Willis, W. J.), Raven, New York (1992) 107.

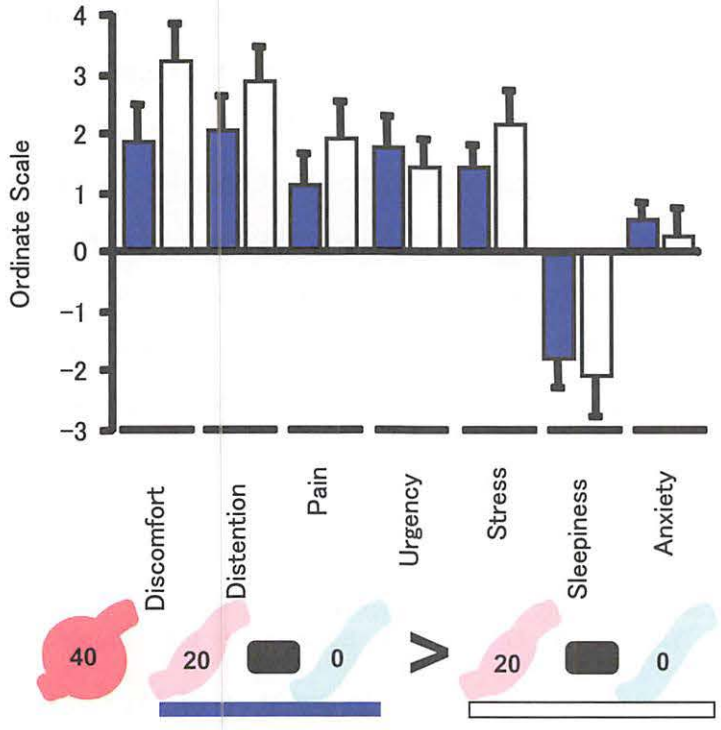

Figure 1. Comparisons of visceral perception and emotion during stimulation minus baseline. Mild (20 mmHg) stimulation after intense stimuli v.s. 20 mmHg without prior stimulation. Solid bars indicated the group 1. Open bars were group 2 (mean and standard error). Vertical axis indicated the visceral perception and emotion changes from baseline of the ordinate scale. There were no significantly differences in the ordinate scale during mild stimulation between with intense stimuli and without prior stimuli. Statistical analyses was used by Mann-Whitney U-test.

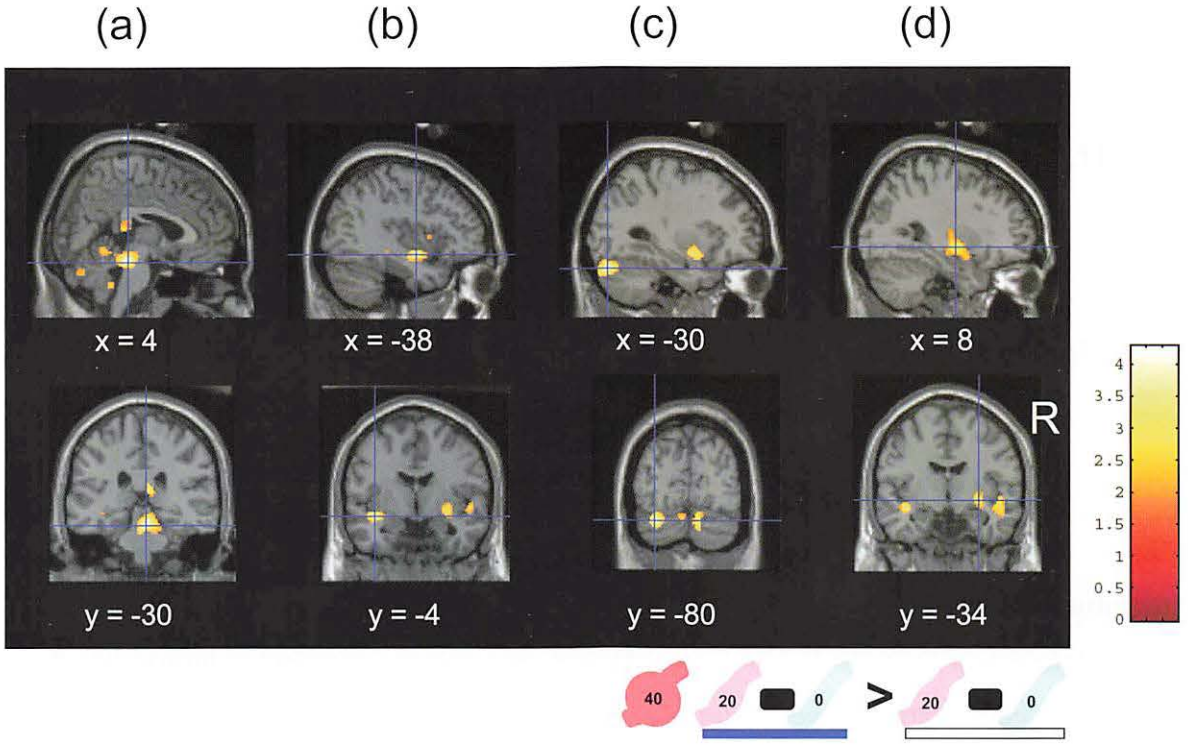

Figure 2. Statistical (Z) maps of brain during 20 mmHg stimulation compared to 20 mmHg distention after the experience of 40 mmHg distention (group 1) and 20 mmHg distention without the experience of prior stimuli (group 2). (a) Note the significant higher activation of the midbrain including PAG (x, y, z = 4, -30, -20, Z = 4.95), (b) left insula (BA13, x, y, z = -38, -4, -12, Z = 4.93), (c) left cerebellum (x, y, z = -30, -80, -26, Z = 4.74), (d) right putamen (x, y, z = 30, -8, -6, Z = 3.96). Color calibration bars that apply to each image represent critical Z-value magnitude of the activation areas. Coordinates are relative to anterior commeasure in the interaural (x), anterior-posterior (y), and superior-inferior (z) directions. Color calibration bars that apply to each image represent critical Z-value magnitude of the activation areas with a threshold voxel alpha level of $p < 0.001$ (uncorrected). R indicated right side of the brain image.

VIII. 6. Relationship between Brain Activity and Natural Killer Cell Activity in Patients with Cancer

Tashiro M.[1], Kubota K.[2], Miyake M.[1], Watanuki S.[1], Kumano K.[3], and Itoh M.[1]

[1]*Cyclotron and Radioisotope Center, Tohoku University*
[2]*Division of Nuclear Medicine and Radiology, International Medical Center of Japan*
[3]*Graduate School of Medicine, The University of Tokyo*

Introduction

Interaction between psychological factors and immune function in human has been long discussed by various investigators[1]. Since psychological factors have been discussed in association with the prognosis of cancer patients[2-5], explanation of how psychosocial factors result in certain physical outcomes would be of clinical importance. Nowadays, presence of psycho-neuro-immune (PNI) interaction seems to be doubtless, but its mechanism is still to be investigated. One of the possible main pathways that mediate this complex interaction would be the hypothalamic-pituitary-adrenal (HPA) axis. This hypothesis, however, does not say anything about the roles of higher brain including neocortex and limbic system. The cerebral cortex and limbic system should also be included in the pathway of psycho-immune interactions since psychosocial events should be first recognised and judged before they are felt "stressful". Our preliminary report already demonstrated that functional neuroimaging technique would be useful in clinical research of PNI interaction though the number of subjects were rather small (n=8)[6]. In the present report, updated results with increased number of patients are demonstrated.

Methods

Subjects were 24 patients (mean age +/- s.d., 62.5 +/- 11.5) with cancers in various organs at various stages. The study protocol was approved by the Ethics Committee for Clinical Research of Tohoku University and informed consent was obtained from each patient. After injection of [^{18}F]fluorodeoxyglucose (FDG), patients were kept under resting condition throughout uptake time and scanning periods. Details of the data acquisition and analysis are given in our previous works[7,8]. Natural killer cell activity

(NKA) was measured using a blood sample taken from each patient just prior to injection of FDG. Then, data analysis was performed to examine linear correlation between the regional cerebral glucose uptake ratios and NKA as well as intra-group differences between high and low NKA patients, using Statistical Parametric Mapping (SPM).

Results

In the present study, 8 out of 24 patients were excluded because anti-cancer treatment including chemotherapy had already started because they demonstrated significantly low NKA (mean NKA +/- S.D.: 10.2 +/- 11.4) than the NKA of the other patients (mean NKA +/- S.D.: 24.0 +/- 14.7) ($p< 0.05$). The 16 patients were further divided into two subgroups: low and high NKA groups. Group comparison analysis was performed including the age-matched controls. Brain image analysis revealed that NKA values correlated negatively in the right lateral prefrontal cortex, temporo-parietal cortex, and in the cerebellum. No brain regions demonstrated positive correlation to NKA. Intra-group comparison demonstrated that high NKA was associated with low glucose uptake in the insula and high glucose uptake in left dorsolateral prefrontal cortex (DLPFC). Intra-group comparison also demonstrated that low NKA was associated with low glucose uptake in the thalamus and hypothalamus and high glucose uptake in occipital cortex and cerebellum.

Discussions

Links between psychosocial events and immune responses have been long studied[9,10]. However, the roles of cortical and limbic structures in a psycho-immune interaction have not been discussed into deep yet. Previous animal studies demonstrated that altered immune functions were observed following destruction of specific brain structures such as cerebral cortex, limbic structure and hypothalamus. Immune enhancement tends to follow damages to the limbic structures, suppression tends to follow damages to the cerebral cortex, and both enhancement and suppression were observed following damages to the hypothalamus[11]. The purpose of these lesioning studies was to clarify the role of specific brain regions in the neuro-immune modulation. Human studies in the same context could be achieved only with the aid of non-invasive functional imaging such as PET.

Previous works done by Wik and colleagues demonstrated correlation between the

regional cerebral blood flow (rCBF) and NKA in normal volunteers and patients with fibromyalgia[12,13]. Their studies demonstrated that NKA correlated negatively with rCBF in the somatosensory association cortex. These studies, as far as the authors know, the first studies that examined natural immunity and regional brain activity in human subjects. The findings of negative correlation between NKA and activity in the limbic structures seems to be in accordance with the previous animal studies[11].

In addition, chemotherapy might affect not only NKA but also regional brain activity. In one of our previous studies where FDG PET was performed in cancer patients[14], the patients were subgrouped by scores of Self-rating Depression Scale (SDS) and by with or without past experiences of chemotherapy. The results demonstrated that the regional brain influences of chemotherapy and depression were in part overlapping in the frontal cortex and that both would work in the same direction of decreasing brain metabolism in the cortex. Therefore, studies concerning neuro-immune interaction should employ patients before starting treatment.

In spite of the relatively small sample size and heterogeneity of the group in terms of diagnosis and history, this observation might provide supporting data for the presence of interactions between the brain and immune system. We hope that functional neuroimaging technique could provide more supporting data for cross-talk between mental, neural and immune aspects in patients.

References

1) Eysenck H.J., Adv. Behav. Res. Ther. **16** (1994) 167.
2) Derogatis R.L., Abeloff M.D., Melisaratos N., JAMA. **242** (1979) 1504.
3) Grossarth-Maticek R., Bastiaans J., Kanazir D.T., J. Psychosom. Res. **29** (1985) 167.
4) Greer S., Morris T., Pettingale K.W., et al., Lancet **1** (1990) 49.
5) Watson M., Haviland J.S., Greer S., et al., Lancet **354** (1999) 1331.
6) Tashiro M., Itoh M., Kubota K., et al., Psychooncology **10** (2001) 541.
7) Tashiro M., Kubota K., Itoh M., et al., Psycho-oncology. **8** (1999) 283.
8) Tashiro M., Kubota K., Itoh M., et al., Med. Sci. Monit. **7** (2001) 226.
9) Ader R., Felton D.L., Cohen N., Psychoneuroimmunology 2nd Ed., New York, Academic Press (1991).
10) Bovbjerg D.H, Valdimarsdottir H.B., Psycho-oncology (Ed. by Holland J.C.), New York, Oxford, Oxford University Press (1998) 125.
11) Renoux G., Biziere K., Renoux M., et al., Ann. N. Y. Acad. Sci. **496** (1987) 346.
12) Wik G., Lekander M., Fredrikson M., Brain Behav. Immun. **12** (1998) 242.
13) Lekander M., Fredrikson M., Wik G., Neurosci. Lett. **282** (2000) 193.
14) Tashiro M., Psychooncology **13** (2004) 486.

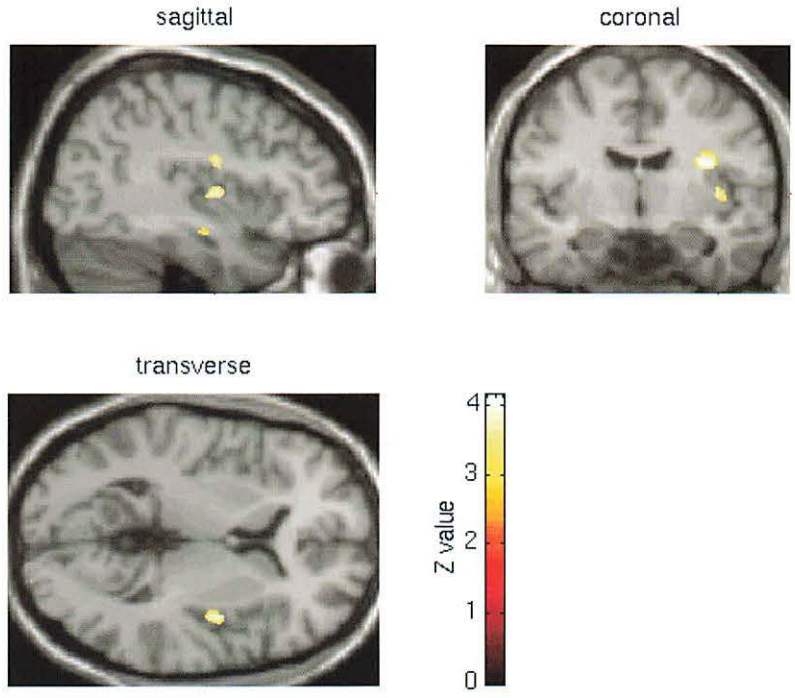

Figure 1. Regions associated with high natural killer cell activity (NKA). Decreased glucose uptake in the insular region was observed only in the high NKA subgroup (patients with cancer). In the low NKA subgroup (cancer patients), the regional glucose uptake in the insular region maintain at normal level. The statistical threshold: $p < 0.001$ (uncorrected).

VIII. 7. Reactivation of Medial Temporal Lobe and Occipital Lobe During the Retrieval of Color Information: a Positron Emission Tomography Study

Ueno A.[1], Abe N.[1], Suzuki M.[1,2], Hirayama K.[1], Mori E.[1], Tashiro M.[2], Itoh M.[2], and Fujii T.[1]

[1]Graduate School of Medicine, Tohoku University
[2]Cyclotron and Radioisotope Center, Tohoku University

Functional neuroimaging techniques such as positron emission tomography (PET) and functional magnetic resonance imaging (fMRI) allow us to monitor the brain activity associated with encoding and retrieval separately and to identify the brain regions commonly activated during encoding and retrieval. However, to date, only a relatively small number of neuroimaging studies have directly assessed whether the neural activity elicited during encoding is reactivated during retrieval of the encoded information[1-5].

The results of the previous studies indicate that some of the association cortices activated during encoding are also activated (reactivated) during retrieval. With regard to the reactivation of the MTL structures, the results of previous studies remain controversial. Since there are various constituents of the content of an event, it is worthwhile investigating what circumstances lead to overlapping activation in the MTL and other association cortices during both encoding and retrieval.

The present study further examined the reactivation hypothesis within the same sensory modality (i.e., visual modality) by investigating the encoding and retrieval of color information using PET. Specifically, the research question was whether overlapping activity would be found in both the MTL and color-related cortical regions during the encoding and retrieval of color information attached with meaningless shapes. In most previous imaging studies relevant to the reactivation hypothesis, meaningful stimuli were used. In the present study, completely arbitrary associative memory tasks between meaningless shapes and colors were applied to avoid potential confounding of preexisting binding between constituents of the memory content.

Subjects were presented with 20 stimuli (random shapes for the two encoding and

two retrieval conditions). Stimuli were presented on a black background on a display controlled by a Windows computer. List A (20 colored random shapes) was presented in one encoding condition (EC; encoding of colored shapes), and list B (20 white random shapes) in the other (EW; encoding of white shapes). During the two encoding conditions, subjects were asked to press a button with the index finger of their left hand as soon as the stimuli were presented and to memorize the shapes and colors of the stimuli. To boost subsequent retrieval, each encoding condition was repeated five times and only the first encoding condition was scanned with PET. List C (14 random shapes which were red or green at encoding, 3 random shapes which were white at encoding, and 3 unstudied random shapes) was presented in one retrieval condition (RC; retrieval of colored shapes), and list D (14 random shapes which were white at encoding, 3 random shapes which were red or green at encoding, and 3 unstudied random shapes) was presented in the other (RW; retrieval of white shapes). During 80-second PET data acquisition, 14 shapes which were colored at encoding, one shape which was white at encoding, and one new shape were presented in RC, and 14 shapes which were white at encoding, one shape which was green at encoding, and one new shape were presented in RW (see Fig. 1).

Regional cerebral blood flow (rCBF) was measured using PET (SET2400W Shimadzu, FWHM 4.0 mm) and ^{15}O-labeled water (approximately 180 MBq for each injection). The transaxial sampling field of view (FOV) was 256 mm, and the axial FOV was 190 mm. The thickness of the slices measured was 3.125 mm. Each task started 10 seconds before PET data acquisition, and lasted 100 seconds. PET data acquisition lasted 80 seconds. A transmission scan was followed by the experiment, and the data were used to obtain corrected emission images. A T1-weighted MRI scan (1.5T) was performed on a separate occasion for coregistration.

The data were analyzed with Statistical Parametric Mapping (SPM2) (Wellcome Department of Imaging Neuroscience, UK). All rCBF images acquired from each subject were realigned to correct for small movements occurring between scans. This process generated an aligned set of images and a mean image per subject. A T1-weighted structural MRI was coregistered to this mean PET image. Then the coregistered T1 image was normalized to the Montreal Neurological Institute (MNI) templates implemented in SPM2. The parameters from this normalization process were applied to each PET image. The PET images were reformatted to isometric voxels ($2\times2\times2$ mm^3) and smoothed with a Gaussian kernel of FWHM of 10 mm. The rCBF-equivalent measurements were adjusted to a global CBF mean of 50 ml/dl/min. Contrast of the condition effect of each voxel was

assessed using *t*-statistics, resulting in a statistical image (SPMt transformed into an SPMz). In both standard pairwise contrasts (i.e., EC vs. EW and RC vs. RW) and a cognitive conjunction analysis (i.e., EC vs. EW conjunct with RC vs. RW)[6], the threshold of significance was set at $p < 0.001$ (uncorrected for multiple comparisons). To reduce the possibility of false-positive results (Type 1 errors), we regarded clusters of 25 or more voxels as significant.

First, EC was compared with EW. This contrast showed brain activations in the bilateral occipital region, the left supramarginal gyrus, the left superior frontal gyrus, and the left putamen. Second, RC was compared with RW. RC, relative to RW, was associated with activations in the right lingual gyrus and the left middle occipital gyrus. Finally, to determine whether brain regions activated during encoding were reactivated at retrieval, we used a conjunction analysis (EC vs. EW conjunct with RC vs. RW). This analysis revealed that the right parahippocampal gyrus, the right lingual gyrus, the right inferior occipital gyrus, and the left putamen were active in both the encoding contrast and the retrieval contrast (Table 1 and Fig. 2).

The results showed that overlapping activity was found in the MTL and the occipital lobe (the lingual and inferior occipital gyri) in the right hemisphere during the encoding and retrieval of meaningless shapes with color information compared with those without color information. In EC all stimuli were colored shapes, and in EW all stimuli were white shapes. By contrast, in both of the retrieval conditions (RC and RW) all stimuli were white shapes. Therefore, encoding-related activations probably reflect the on-line processing of color information from the external world (i.e., the process of actual color perception) and binding it with shapes, whereas retrieval-related activity could not be attributed to the on-line processing of color information from the external world but rather to the process of retrieval of color information from the recognized shapes. Hence, this finding supports the reactivation hypothesis that postulates that the retrieval of specific event information is associated with the reactivation of both the MTL structures and regions that were involved during encoding of the same information.

References

1) Nyberg L., Habib R., Mcintosh AR., Tulving E., Proc. Natl. Acad. Sci. USA **97** (2000) 11120.
2) Persson J., Nyberg L., Microsc. Res. Tech. **51** (2000) 39.
3) Wheeler M.E., Petersen M.E., Buckner R.L., Proc. Natl. Acad. Sci. USA **97** (2000) 11125.
4) Nyberg L., Petersson K.M., Nilsson L.G., Sandblom J., Aberg C., Ingvar M., Neuroimage **14** (2001) 521.
5) Vaidya C.J., Zhao M., Desmond .JE., Gabrieli J.D.E., Neuropsychologia **40** (2002) 2136.

6) Friston K.J., Penny W.D., Glaser D.E., Neuroimage **25** (2005) 661.

Table 1. Brain regions showing overlapping activity during encoding and retrieval of color information.

Region (Brodmann's Area)	MNI coordinates			Z value	Cluster size
	x	*y*	*z*		
R parahippocampal gyrus (BA28)	18	-22	-16	3.68	25
R lingual gyrus (BA18)	18	-88	-6	4.12	83
R inferior occipital gyrus (BA18)	34	-88	-16	4.45	58
L putamen	-30	10	0	3.78	36

EC: encoding of colored shapes condition; EW: encoding of white shapes condition;
R; right; L: left.

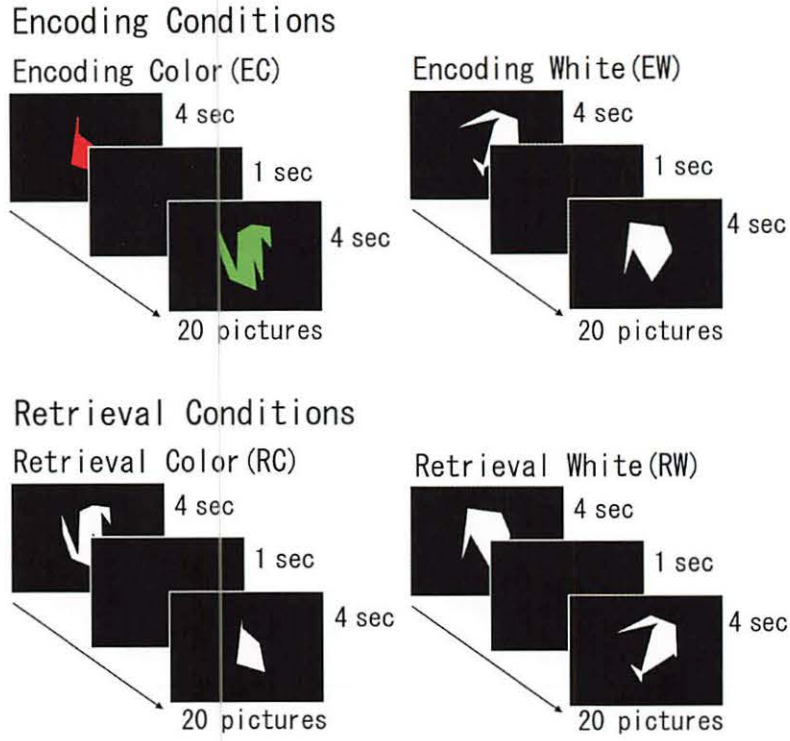

Figure 1. The experimental design, which involved two encoding conditions (EC and EW) and two retrieval conditions (RC and RW). In the encoding conditions, subjects were asked to learn the shapes and colors of 20 stimuli. In the retrieval conditions, subjects were asked to judge whether the stimuli had been presented with red, green, or white, or had not been presented at the encoding conditions. Note that all stimuli in the retrieval conditions were presented with white. EC, encoding of colored shapes condition; EW, encoding of white shapes condition, RC, retrieval of colored shapes condition; RW, retrieval of white shapes condition.

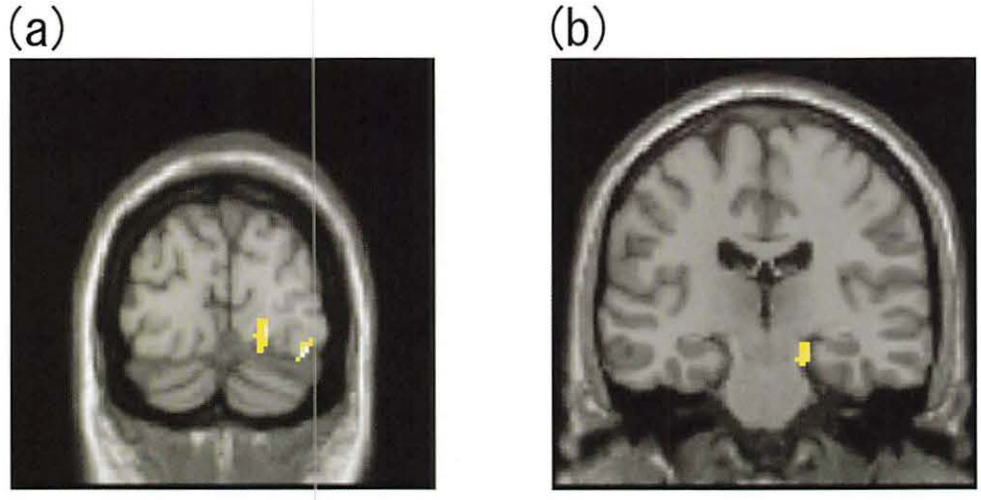

Figure 2. Brain activations common to the encoding and retrieval of color information (EC vs. EW conjunct with RC vs. RW). The activations are superimposed onto MRIs of Montreal Neurological Institute (MNI) templates. (a) Right lingual gyrus (18, -88, -6), right inferior occipital gyrus (34, -88, -16). (b) Right parahippocampal gyrus (18, -22, -16).

IX. RADIATION PROTECTION AND TRAINING OF SAFETY HANDLING

IX. 1. Beginners Training for Safe Handling of Radiation and Radioisotopes in Tohoku University

Baba M., Miyata T., and Iwata R.

Cyclotron and Radioisotope Center, Tohoku University

During 2005, the beginners training for safe handling of radiation and radioisotopes in Tohoku University was conducted in three courses as usual:
1) Radiation and Isotopes, 2) X-ray Machines and Electron Microscope, and 3) Synchrotron Radiation (SOR). The training was held twice a year, May and November, under the help for lectures and practice from various departments and research institutes of the university.

Lectures in English which were started in November of 2002 were continued for students and/or researchers who are not so familiar with Japanese language, by using PC projector and text of copies of view graphs (English class). The membership of the English class is increased markedly from the last year as shown later.

The training for "Radiation and Radioisotopes" is for persons who use unshielded radioisotopes and accelerators, and has been conducted from 1977. The contents of lectures and practices are shown in Table 1. The order and content of the lecture was slightly modified from November aiming at better understanding by trainees: the lecture on "the effect of radiation on human" was moved to the second to give stronger motivation for the training course and the following lectures. Along with the change, a new introductory lecture of "Introduction to radiation" was newly prepared as the first lecture to provide knowledge required to understand the lecture of "the effect of radiation on human". In the fiscal year of 2005, the training was performed for 525 persons (38 persons in the English class). The departments or institutes to which they belong are given in Table 2.

The training for "X-ray machines and electron microscopes" started at the end of 1983. The training is scheduled twice a year at the same time as that for "Radiation and Radioisotopes". In this course, only lectures are given with no practice. The contents of the lectures and the distributions of trainees are shown in Table 3 and Table 4, respectively. The number of trainees was 478 (44 in the English class).

The training for the "Synchrotron Radiation" began at the end of 1995. The contents of the lectures are the same as those of the radiation and radioisotopes but no practice. In 2004, the number of trainees of the SOR course was 94 (6 in the English class).

Table 1. Contents of the lectures and practices for safe handling of radiation and radioisotopes in 2005.

Lectures (one day)	Hours
Introduction to radiation	0.5
Effects of radiation on human	1.0
Radiation physics and measurements	1.0
Chemistry of radioisotopes	1.0
Radiological protection ordinance including video	1.5
Safe handling of radioisotopes	1.5

Practices (one day)	Hours
Treatment of unsealed radioactive solution	4.0
Measurement of surface contamination and decontamination	1.0
Measurement of gamma-rays and beta-rays	2.0

Table 2. Distribution of trainees for "Radiation and Radioisotopes" in 2005.

Department	Staff	Student	Total	English class
CYRIC	1	5	6	2
Medicine	18	53	71	5
Dentistry	0	11	11	0
Pharmacy	0	57	57	5
Science	2	59	61	2
Engineering	4	80	84	8
Agriculture	1	80	81	3
Research Institutes	11	104	115	13
The others	0	1	1	0
Total	37	450	487	38

Table 3 Contents of the lectures for "X-ray machines and Electron microscopes" in 2005 (same for both Japanese and English class)

Lectures (one day)	Hours
Safe handling of X-ray machines	1.5
Radiological protection ordinance	0.5
Video for safe handling of radiation and radioisotopes	0.5

Table 4 Distribution of trainees for "X-ray machines and Electron microscopes" in 2005.

Department	Staff	Student	Total	English class
Medicine	3	1	4	
Pharmacy	2	19	21	
Science	0	18	18	1
Engineering	16	174	190	10
Research Institutes	35	149	184	33
The others	4	13	17	
Total	60	374	434	44

Table 5 Distribution of trainees for "Synchrotron radiation" in 2005.

Department	Staff	Student	Total	English Class
Pharmacy	0	1	1	
Science	1	8	9	1
Engineering	1	30	31	
Research Institutes	8	39	47	5
Total	10	78	88	6

IX. 2. Radiation Protection and Management

Miyata T.[1], Baba M.[1], and Nakae H.[2]

[1]Cyclotron and Radioisotope Center, Tohoku University
[2]Japan Radiation Protection Co., Ltd.

(1) Overview

During the fiscal year of 2005, research and education in the center were conducted as active as usual.

New ^{7}Li(p,n) neutron source installed at the 3-2 course of CYRIC last year has been used for actual experiments and proved very effective in study of neutron induced cross -sections and irradiation of semiconductors devices. This source was designed to achieve a highest level neutron flux over the world by enabling a short distance between target and sample or detector down to one meter. Now the source is served to experiments using mono-energy neutrons and semiconductor test experiments.

Last year, "β-ray analysis room" in Radio Isope Room was converted into PET Research Room to promote life science reaserch using PET and a γ-camera. The 931 PET placed in Research Building was moved to the room after conversion of the room and approval of radiation licensing.

The new online radiation protection and management system of CYRIC which was installed in 2002 worked fairly reliably except for some problems slowing down of the system response when the data transfer rate is so high. The radiation detectors connected with the monitoring system performed reliably too while one gamma detector should be repaired.

Along with the change of organization of the university, measurement of radioactivity concentration is continued periodically but the observed level was low enough generally. Devices and gas counters with automatic sample changer for radioactivity concentration measurement (samplers, α-β automatic counters) were routinely used without serious problems by several radiation facilities in Tohoku University.

(2) Unsealed radio nuclides used in CYRIC

The species and amounts of unsealed radio nuclides handled in CYRIC during the fiscal year of 2003 are summarized in Table 1. The table includes the isotopes produced by the cyclotron as well as those purchased from the Japan Radio Isotope Association or taken over from other radioisotope institutes.

(3) Radiation exposure dose of individual worker

The exposure doses of the workers in CYRIC during 2005 are given in Table 2. The doses were sufficiently lower than the legal dose limits.

(4) Radiation monitoring of the workplace

Radiation dose rates inside and outside of the controlled areas in CYRIC were monitored periodically and occasionally when needed. They were generally below the legal dose limits although there are several "hot spots" in mSv/hr range like slits or beam stopper and so on. Surface contamination levels of the floors inside the controlled areas were also measured with a smear method and a survey meter method. They were under the legal regulation levels.

(5) Wastes management

The radioactive wastes were delivered to the Japan Radio Isotope Association twice in the fiscal year of 2005.

The concentration of radioisotopes in the air released from the stack after filtration was monitored with stack gas monitors. The values on concentration were lower than the legal regulation levels. The radioactive water was stocked in the tanks at least for 3 days and then released to the sewerage after confirming that the concentration was lower than the legal regulation levels.

Radioactive organic scintillator waste of 800 litter was treated by incinerator provided by Fuji-kogyo Co.Ltd. The incinerator was overhauled last year.

Table 1. Unsealed radioisotopes used in each building of CYRIC during 2005.

(a) Cyclotron Building (kBq)

Group 1, 2		Group 3		Group 4	
^{42}Ar	4.000	^{11}C	763,028,800.000	^{18}F	674,459,200.000
Total	4.000	Total	763,028,800.000	Total	674,459,200.000

(b) Radioisotope Building (kBq)

Group 1, 2		Group 3		Group 4	
^{90}Sr	34.616	^{11}C	1,483,700.000	^{14}C	11,471.000
^{56}Co	3,640.870	^{99}Mo	4,050,510.000	^{51}Cr	8,351.420
^{137}Cs	720.000	^{32}P	1,555,243.962	^{18}F	1,833,350.000
^{55}Fe	3,483.900	^{99m}Tc	4,220,210.000	^{3}H	88,618.070
^{125}I	221,669.992	^{48}V	1,998.158		
Total	229,549.378	Total	11,311,662.212	Total	1,941,790.490

* Including the use in the "β-ray analysis" room

(c) Research Building (kBq)

Group1,2		Group 3		Group 4	
		^{11}C	3,700,000.000	^{18}F	518,000.000
		^{15}O	10,915,000.000		
Total	0	Total	14,615,000.000	Total	518,000.000

Table 2. Occupational radiation exposures at CYRIC during the fiscal year of 2004.

Dose range (mSv)	Number of individuals
No measurable exposure	33
< 1.0	10
1.0 ~ 2.0	6
2.0 ~ 2.5	1
Total number of persons monitored	50

X. PUBLICATIONS

X. PUBLICATIONS

[636] A New Passive Dosemeter Using an Imaging Plate and Annealing.
Hiroko Ohuchi, Akira Yamadera, Mamoru Baba.
Radioisotopes, **53** (2004) 115-122.

[637] Application of Imaging Plates to Cumulative Dosemeter for High X-ray Radiation Fields.
H. Ohuchi, A. Yamadera.
J. Nucl. Sci. Tech., **Suppl. 4** (2004) 140-143.

[638] Measurement of Low-Level Radioactive Liquid Waste with Imaging Plates.
H. Ohuchi, A. Yamadera, M. Baba.
J. Nucl. Sci. Tech., **Suppl. 4** (2004) 196-199.

[639] Measurement of the g-Factor of the 27^- High-Spin Isomer State of ^{152}Dy.
M. Fujita, T. Endo, A. Yamazaki, T. Sonada, T. Miyake, E. Tanaka, T. Shinozuka, T. Suzuki, A. Goto, Y. Miyashita, N. Sato, Y. Wakabayashi, N. Hokoiwa, M. Kibe, Y. Gono, T. Fukuchi and A. Odahara.
Hyperfine Interact.., **159** (2004) 245-249.

[640] Upgraded sinusoidal beam chopping system at CYRIC.
A. Terakawa, M. Tanigaki, K. Itoh, M. Fujita, T. Shinozuka, H. Orihara.
Nucl. Instrum. Methods .Phys. Res., A **538** (2005) 218-224.

[641] Preclinical and clinical evaluation of *O*-[^{11}C]methyl-L-tyrosine for tumor imaging by positron emission tomography.
Kiichi Ishiwata, Hideo Tsukada, Kazuo Kubota, Tadashi Nariai, Norihiro Harada, Kazunori Kawamura, Yuichi Kimura, Keiichi Oda, Ren Iwata, Kenji Ishii.
Nucl. Med. Biol., **32** (2005) 253-262.

[642] Increased [^{18}F]Fluorodeoxyglucose Accumulation in Right ventricular Free Wall in Patients with Pulmonary Hypertension and Effect of Epoprostenol.
Minako Oikawa, Yutaka Kagaya, Hiroki Otani, Masahito Sakuma, Jun Demachi, Jun Suzuki, Tohru Takahashi, Jun Nawata, Tatsuo Ido, Jun Watanabe, Kunio Shirato.
J. Amer. Coll. Cardiology, **45** (2005) 1849-1855.

[643] Determination of the Gamow-Teller quenching factor from charge exchange reaction on ^{90}Zr.
K. Yako, H. Sakai, M.B. Greenfield, K. Hatanaka, M. Hatano, J. Kamiya, H. Kato, Y. Kitamura, Y. Maeda, C.L. Morris, H. Okamura, J. Rapaport, T. Saito, Y. Sakemi, K. Sekiguchi, Y. Shimizu, K. Suda, A. Tamii, N. Uchigashima, T. Wakase..
Phys. Lett., **B615** (2005) 193-199.

[644] Response of a germanium detector to energetic heavy ions.
R. Taki, H. Okamura, N. Fukunishi, H. Ryuto, N. Sakamoto, K. Sekiguchi, A. Goto.
Nucl. Instrum. Methods .Phys. Res., A **545** (2005) 269-272.

[645] Classical conditioned response of rectosigmoid motility and regional cerebral in humans.
M. Kanazawa, M. Endo, K. Yamaguchi, T. Hamaguchi, W.E. Whitehead, M. Itoh, and S. Fukudo.
Neurogastr. Moti,l **17** (2005) 705-713.

[646] Resolving the Discrepancy of 135 MeV *pd* Elastic Scattering Cross Sections and Relativistic Effects.
K. Sekiguchi, H. Sakai, H. Witala, W. Glöckle, J. Golak, K. Hatanaka, M. Hatano, K. Itoh, H. Kamada, K. Kuboki, Y. Maeda, A. Nogga, H. Okamura, T. Saito, N. Sakamoto, Y. Sakemi, M. Sasano, Y. Shimizu, K. Suda, A. Tamii, T. Uesaka, T. Wakasa, and K. Yako.
Phys. Rev. Lett., **95** (2005) 162301.

[647] Measurement of Neutron Emission Spectra in Li(d,xn) Reaction with Thick and Thin targets for 40-MeV Deuterons.
M. Hagiwara, T. Itoga, N. Kawata, N. Hirabayashi, T. Oishi, T. Yamauchi, M. Baba, M. Sugimoto, T. Muroga..
Fusion Sci. Tech., **48** (2005) 1320-1328.

[648] Microbeam Analysis at Tohoku University for Biological Studies.
S. Matsuyama, K. Ishii, S. Abe, H. Ohtsu, H. Yamazaki, Y. Kikuchi, Ts. Amartaivan, K. Inomata, Y. Watanabe, A. Ishizaki, Y. Barbotteau, A. Suzuki, T. Yamaguchi, G. Momose and H. Imaseki.
Int. J. PIXE, **15** (2005) 41-45.

[649] Microbeam Analysis of Single Aerosol Particles at Tohoku University.
S. Matsuyama, K. Ishii, H. Yamazaki, Y. Kikuchi, Ts. Amartaivan, S. Abe, K. Inomata, Y. Watanabe, A. Ishizaki, R. Oyama, Y. Kawamura, A. Suzuki, T. G. Momose T. Yamaguchi and H. Imaseki.
Int. J. PIXE, **15** (2005) 257-262.

[650] Detection of nuclear de-exceitation gamma-rays in water Cherenkov detector.
K. Kobayashi, Y. Itow, M. Shinozawa, M. Yosoi, H. Akimune, H. Ejiri, H. Fujimura, M. Fujiwara, K. Hara, K.Y. Hara, T. Ishikawa, M. Itoh, T. Kawabata, M. Nakamura, H. Sakaguchi, Y. Sakemi, H. Takeda, M. Uchida, T. Yamada, Y. Yasuda, H.P.Yoshida and R.G.T. Zegers.
Nucl. Phys., B (Proc. Suppl.) **139** (2005) 72-76.

[651] Analyzing powers for exclusive $1s_{1/2}$ proton knockout from light nuclei.
T. Noro, T. Yonemura, S. Asaji, N.S. Chant, K. Fujita, Y. Hagihara, K. Hatanaka, G.C. Hillhouse, T. Ishida, M. Itoh, S. Kishi, M. Nakamura, Y. Nagasue, H. Sakaguchi, Y. Sakemi, Y. Shimizu, H. Takeda, Y. Tamesige, S. Terashima, M. Uchida, T. Wakasa, Y. Yasuda, H.P. Yoshida, and M. Yosoi.
Phys. Rev., C **72** (2005) 041602.

[652] Automated preparation of hypoxic cell marker [^{18}F]FRP-170 by on-column hydrolysis.
Y. Ishikawa, R. Iawata, S. Furumoto, Y. Takai.
Appl. Radiat. Isot., **62** (2005) 705-710.

[653] Preclinical and clinical evaluation of *O*-[^{11}C]methyl-L-tyrosine for tumor imaging by positron emission tomography.
K. Ishiwata, H. Tsukada, K. Kubota, T. Nariai, N. Harada, K. Kawamura, Y. Kimura, K. Oda, R. Iwata, and K. Ishii.
Nucl. Med. Biol., **32** (2005) 253-262.

[654] Simple automated preparation of [^{11}C]*O*-methyl-L-tyrosine for routine clinical use.
Y. Ishikawa, R. Iwata, S. Furumoto, C. Pascali, A. Bogni, K. Kubota and K. Ishiwata.
Appl. Radiat. Isot., **63** (2005) 55-61.

[655] Use of reference tissue models for quantification of histamine H1 receptors in human brain by using positron emission tomography and [^{11}C]doxepin.
A. Suzuki, M. Tashiro, Y. Kimura, H. Mochizuki, K. Ishii, H. Watabe, K. Yanai, K. Ishiwata, K. Ishii.
Ann. Nucl. Med., **19** (2005) 425-433.

[656] An experimental study on *O*-[^{18}F]fluoromethyl-L-tyrosine for differentiation between tumor and inflammatory tissues.
M. Suzuki, K. Yamaguchi, G. Honda, R. Iwata, S. Furumoto, M. Jeong, H. Fukuda and M. Itoh.
Ann. Nucl. Med., **19** (2005) 589-595.

[657] Histamine H1 receptors in schizophrenic patients measured by positron emission tomography.
K. Iwabuchi, C. Ito, M. Tashiro, H. Mochizuki, M. Kato, M. Kano, K. Ishii, K. Ishiwata, M. Itoh, R. Iwata, H. Matsuoka, M. Sato and K. Yanai.
Eur. Neuropsychopharmacol., **15** (2005) 185-191.

[658] Mild cognitive impairment after adjuvant chemotherapy in breast cancer patients-evaluation of appropriate research design and methodology to measure symptoms.
T. Matsuda, T. Takayama, M. Tashiro, Y. Nakamura, Y. Ohashi, K. Shinozuma.
Breast Cancer, **12** (2005) 279-287.

[659] Effects of fexofenadine and hydroxyzine on brake reaction time during car-driving with cellular phone use.
M. Tashiro, E. Horikawa, H. Mochizuki, Y. Sakurada, M. Kato, T. Inokuchi, F. Ridout, I. Hindmarch, K. Yanai.
Hum. Psychopharmacol., **20** (2005) 501-509.

[660] The neural correlates of driving performance identified using positron emission tomography.
E. Horikawa, N. Okamura, M. Tashiro, Y. Sakurada, M. Maruyama, H. Arai, K. Yamaguchi, H. Sasaki, K. Yanai, M. Itoh.
Brain Cogn., **585** (2005) 166-171.

XI. MEMBERS OF COMMITTEE

XI. MEMBERS OF COMMITTEE (as of Jan. 1, 2006)

General

(Chairman)	Keizo	Ishii	(Graduate School of Engineering)
	Tetsuo	Shoji	(Executive Vice President)
	Osamu	Hashimoto	(Graduate School of Science)
	Kazuaki	Iwasa	(Graduate School of Science)
	Akira	Takahashi	(Graduate School of Medicine)
	Keiichi	Sasaki	(Graduate School of Dentistry)
	Koji	Fukunaga	(Graduate School of Pharmaceutical Sciences)
	Katsunori	Abe	(Graduate School of Engineering)
	Ryoichi	Katsumata	(Graduate School of Agricultural Science)
	Kazuhiko	Nishitani	(Graduate School of Life Science)
	Isamu	Sato	(Institute for Materials Research)
	Hiroshi	Fukuda	(Institute for Development, Aging and Cancer)
	Osamu	Tochiyama	(Institute of Multidisciplinary Research for advanced Materials)
	Syoki	Takahashi	(University Hospital)
	Jirohta	Kasagi	(Laboratory of Nuclear Science)
	Tatsuo	Ido	(CYRIC)
	Masatoshi	Itoh	(CYRIC)
	Mamoru	Baba	(CYRIC)
	Ren	Iwata	(CYRIC)
	Hiroyuki	Okamura	(CYRIC)
	Tsutomu	Shinozuka	(CYRIC)
	Toshio	Kobayashi	(Graduate School of Science)
	Kazuhiko	Yanai	(Graduate School of Medicine)
	Tetsuya	Ono	(Radiation Safety Committee, Research Promotion Council)
(Observer)	Ryuko	Yoshida	(Head of Administration Office, Graduate School of Information Science)

Cyclotron

(Chairman)	Hiroyuki	Okamura	(CYRIC)
	Osamu	Hashimoto	(Graduate School of Science)
	Toshio	Kobayashi	(Graduate School of Science)
	Hideya	Onodera	(Graduate School of Science)
	Tsutomu	Sekine	(Centre for the Advancement of Higher Education)
	Kazushige	Maeda	(Graduate School of Science)
	Hirokazu	Tamura	(Graduate School of Science)
	Keizo	Ishii	(Graduate School of Engineering)
	Akira	Hasegawa	(Graduate School of Engineering)
	Isamu	Sato	(Institute for Materials Research)
	Masao	Saitoh	(Institute of Multidisciplinary Research for advanced Materials)
	Tsutomu	Otsuki	(Laboratory of Nuclear Science)
	Masatoshi	Itoh	(CYRIC)
	Mamoru	Baba	(CYRIC)
	Ren	Iwata	(CYRIC)
	Tsutomu	Shinozuka	(CYRIC)

Radiation Protection and Training of Safe Handling

(Chairman)	Mamoru	Baba	(CYRIC)
	Kazuaki	Iwasa	(Graduate School of Science)
	Yoshihiko	Uehara	(Graduate School of Medicine)
	Yasushi	Yamazoe	(Graduate School of Pharmaceutical Sciences)
	Keizo	Ishii	(Graduate School of Engineering)
	Toshiyasu	Yamaguchi	(Graduate School of Agricultural Science)
	Kazuhiro	Sogawa	(Graduate School of Life Science)
	Masayuki	Hasegawa	(Institute for Materials Research)
	Hiroshi	Fukuda	(Institute for Development, Aging and Cancer)
	Tomohiro	Kaneta	(University Hospital)
	Tsutomu	Shinozuka	(CYRIC)

Life Science

(Chairman)	Masatoshi	Itoh	(CYRIC)
	Noriaki	Ohuchi	(Graduate School of Medicine)
	Shogo	Yamada	(Graduate School of Medicine)
	Syoki	Takahashi	(Graduate School of Medicine)
	Teiji	Tominaga	(Graduate School of Medicine)
	Masahiko	Yamamoto	(Graduate School of Medicine)
	Yukitsuka	Kudo	(Biomedical Engineering Research Organization)
	Makoto	Watanabe	(Graduate School of Dentistry)
	Sumio	Ohtuki	(Graduate School, Division of Pharmaceutical Sciences)
	Keizo	Ishii	(Graduate School of Engineering)
	Kazuo	Yamamoto	(Graduate School of Life Science)
	Hiroshi	Fukuda	(Institute for Development, Aging and Cancer)
	Junichi	Gotoh	(University Hospital)
	Yoshihiro	Takai	(College of Medical Sciences)
	Ren	Iwata	(CYRIC)
	Manabu	Tashiro	(CYRIC)
	Yoshihito	Funaki	(CYRIC)

Prevention of Radiation Hazards

(Chairman)	Mamoru	Baba	(CYRIC)
	Osamu	Hashimoto	(Graduate School of Science)
	Tsutomu	Sekine	(Graduate School of Science)
	Keizo	Ishii	(Graduate School of Engineering)
	Ren	Iwata	(CYRIC)
	Tsutomu	Shinozuka	(CYRIC)
	Masashi	Koseki	(CYRIC)
	Takamoto	Miyata	(CYRIC)

Research Program

(Chairman)	Mamoru	Baba	(CYRIC)
	Masatoshi	Itoh	(CYRIC)
	Ren	Iwata	(CYRIC)
	Hiroyuki	Okamura	(CYRIC)
	Tsutomu	Shinozuka	(CYRIC)
	Osamu	Hashimoto	(Graduate School of Science)
	Tsutomu	Sekine	(Centre for the Advancement of Higher Education)
	Kazuhiko	Yanai	(Graduate School of Medicine)
	Akira	Takahashi	(Graduate School of Medicine)
	Katsunori	Abe	(Graduate School of Engineering)
	Hiromichi	Yamazaki	(Graduate School of Engineering)
	Isamu	Sato	(Institute for Materials Research)
	Hiroshi	Fukuda	(Institute for Development, Aging and Cancer)
	Syoki	Takahashi	(University Hospital)
	Jirohta	Kasagi	(Laboratory of Nuclear Science)
	Toshio	Kobayashi	(Graduate School of Science)
	Kazushige	Maeda	(Graduate School of Science)
	Hirokazu	Tamura	(Graduate School of Science)

XII. STAFF

XII. STAFF (as of Jan. 1, 2006)

Director Keizo Ishii

Division of Accelerator

Osamu	Hashimoto[1)]
Tsutomu	Shinozuka
Takashi	Wakui
Mifuyu	Ukai
Akiyoshi	Yamazaki
Shizuo	Chiba[5)]
Yasuaki	Ohmiya[5)]
Naoto	Takahashi[5)]
Shigenaga	Yokokawa[5)]
Akihiko	Matsumura[5)]
Takaaki	Nakahara[5)]

Division of Instrumentations

Hiroyuki	Okamura
Toshio	Kobayashi[1)]
Hikonojo	Orihara[4)]
Masatoshi	Itoh
Sho-ichi	Watanuki
Kazutaka	Ohzeki

Division of Radiopharmaceutical Chemistry

Ren	Iwata
Yukitsuka	Kudo[3)]
Yoshihito	Funaki
Yohichi	Ishikawa
Shozo	Furumoto[3)]

Division of Cyclotron Nuclear Medicine

Masatoshi	Itoh
Kazuhiko	Yanai[2)]
Keiichiro	Yamaguchi[4)]
Kohichiro	Kawashima[4)]
Manabu	Tashiro
Masayasu	Miyake
Maki	Suzuki
Kazuaki	Kumagai
Kyokutoh	Dan
Mehedi	Masud
Sabina	Khond Kar
Manami	Suzuki
Goh	Honda
Takehisa	Sasaki
Targino Rodrigues Dos Santos	

Division of Radiation Protection and Safety Control

Mamoru	Baba
Takashi	Nakamura[4)]
Takamoto	Miyata
Morio	Katoh
Hirokazu	Nakae[6)]

Graduate Student and Researcher

Tomokazu	Suzuki	(Graduate School of Science)
Yu-ji	Miyashita	(Graduate School of Science)
Nozomi	Sato	(Graduate School of Science)
Miharu	Ohkuma	(Graduate School of Science)
Naoya	Sugimoto	(Graduate School of Science)
Shingo	Fukushima	(Graduate School of Science)
Tomohiro	Terazono	(Graduate School of Science)
Ryo	Matsuo	(Graduate School of Science)

Kimihiko	Sato	(Graduate School, Division of Pharmaceutical Sciences)
Yoshio	Honda	(Graduate School, Division of Pharmaceutical Sciences)
Akihiro	Sugawara	(Graduate School, Division of Medicine)
Margaretha	Sulistyoningsih	(Graduate School of Engineering)
Masayuki	Hagiwara	(Graduate School of Engineering)
Toshiro	Itoga	(Graduate School of Engineering)
Takuji	Ohishi	(Graduate School of Engineering)
Mohammad	Nakhostin	(Graduate School of Engineering)
Akram	Mohammadi	(Graduate School of Engineering)
Takashi	Sasaki	(Graduate School of Engineering)
Takahiro	Makino	(Graduate School of Engineering)
Yasuhiro	Unno	(Graduate School of Engineering)
Soh	Kamata	(Graduate School of Engineering)
Wataru	Takahashi	(Graduate School of Engineering)

Office Staff

Ryuko	Yoshida
Masashi	Koseki
Tomoya	Yonezawa
Yu-ko	Yamashita
Mitsuko	Endo
Kyoko	Fujisawa
Fumiko	Mayama
Masakatsu	Itoh
Kietu	Takahashi
Kimiko	Abe
Asami	Sawada
Yoshiro	Sukegawa
Ai	Endo
Shurikeiko	Fujimoto

1) Graduate School of Science
2) Graduate School of Medicine
3) TUBERO
4) Visiting Professor
5) SUMI-JU Accelerator Service Ltd.
6) Japan Radiation Protection Co., Ltd.